# FACULTY OF GRADUATE STUDIES

## Synthesis and Characterization of Nano-Iron Based Materials and Their Application for the Removal of Anionic and Cationic Dyes

تحضير وتشخيص مواد مستندة للحديد بمقياس النانو واستخدامها لإزالة الأصباغ السالبة والموجبة

This Thesis was submitted in partial fulfillment of the requirements for the

## Master's Degree in Applied Chemistry

From the Faculty of Graduate Studies at Birzeit University, Palestine

By: Muath Nairat

Supervised by: Prof. Talal Shahwan

# Synthesis and Characterization of Nano-Iron Based Materials and Their Application for the Removal of Anionic and Cationic Dyes

We approve the thesis of Muath Nairat

_____

Prof. Talal Shahwan
Supervisor
Chemistry Department – Chair Person
Birzeit University

_____

Assist. Prof. Zaki Hassan
Committee Member
Chemistry Department – Faculty Member
Birzeit University

_____

Assist. Prof. Hani Awad
Committee Member
Chemistry Department – Faculty Member
Birzeit University

18 May 2013
    **Date**

# ACKNOWLEDGEMENTS

*To the sanctification of divine entity whom am pride with servitude &*
*whose glorified existence was overtly manifested to me o'er this work*

# ABSTRACT

The scientific and research studies concerned with the removal of pollutants from both groundwater and surface water are distinguished by its vital importance and unrivaled scientific concern throughout the whole world. This is so not only because they are considered among the most essential environmental fields, but also because they focus on one of the most vital natural resources upon which all aspects of life do depend. It is water through which Almighty God hath made everything live, and without it life will no more exist.

Iron nanomaterials are emerging as very effective tools for the removal of a wide spectrum of pollutants from water. These materials are based on iron nanoparticles, the effectiveness of which is attributed to large surface area and enhanced surface activity. In addition to extensive laboratory-scale research that is being carried out internationally, field studies are also being performed in many countries to assess the feasibility of iron nanotechnology in environmental remediation. In this context, *in-situ* and *ex-situ* treatment methodologies are being investigated. *In-situ* treatment

involves direct injection of iron nanoparticles into underground water bodies, while *ex-situ* treatment involves deploying slurries of iron nanoparticles into large tanks containing polluted water or soil. Moreover, iron nanomaterials are being proposed to replace iron powder in modern water treatment facilities known as permeable reactive barriers (PRBs)

In this study, iron nanoparticles along with nano iron supported on natural zeolite (clinoptilolite) and alumina have been produced via reduction of iron ions using sodium borohydride. The composite materials demonstrated high dye removal capabilities. The usage of the given substrates contributed to decreasing the aggregation of iron nanoparticles, thus enhancing their surface activity and, as such, increasing their uptake capacity allowing for better reusability.

Iron nanoparticles and their based materials were characterized using XRD, XPS, FTIR, SEM, TEM, EDX and BET-$N_2$. The produced iron nanomaterials were then used in the removal of aqueous methylene blue and methyl orange as two models of cationic and anionic dyes, the dye removal was monitored using UV-visible and GC-MS. The experiments investigated the effects of contact time and

dyes concentrations, in order to assess the kinetic behavior of the dye removal process and the extent of dye removal using iron nanoparticles and compare it with the nano iron based materials.

The results indicate that the composite of iron nanoparticles supported on zeolite has the fastest dye removal kinetics which can be adequately described using $2^{nd}$ order kinetics for the removal of methylene blue with $k_2$ values of $8.8\pm1.5\times10^{-2} - 9.9\pm4.9\times10^{-1}$ L mg$^{-1}$ min$^{-1}$ followed by $1^{st}$ order kinetics for the removal of methyl orange at low initial concentrations with $k_1$ value of $1.9\pm2.7\times10^{-1}$ min$^{-1}$ and $2^{nd}$ order kinetics at high initial concentrations with $k_2$ value of $9.8\pm4.8\times10^{-3}$ L mg$^{-1}$ min$^{-1}$. Moreover, the same composite demonstrated applicability in dyes removal over a wide range of concentrations and high reusability of five successive cycles with stable dye removal percentages.

# ملخص

تَمتازُ الدراساتُ العِلمية والبحثيّةُ المتعلّقةُ بوسائلِ إزالة الملوّثات من المياهِ الجوفيّة والسطحيّة بأهميّةٍ بالغةٍ واهتمامٍ علميٍّ منقطع النظيرِ على المستوى العالمي ككل، لا لكونها من أهمّ حقول العلوم البيئيّةِ فحسب، بل لكونها تتعلّق بأهمِّ عنصرٍ طبيعيٍّ تعتمدُ عليه الكائناتُ جميعاً من أجل الحياة، وهو الماءُ الذي جعل الله منه كلَّ شيءٍ حيّ، إذْ بدونِهِ تنعدمُ كافّة أنماطِ الحياةِ على الأرض.

تعد مواد النانو للحديد من أكثر الوسائل كفاءةً في إزالة العديد من ملوثات المياه، والتي تعزى كفاءتها إلى طبيعتها المكونة من جزيئات النانو للحديد المتسمّة بمساحة السطح الواسعة وكفاءتها السطحية المحسنة. علاوةً على كثافة الدراسات البحثية المخبرية المجراة عالميا، غدا في دولٍ عدة إجراء دراسات تطبيقية على أرض الواقع في محاولةٍ لتحقيق مفهوم وإمكانية استعمال هذه الجزيئات في التنقية البيئية، وبهذا المنحى غدا تحقيق وسائل داخلية وخارجية لتنقية المياه، فقد أُجريت تجارب حقن وإدخال جزيئات النانو للحديد في المياه الجوفية مباشرة، وبحيز آخر قد تمَّ استخدامُ هذهِ الجزيئات كخليط يوضع في خزانات خارجية لمعالجة المياه أو التربة الملوثة. ويتمَّ اقتراح استخدام مواد النانو للحديد كبديلٍ لبرادة الحديد في إحدى وسائل تنقية المياه الحديثة المسماة بـ "السدود الفعالة شبه النفاذة".

في هذه الدراسة، تم تحضير جزيئات النانو للحديد منفردة، بالإضافة إلى جزيئات النانو للحديد المستندة على الزيولايت الطبيعي (الكلينوبتيلولايت) وجزيئات النانو للحديد المستندة على أكسيد الألمنيوم، وذلك من خلال اختزال أيونات الحديد ببوروهايدرايد الصوديوم. وقد أظهر إسناد جزيئات النانو للحديد ارتفاعا ملحوظا في كفاءة هذه الجزيئات

على أصعدة الفعالية، تكرير الاستخدام وإمكانية الإزالة للأصباغ، والتي تعزى لتقليل تلاصق جزيئات النانو للحديد من أجل زيادة الكفاءة السطحية ومعها ارتفاع إمكانيتها في الإزالة.

كما تم تشخيص جزيئات النانو للحديد والمواد المستندة له باستخدام: محايد الأشعة السينية، مطياف الأشعة السينية للإلكترون الضوئي، مطياف الأشعة تحت الحمراء، المجهر الإلكتروني الماسح، المجهر الإلكتروني النافذ، مطياف طاقة الأشعة السينية المشتتة، ومساحة السطح المحددة. وقد تم استعمال هذه المواد المستندة للحديد في إزالة المحاليل المائية للميثلين الأزرق والميثيل البرتقالي كنماذج للأصباغ الموجبة والسالبة، والتي تم متابعة سير إزالتها بمطياف الأشعة فوق البنفسجية والمرئية، وجهاز الكروماتجرافيا الغازي بالمطياف الكتلي. كما تمَّ في ذاتِ الوقتِ بحث تأثير عاملي الزمن وتركيز الأصباغ من أجل تحديد المدى والسلوك الحركي لعملية إزالة الأصباغ باستخدام جزيئات النانو للحديد ومقارنة ذلك كله بالمواد المستندة للحديد بمقياس النانو.

أظهرت النتائج أن لجزيئات النانو للحديد المستندة على الزيولايت الطبيعي السرعة الأكبر بإزالة الأصباغ حيث تم إزالة الميثلين الأزرق بتفاعل من الرتبة الثانية وبثوابت اتزان قيمتها $4.9\pm9.9\times10^{-1}$–$1.5\pm8.8\times10^{-2}$ لتر ملغم$^{-1}$ د$^{-1}$، في حين أن تفاعل الميثيل البرتقالي سلك تفاعلا من الرتبة الأولى عند التراكيز المنخفضة بثابت إتزان قيمته $2.7\pm1.9\times10^{-1}$ د$^{-1}$ وتفاعلا من الرتبة الثانية عند التراكيز المرتفعة بثابت اتزان قيمته $4.8\pm9.8\times10^{-3}$ لتر ملغم$^{-1}$ د$^{-1}$. وقد أظهرت المادة ذاتها كفاءة عالية في إزالة الأصباغ على منحىً واسع من التراكيز المختلفة وإمكانية تكرير الاستعمال لخمس محاولات بقدرة إزالة ثابتة.

# ORIGINALITY OF THE WORK

The author declares that all the findings and interpretations in this work are of originality that haven't been published elsewhere expect where it was mentioned and cited.

The results in section 3.2.7 under the title "nZVI as a Fenton Catalyst" have been published previously by our group in *Chem. Eng. J.* **2001**, *172*, 258.

All the results regarding Ze-nZVI preparation, characterization and dye removal assessment have been submitted for publication in *Clean – Soil, Air, Water*.

# TABLE OF CONTENTS

# LIST OF FIGURES

# LIST OF TABLES

# Chapter 1

# INTRODUCTION

## 1.1 Waste Water and Dye Pollution

Water pollution is a major field in environmental sciences due to the importance of water, which covers more than 70% of the earth's surface, and its necessity for life, as most animals and plants are composed of 60% water by volume.[1] Water can be affected by various types of chemical pollutants such as heavy metals (e.g. arsenic, lead, mercury etc.), organic compounds (e.g. dyes, trichloroethane, carbon tetrachloride etc.), inorganic anions (e.g. nitrates, phosphates, perchlorates etc.), in addition to biological pollutants such as bacteria.

Dyes have been known to human beings thousands of years ago[2] and the earliest use of colorant is believed to be by Neanderthal man about 180,000 years ago. However, the first use of organic colorant was much later, being around 4,000 years ago when the blue dye indigo was found in the wrappings of the mummies in the Egyptian tombs.[3] The use of dyes was limited only to natural sources such as

plants, insects and mollusks, and were produced and used in small scale quantities till the end of the nineteenth century then the breakthrough came with Perkin's historic discovery of the first synthetic dye, mauveine, in 1856, after so, dyes were produced and used in large scale quantities. [4]

All dyes share two important components: chromophores which are responsible for producing the color and auxochromes which enhance the affinity of the dye toward the fibers. [5] However, dyes exhibit considerable structural diversity and can be classified in several ways according to their chemical structure and their application. [4] Dyes can be classified according to their solubility in water: soluble dyes which include acid, basic, mordant, metal complex, direct and reactive dyes; insoluble dyes including azoic, sulfur, vat and disperse dyes. [5] Each class of dye exhibit its unique properties arising from its chemical structure, hence promoting each class to be implemented in versatile areas as described in Table 1.1. [5,6] Another important dye classification is made in accordance with its charge: i.e. cationic, anionic and nonionic [7]

**Table 1.1 Classes of dyes and their applications** [5,6]

| Dye Class | Description and Applications |
|-----------|------------------------------|
| Acid | Water soluble anionic compounds, used for nylon, wool, silk, modified acrylics, and also to some extent for paper, leather, ink-jet printing, food, and cosmetics. The principal chemical classes of these dyes are azo (including premetallized), anthraquinone, triphenylmethane, azine, xanthene, nitro and nitroso. |
| Basic | Water soluble cationic compounds, applied in weakly acidic dyebaths; very bright dyes, used for paper, polyacrylonitrile, modified nylons, modified polyesters, cation dyeable polyethylene terephthalate and to some extent in medicine too. Originally they were used for silk, wool, and tannin-mordanted cotton. The principal chemical classes are diazahemicyanine, triarylmethane, cyanine, hemicyanine, thiazine, oxazine and acridine. |
| Direct | Water soluble, anionic compounds; can be applied directly to cellulosics without mordants (or metals like chromium and copper), used in the dyeing of cotton and rayon, paper, leather, and, to some extent to nylon. Generally the dyes in this class are polyazo compounds, along with some stilbenes, phthalocyanines and oxazines. |
| Reactive | Water soluble, anionic compounds; largest dye class, generally used for cotton and other cellulosics, but are also used to a small extent on wool and nylon. These dyes form a covalent bond with the fiber and contain chromophoric groups such as azo, anthraquinone, triarylmethane, phthalocyanine, formazan, oxazine, etc. Their chemical structures are simple, absorption spectra show narrower absorption bands, and the dyeings are brighter making them advantageous over direct dyes. |
| Disperse | Water insoluble, used mainly on polyester and to some extent on nylon, cellulose, cellulose acetate, and acrylic fibers. Since they are water-insoluble nonionic dyes used for hydrophobic fibers from aqueous dispersion. They generally contain azo, anthraquinone, styryl, nitro, and benzodifuranone groups. |
| Sulfur | Organic compounds containing sulfur or sodium sulfide, used for cotton and rayon and have limited use with polyamide fibers, silk, leather, paper, and wood. They have intermediate structures and though they form a relatively small group of dyes the low cost and good wash fastness properties make this class important from an economic point of view. |
| Vat | Water insoluble; oldest dyes; more chemically complex, used for cotton mainly to cellulosic fibers as soluble leuco salts and for rayon and wool too. These water insoluble dyes are with principal chemical class containing anthraquinone (including polycyclic quinones) and indigoids. |

The industrial developments through recent years have left their negative impressions on the environmental society; among these industries are the dyestuff, textile, printing, papers, leather, cosmetics as well as many others that use dyes and dying process to produce their finishing products. [7] Approximately 10,000 dyes and pigments are used in industries and over $7 \times 10^5$ tons of these dyes are produced annually. [8] In a typical textile dyeing process it's required to desize, scour, bleach, dye, finish and dry the product to complete the operation, typically in most of these steps, water washing and rinsing is required, hence generating large amounts of effluents and waste water reaching an average of 100-170 L/kg of cloth processed. [9]

Due to the fact that not all dye molecules bind to the fabric or the finishing product in the dying process, the generated effluents may contain 2% to 50% of the used dye, depending on the dye type and the dyed product. [10] These dye industry generated effluents contain amounts of waste dye that cannot be underestimated with, since low concentrations of the dye, as even low as 1 mg/L, may be considered as unfit for human consumption [11] such as washing, cleaning and drinking due to the imparted color from the dye. Furthermore, these dyes can exhibit toxicity on the aquatic life and may bring severity on

their life span by reducing the amount of the transmitted light and having the tendency to chelate with metal ions bringing about micro-toxicity to fish and other organisms. [12,13] It's also worth mentioning that large part of the dye along with its breakdown products have been considered with their toxicity, mutagenicity and carcinogenicity. [14,15]

Most of the dyes are composed of aromatic related compounds, as the azo dyes (dieazotized amine coupled to an amine or phenol) [16] that stand for the vast majority group of dyes and at least 3000 of them are being used as colorants in food, textile, paper, cosmetics and pharmaceuticals industries. [14] Due to the complex chemical structure of the vast majority of these dyes lies the fact that most of the dyes are stable to photo-degradation, bio-degradation and oxidizing agents, [17] hence giving rise to an emerging environmental challenge in the removal of the dyes from waste water and the treatment of dye in industrial effluents.

## 1.2 Treatment Methods of Dye Contaminated Water

Waste water treatment is regarded as an essential field in environmental sciences. Water treatment and purification methodologies have been growing vastly and are being continuously optimized

through various criteria depending on the water source, treated water use, type of pollutants and the feasibility of implementing the treatment method on the waste water source.

So far, various treatment procedures have been applied in the removal of dyes from waste waters. These include coagulation, chemical oxidation, ozonation, precipitation, ion-exchange, membrane filtration, electrochemical methods, reverse osmosis, and aerobic and anaerobic microbial degradation.[7,18] However, each of these methods suffer from one or more limitation, such as the high energy cost and the formation of by-product in the oxidation method, adsorbent regeneration and disposal requirements in the ion-exchange method, high sludge production and the formation of large particles in the coagulation method, the short half-life in the ozonation method, the concentrated sludge production in the membrane filtration method.[19] Moreover, none of the above methods can be considered to possess the potential of complete dye removal.[18] Apart from the previous methods, dyes are reported to be effectively removed using adsorption processes,[7,18] which are considered as the most effective water treatment method due to the ease of operation and the availability of a wide range of various adsorbents.[20] Adsorption can

be considered as a method of separation on a laboratory scale as well as industrial scale. [21] Currently, iron nanomaterials (basically those based on iron oxides) are playing an important role in this regard.

Another important area in which iron nanomaterials are being tested is the treatment of large bodies of surface and subsurface water. In this field, water treatment methods can be categorized into two general areas: *ex-situ* methods and *in-situ* methods. Traditionally, the former method is implemented via Pump and Treat systems (PTS). In this method, water is extracted along with the pollutants from the source and then treated outside that source. The later methods are carried on by treating the water inside its source. Nowadays emerging important options include installing Permeable Reactive Barriers (PRB's), and direct injection of the treating material into the water aquifer.

The pump and treat system (PTS) as illustrated in Figure 1.1 [22] consists of wells or drains used for extracting water, usually from ground sources, and then treating the water using aboveground treatment facilities, [23] the PTS provides a quick initial removal of contaminants from water but results in a steady slow removal in the

long term. [24] The main drawbacks of such systems are the aquifer geological dependency to achieve the remediation goals, the slow installation/operating conditions and the high cost. [22]
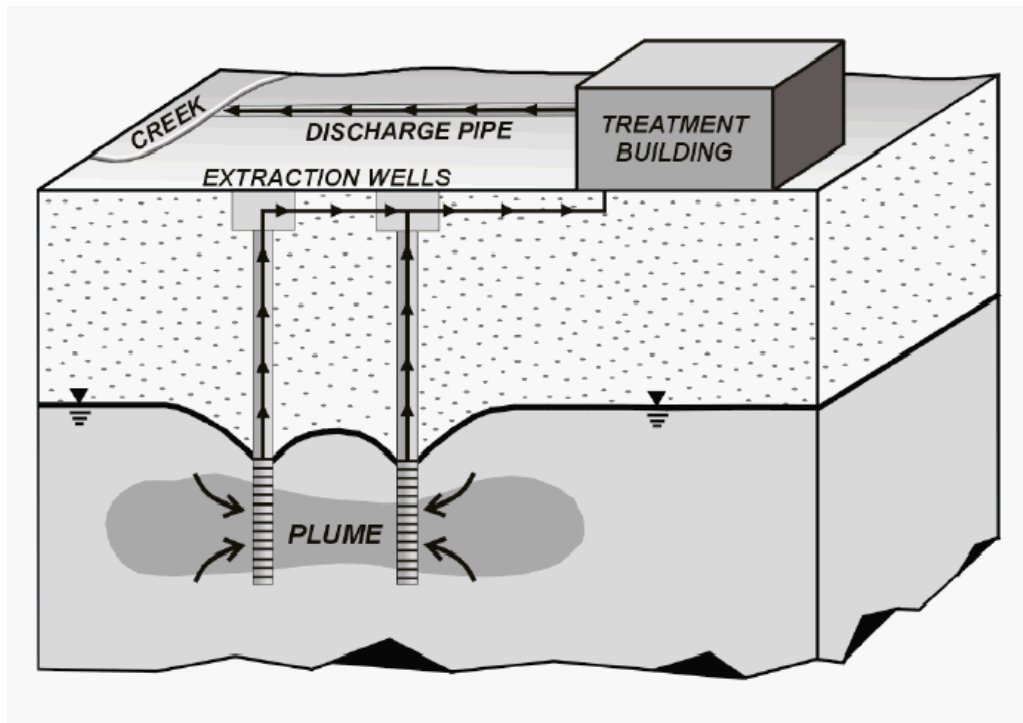


**Figure 1.1 A typical diagram of Pump and treat system (PTS)** [22]

On the other hand, *in-situ* treatment methods imply the treatment of water inside its original source by injecting reactive treating materials inside the aquifer. There have been several treating materials injected inside ground water aquifers, and iron nanoparticles are one of those. The use of iron nanoparticles in injection systems is illustrated in Figure 1.2. [25] This option is considered to yield effective transformation of a wide variety of pollutants, and to be inexpensive

and nontoxic. [25] Iron nanoparticles with palladium nanoparticles (one type of the so-called bimetallic nanoparticles) were implemented in a field study by directly injecting them into groundwater, the injectable nanoparticles were reported to provide enormous flexibility. [26] This material can be injected into the subsurface as water slurries using gravity flow or moderate injection pressures. There is no need to construct specialized injection wells. Some of the particles could be adsorbed on aquifer materials, generating a diffuse passive reactive zone. [26]
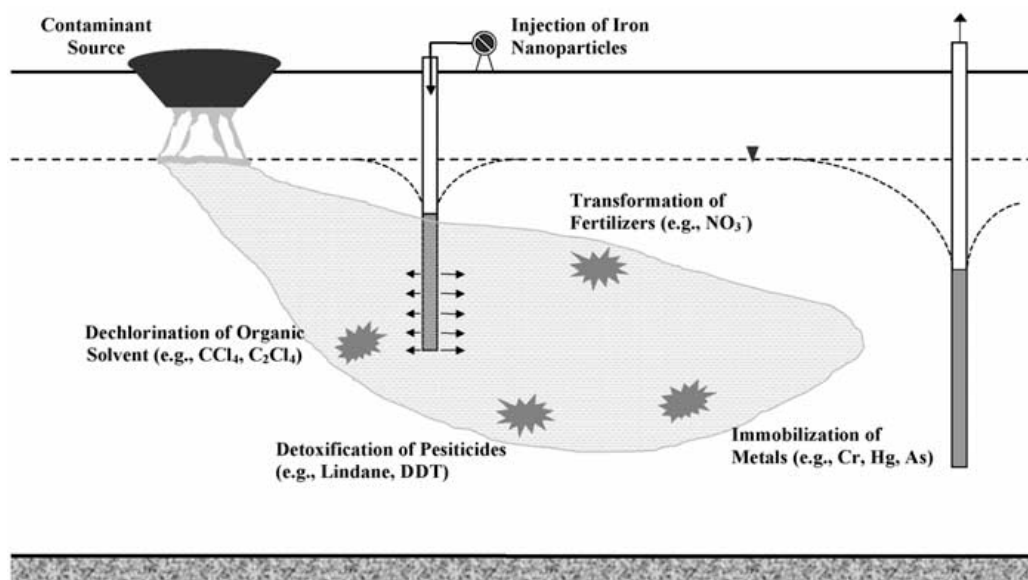


**Figure 1.2 *In-situ* water treatment via direct injection** [25]

Another important *in-situ* water remediation option is the installation of permeable reactive barriers (PRB's), which currently stand as an emerging alternative to the traditional PTS. [27] PRB's are

considered to overcame the PTS drawbacks by providing a better longevity in terms of water treatment for years and decades, ease of installation and operation, and the minimal material and energy requirements. [24] A typical construction of a PRB, as illustrated in Figure 1.3 [28] contains or creates a reactive treatment zone that intercepts and remediates the contaminant plume by various means depending on the reactive material inside the PRB. There have been numerous reactive media employed in the PRB's such as zero valent iron (ZVI), cast iron, steel wool, amorphous ferric oxide, zeolite, activated carbon, limestone and others. [29] However, most PRB's were employed using pure zero valent iron powder (ZVI). According to an EPA survey in 2002, about 55% of the installed PRB's were using ZVI as the reactive media for water treatment. [28]
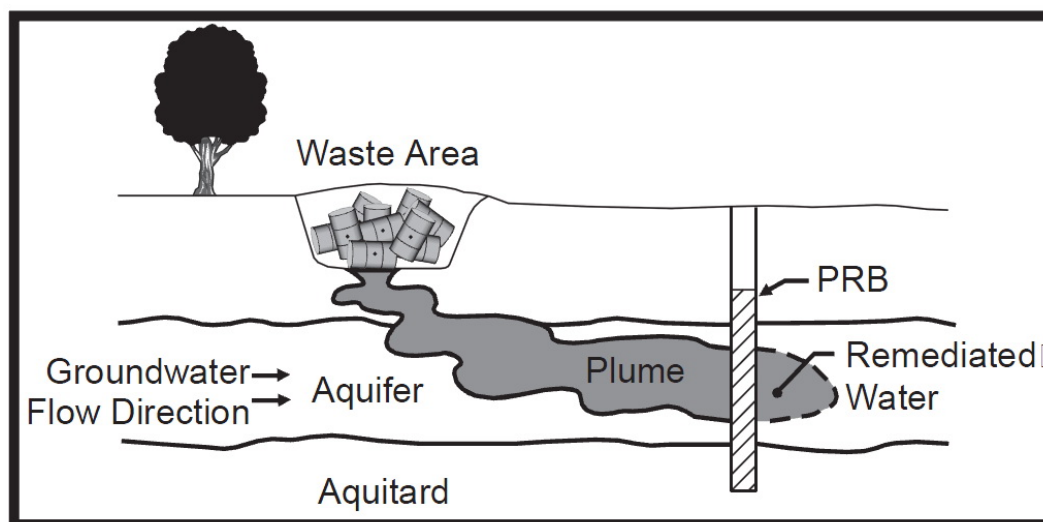


**Figure 1.3 A typical diagram of Permeable reactive barrier (PRB)** [28]

The use of ZVI in PRB's was proven to be efficient toward the removal of various contaminants from waste water; such as dissolved metals, [30] acid-mine drainage, [31] dissolved nutrients, [32] inorganic species [27] and chlorinated organic compounds. [33]

As it is always the case, there are increasing demands which require higher quality water treatment methodologies utilizing less energy and lower treatment cost. Nanotechnology offers numerous opportunities to develop the next generation water treatment methods. [34,20] The breakthrough of using ZVI in its nanoscale form (the so called iron nanoparticles or nano zero valent iron "nZVI") started in 1997 with Wang and Zhang. [35] Their use of nZVI instead of ZVI provided, as with any nano scale system, a much higher surface area to weight ratio and as such higher reactivity ratios. This has given rise to consecrate the novelty of the nano world to meet the ever increasing demands for better water treatment systems.

The next section contains a brief review on iron and its nanoscale form (nZVI), with an overview on its use for water treatment from various pollutants.

## 1.3  Nano Iron and Its Based Materials

Iron is the transition metal of atomic number 26 designated with the symbol Fe, being placed in the 8th group and the 4th period of the periodic table. The element occurs in different isotopes, with $^{56}$Fe being the most abundant and stable isotope. Iron is considered to be the 4th most abundant element in the earth's crust. [36]

Iron, like other group 8 elements, can possess a wide range of oxidation possibilities ranging from -2 to +6. However, iron can exist mainly through the oxidation states +2 and +3 in the presence of water and/or oxygen according to the redox potentials of Fe, as indicated in Table 1.2. [37] In its elemental form, Fe reactive and can be oxidized immediately in atmospheric oxygen to form mainly Magnetite, $Fe_3O_4$, and Hematite, $Fe_2O_3$ in a reaction termed as corrosion. This corrosion reaction occurs mainly on the outer surface of Fe exposed to air's oxygen. The outer surface can develop oxyhydroxide (-OOH) groups yielding goethite, lepidocrocite and others. In the presence of liquid water, these groups can undergo protonation or deprotonation, depending on the pH of water.

**Table 1.2 Standard reduction potentials of iron species** [37]

| Redox Reaction | $E^0$/V |
|---|---|
| $Fe^{2+} + 2e^- \longrightarrow Fe^0$ | -0.447 |
| $Fe^{3+} + 3e^- \longrightarrow Fe^0$ | -0.037 |
| $Fe^{3+} + 1e^- \longrightarrow Fe^{2+}$ | 0.771 |

Zero valent iron (ZVI) is a term that refers to iron material in which the amount of oxide is very small and is confined to the outermost part of the surface. This material is characterized by its high reducing ability toward various types of water contaminants. As mentioned previously, ZVI is widely employed in PRB's facilities.

At first use, ZVI showed its effectiveness toward the dehalogination of chlorinated ethanes, ethenes and methanes, [38] then it was proven with its potential toward the removal of various priority pollutants, including metals, [30,39] polychlorinated biphenyls, [40] chlorinated pesticides, [41] nitro aromatic compounds [42] and nitrates. [43]

As stated in the previous section, the ever increasing demands for better and more efficient water treatment methodologies brought about the manipulation of using the reactive ZVI in its nano scale form, iron nanopartilcles (here termed nano zero valent iron, nZVI). The higher

reactivity of nZVI when compared with ZVI is imparted mainly from the higher surface area to mass ratio. [44] It was reported that the removal of Pb(II) increased by 29 folds when using nZVI instead of ZVI. [45] Furthermore, as particle size decreases the proportion of surface and near surface atoms increases. Surface atoms tend to have more unsatisfied or dangling bonds with concomitantly higher surface energy. Thus, the surface atoms have a stronger tendency to interact, adsorb and react with other atoms or molecules in order to achieve surface stabilization. [46]

There have been several preparation methods for nZVI or some related iron oxides nanoparticles; including: thermal decomposition of iron pentacarbonyl, sonochemical decomposition of iron carbonyl, inert gas condensation, severe plastic deformation, high energy ball milling, ultrasound shot peening, microemulsion (reverse micelle), pulse electrodeposition, liquid flame spray, gas phase reduction, liquid phase reduction and many others ranging from "top down" approaches to "bottom up" approaches. [47,48] Throughout this study the liquid phase reduction method of iron salts using borohydride ions was employed. This method was used by Wang and Zhang, [35] and later by many other research groups with minor modifications. It hasn't been long to prove

the efficiency of nZVI in the removal/degradation of various contaminants from water after its first use in the degradation of trichloroethene and tetrachloroethene from aqueous solutions. [35] Since then nZVI has been shown to be  highly effective in the removal and/or degradation of numerous chemical pollutants, including: β-lactam based antibiotics like amoxicillin and ampicillin, [49] azo dyes like methyl orange, [50] chlorinated pesticides like lindane (γ-hexachlorocyclohexane), [51] organophosphates like tributyl phosphate, [52] nitroamines like RDX (hexahydro-1,3,5-trinitro-1,3,5-triazine), [53] nitroaromatics like TNT (2,4,6-trinitrotoluene), [54] chlorophenols like *p*-chlorophenol, [55] polyborminated diphenyl ethers like decabromodiphenyl ether, [56] polychlorinated biphenyls, [57] inorganic anions like nitrate [58] and perchlorate, [59] alkaline earth metals like barium [60] and beryllium, [61] transition metals like cobalt [62], copper [63] and nickel, [64] post-transition metals like zinc and cadmium, [65] metalloids like arsenic [66] and selenium; [67] and actinides like uranium [68] and plutonium. [69]

Due to the significant variations in the chemistry of the contaminants that are removed/degraded using nZVI, there have been several removal/degradation mechanisms and pathways reported in the

literature; including: sorption, complexation, (co)precipitation, and surface mediated chemical reduction. [70]

The nZVI prepared via the borohydride reduction method was found to be in spherical shapes with different sizes, mostly less than 100 nm, and ranging around 60-70 nm. [71] These nanoparticles tend to agglomerate into further chains. [72] Each of these nanoparticles possess a core-shell structure with the inside part being composed of zero valent iron while the outer shell is made of iron (hydr)oxides. [73] Both parts of the core-shell structure (see Fig.1.4) [44] of nZVI can be active in the treatment of water pollutants. The outer (hydr)oxides shell gives rise to sorption reactions, while the core acts as an electron source that promotes chemical reduction of pollutants. [69] It was reported that the thin and distorted (hydr)oxides layer allows electron transfer from the metal core: (1) directly through defects such as pits or pinholes of the shell, (2) indirectly through the shell conduction band, impurity or localized band, and (3) from sorbed or structural $Fe^{3+}$, while the shell acts as an efficient adsorbent for various contaminants. [44]
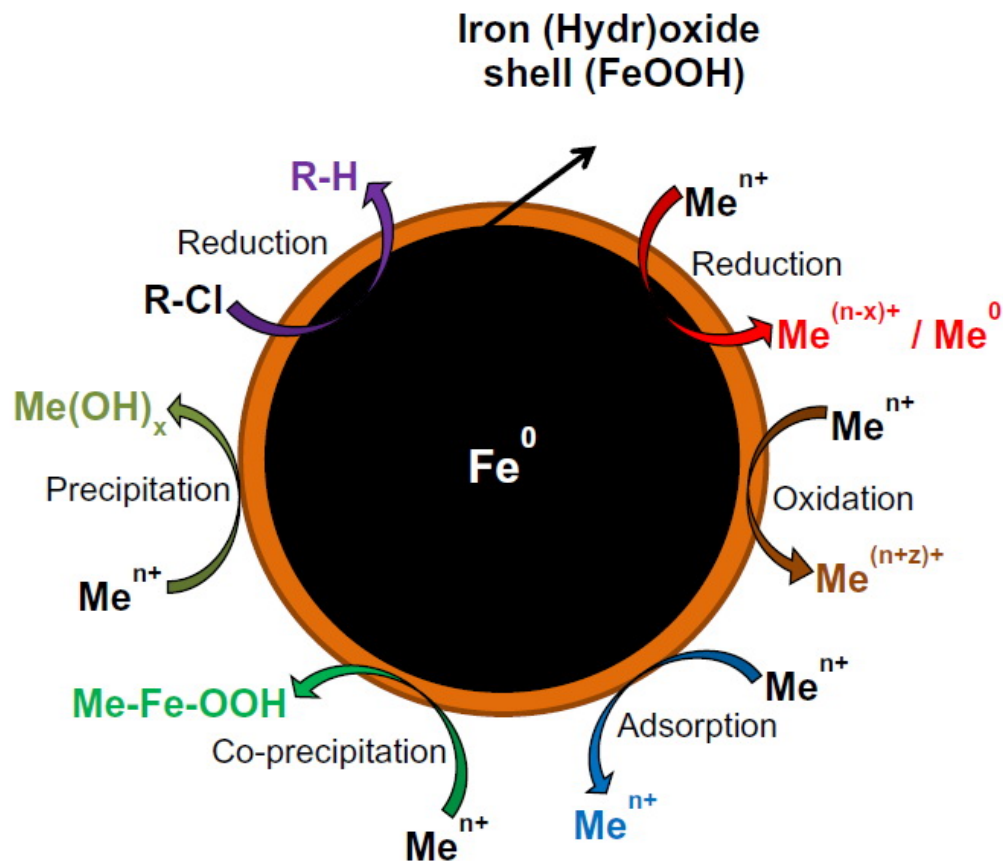
**Figure 1.4 nZVI core shell structure showing various contaminants removal\degradation mechanisms.** [44]

In spite of the optimism surrounding lab-scale results, there are still some drawbacks that preclude from implementing nZVI in large field scale, as in PRB's. The first obstruction arises from the need for kilogram quantities of nZVI in order to be operated as an active material inside PRB's. The price for a kilogram quantity of nZVI is much more higher than ZVI, as in 2005 the nZVI price varied between 20 $ and 77 $ per pound [74] while micro granular ZVI powder would cost less than 1$ per pound.

Another important restriction that impedes implementing nZVI in large field scale lies within the nature of nZVI itself; it's the tendency of nZVI particles to agglomerate into larger particles reaching micro sizes and thus resulting in lower surface area, reactivity and mobility. [75] The classical Derjaguin, Landau, Verwey and Overbeek (DLVO) theory predicts the interaction energy between two identical collides as the sum of the electrostatic repulsion forces (positive by convention) and the van der walls attraction forces (negative by convention). [76] As the separation distances between two collides decreases both of the van der walls attraction and the electrostatic repulsion forces increase in a countered manner. At close separation distances the attraction forces exceed the repulsion ones, creating a minimum energy well in which the two collides become irreversibly attached. [44] However, in the case of nZVI it was shown that attraction forces is primarily dominated by magnetic attraction forces between nZVI particles, [75] bringing about in total higher affinity to form nZVI aggregates as described in Figure 1.5. [44]
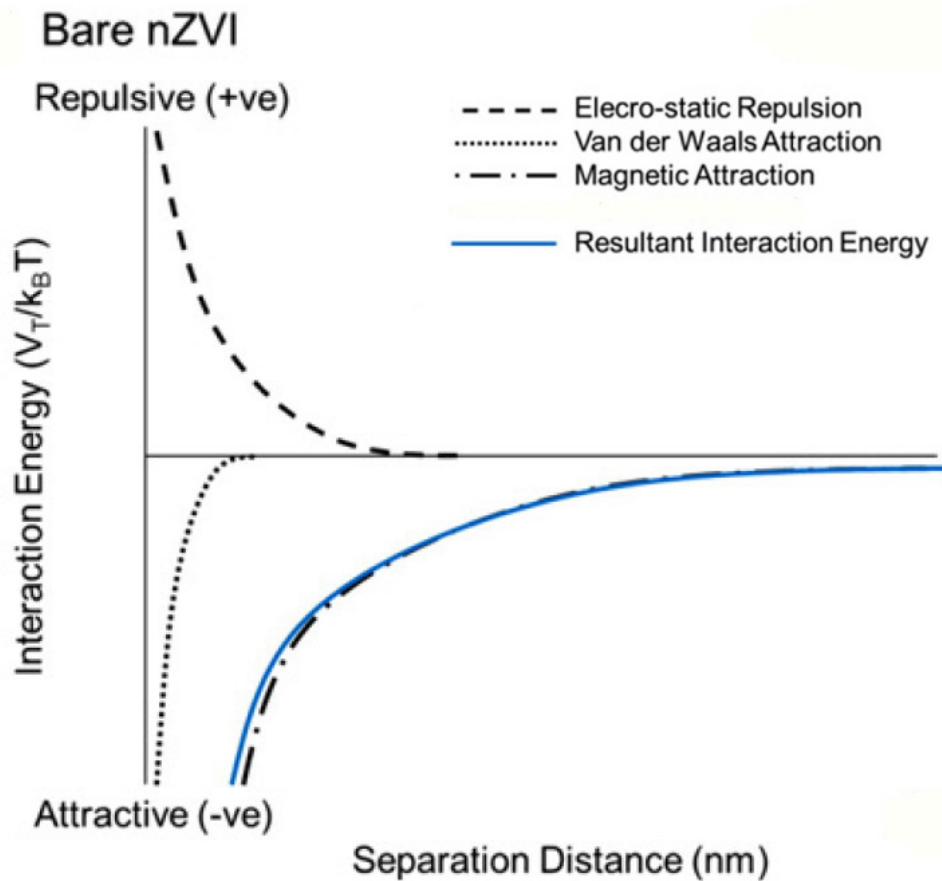
**Figure 1.5 Conceptual model of DLVO interaction forces for nZVI particles** [44]

Furthermore, the iron magnetic momentum not only results in the aggregation of nZVI particles, but also in poorer particles mobility [77] which is urgently needed for environmental purposes as it's generally required from the reactive treatment media to reach as much as possible contaminated areas in direct injection methods, and a minimum level of mobility to avoid shutting the permeability of a PRB.

Considerable efforts have been devoted by researchers worldwide to overcome and minimize the nZVI agglomeration tendency. The efforts to bring about dispersion of nZVI particles can be achieved through stabilizing the nZVI post synthesis or introducing a stabilizer reagent during synthesis. However, in both cases, the stabilization can be regarded as a steric factor that prevents or decreases the nZVI agglomeration as described in the DLVO model in Figure 1.6. [44]
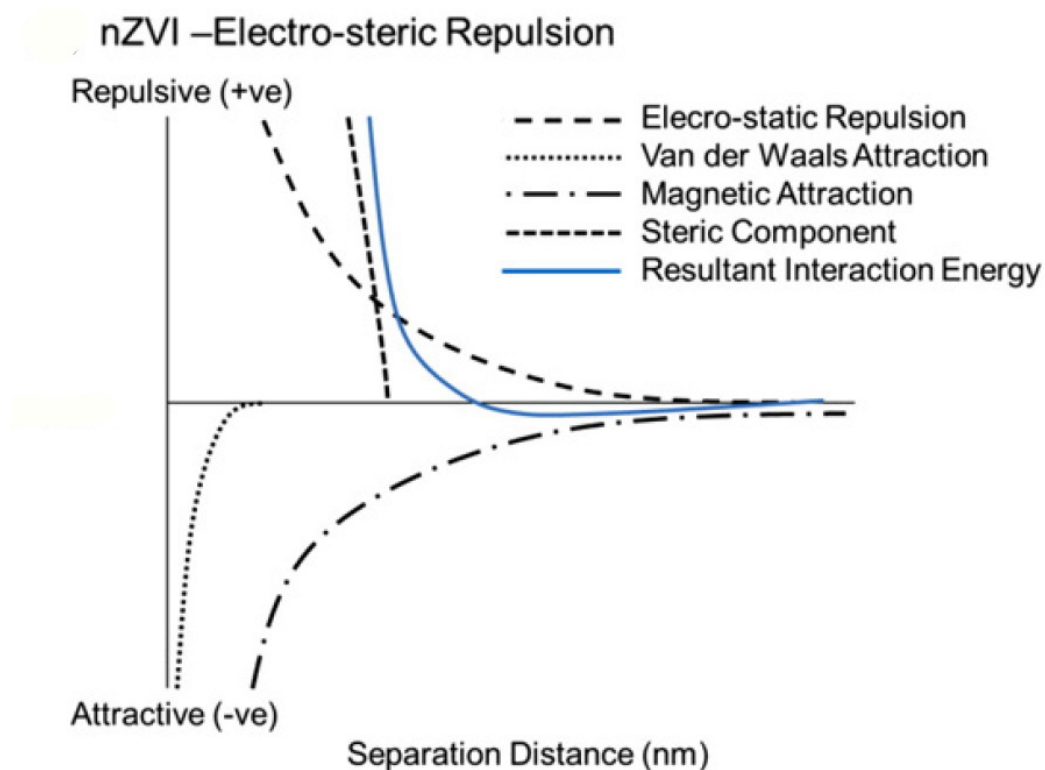


**Figure 1.6 Conceptual model of DLVO interaction forces for stabilized nZVI particles.** [44]

Polymeric coatings using polyelectrolytes have been considered as one of the affordable methods to bring about better nZVI mobility and decrease the particles aggregation via post synthesis surface stabilization. There have been numerous polyelectrolyte coatings used in the stabilization of nZVI including butyl methacrylate, [78] carboxymethyl cellulose, [79] guar gum, [80] poly(4-styrenesulphonate), [81] polyacrylic acid, [82] polyaspartate, [79] polyoxyethylene sorbitan monolaurate, [83] polymethylmethacrylate, [78] polymethacrylic acid, [78] polystyrene sulphonate, [79] polyvinyl alcohol-co-vinyl acetate-co-itaconic, [84] triblock copolymers [85] and xanthan gum. [86] The stabilized nZVI particles were studied in the removal of various pollutants at a lab bench scale and produced results with variable efficiency in the means of mobility and water treatment. However, it was noted that with post synthesis stabilization that depends on physically adsorbing polymeric coatings in a post synthesis process over the existing nZVI, the reactivity of nZVI toward water treatment has decreased when compared with untreated nZVI. This is primarily due to blocking the reactive site on nZVI from the stabilizing polymeric coatings. [87]

One example of the stabilization process during synthesis involves the preparation of nZVI in the presence of a stabilizing agent,

as in using water soluble starch during synthesis to obtain surface stabilized nZVI with Pd having less agglomeration rate and greater dechlorination power. [88] The same approach has been employed using natural extracted polyphenols from green tea [89] and sorghum bran [90] as a reducing agent instead of borohydride, in which the polyphenols also served as a capping agent for produced nZVI. [89]

The use of solid supports during the synthesis of nZVI has been tested to prepare composites containing dispersed nZVI. Several solid supports have been used so far, including: natural clays as kaolinite, [91] bentonite, [92] and palygorskite, [93] alumina, [94] ferregels resin, [95] silica, [96] cation exchange resin, [97] NaY zeolite, [98] zeolite, [99] multiwalled carbon nanotubes, [100] activated carbon, [101] exfoliated graphite, [102] chitosan [103] and carbon microspheres. [104] The composites of nZVI on solid supports have been investigated for the removal of various contaminants and some of them showed an increase in efficiency when compared with pure nZVI particles, giving rise to a versatile class of nano-composites that can be implemented in large field scale water treatment systems.

## 1.4 Literature Review

This section attempts to survey the application of nZVI and its composite materials in the removal of various dye types. The aim here is to provide an overview about the main results and to establish a basis for comparison of the data and literature and the data obtained in this study.

Microscale iron powder (ZVI) was reported to be efficient in the removal of various dyes. [105] By virtue of its enhanced reactivity and larger surface area, nanoscale iron would be expected to convey large potential for dye removal from water media. In spite of the breakthrough of using nZVI for the dehalogenation of chlorinated organic compounds in 1997, [35] less research has been conducted on dye removal using nZVI, and the first plain research on this issue did not come to the scene till about 10 years thereafter. nZVI prepared via borohydride reduction was employed in the removal of the dye acid black 24, a multi azo linkage anionic dye, under various experimental conditions. [106] The dye removal rate constants were reported to be within $0.046 - 0.603$ min$^{-1}$ for nZVI dosages of $0.0335 - 0.3348$ g L$^{-1}$,

and the largest dye removal capacity was found to be 609.4 mg dye per g nZVI.

In another study, [107] the removal of acid black 24 higher dye removal percentages were achieved when the addition of nZVI is coupled with either UV irradiation or $H_2O_2$ addition. The addition of nZVI to the UV/$H_2O_2$ process consumed shorter times for total dye removal than using UV/$H_2O_2$ solely. Furthermore, Li and coworkers [108] found that the removal of acid black 24 using nZVI follows a pseudo first order kinetics and the rate constant was reported to increase linearly with nZVI/ZVI concentration and to decrease with particle size. Also In addition, the activation energy for the dye removal reaction was given as 72.3 kJ mol$^{-1}$ within a temperature range of 10-45 ℃, indicating that the surface reaction controls the rate of dye degradation.

The removal of methyl orange, an anionic azo dye, using nZVI was studied by Fan et al. [50] . The study confirmed that the dye removal efficiency was enhanced by increased initial nZVI dosages and reaction temperatures, but decreased at higher initial dye concentrations and elevated pH's. The kinetic analysis showed that the

reaction follows first order kinetics with activation energy of 35.9 kJ mol$^{-1}$.

The removal of reactive black 5 and reactive red 198, which are azo anionic dyes used in actual textile dying, using nZVI was investigated by Satapanajaru et al. [109] under various experimental conditions. Their study agrees with other dye removal studies in reporting higher dye removal rates using increased nZVI dosages as well as lesser reaction rates at higher initial dyes concentrations and elevated pH's. The dye removal reactions followed pseudo first order kinetics and the obtained reaction rate constants were 0.15-1.17 h$^{-1}$ for reactive black 5, and 0.17-1.29 h$^{-1}$ for reactive red 198, respectively. The same study investigated also dyes removal using nZVI supported on sand, silica oxide and biological sludge, and concluded that the dyes removal efficiencies using supported nZVI were higher than 70% within 90 min.

nZVI was successfully applied in the removal of the anionic azo dye Orange II. [110] It was noted that the nZVI was capable of totally degrading the azo dye and achieving total decolorization. However,

nZVI was reported to lack the ability to achieve total mineralization of dye residues, hence $H_2O_2$ was employed for this purpose.

Moreover, nZVI supported on various substrates were employed in the removal of various dyes. Shu et al. [97] prepared a composite of nZVI supported on cation exchange resin via the typical borohydride reduction method and investigated its potential in the removal of acid blue 113, a multi azo anionic dye. The authors found that the dye removal efficiency was dependent on dye concentration and nZVI composite dosage, while the dye removal rate followed a modified pseudo first order kinetics. The observed removal rate constants were determined as 0.137 and 0.756 $min^{-1}$ while using nZVI dosages of 4.9 and 50.8 mg $g^{-1}$, respectively.

The removal of water soluble anionic azo dyes using a cation exchange resin-supported nZVI was also reported by Zhao et al. [111]. It was concluded that the nZVI composite was capable of degrading acid orange 7, acid orange 8, acid orange 10, sunset yellow and methyl orange dyes with decolorization ratios reaching up to 95% in 4 min contact time. The same composite was also used as a filling in column operations to investigate the dye removal under continuous flow. It

was shown that the composite was able to decompose 58%-90% from the dye in the first run, and the authors suggested a column regeneration methodology using iron salts followed by reduction using borohydride.

In another study, nZVI supported on bentonite was reported [112] and shown to be effective in removal of aqueous orange II dye. The composite was suggested as a more efficient material in dye removal compared with nZVI alone, under the same experimental conditions.

Iron nanoparticles prepared via a "greener" method using natural green tee extract were employed as a Fenton catalyst to degrade several dyes including bromothymol blue, [113] methylene blue and methyl orange. [89] Moreover, it was suggested that, as a Fenton catalyst, the greener iron nanoparticles were more effective in the removal of methylene blue and methyl orange, compared with nZVI produced via borohydride reduction. [89]

In another work, nZVI prepared via the borohydride reduction was stabilized using extracted natural biopolymers from Orange's pectin, and was used in the removal of acid yellow 17 from aqueous solutions. [114] It was deduced that the nZVI served as a reducing agent

of the dye, and that the biopolymers served as adsorbents. Moreover, the dye removal percentage varied between 45.6 and 97.8 % depending on the type of the stabilizing biopolymer.

One more interesting example of supported nZVI, is the multiwalled carbon nanotube-reinforced electrospun polymer nanofibers containing nZVI, which showed effective removal of various pollutants including the dyes methyl blue, acridine orange, and acid fuchsine. [100]

Functionalized nZVI using 3-aminopropyltriethoxisilane was reported by Zhang et al. [115] and employed in the removal of acid brilliant scarlet GR and reactive brilliant red K-2BP. The dye removal capacities using this composite were 121.06 mg g$^{-1}$ and 191.5 mg g$^{-1}$, respectively. Furthermore, it was found that the dyes adsorption followed pseudo second order kinetics and fitted adequately with Langmuir adsorption isotherm.

Bimetallic nanoparticles containing iron were prepared with various metals and employed for several environmental purposes. [44] Fe/Cu nanoparticles and Fe/Cu supported on carbon were investigated for the removal of the dye indigo blue from aqueous solutions. [116] The

dye removal rate followed pseudo second order kinetics, and was fitted using Freundlich, BET and Langmuir isotherm models, but correlated mostly using Freundlich model.

Fe/Ni bimetallic nanoparticles were also reported to be effective in the degradation of orange-g azo dye. [117] The bimetallic nanoparticles were produced using the borohydride reduction method. The dye degradation efficiency was dependent on initial dye concentration, pH of the dye solution and the Fe/Ni dosages. The extent of dye removal increased with higher Fe/Ni dosages, but decreased at higher initial dye concentrations and at elevated pH.

The removal of dyes was also investigated on several iron oxide nanoparticles prepared with various methods. [118,119,120] However, since the chemistry of iron oxide differs from nZVI and its based materials, the obtained results are not covered in this survey.

## 1.5 Aim of the Study

This study focuses on the synthesis of iron nanoparticles (nano zero valent iron, nZVI) and nano iron based materials, namely nZVI supported on natural zeolite (Ze-nZVI) and nZVI supported on alumina powder (Al-nZVI) at various solid-support/iron ratios. The

prepared materials were characterized using Scanning Electron Microscopy (SEM) and Transmission Electron Microscopy (TEM) to investigate and compare their nanoscale morphology. X-Ray powder Diffraction (XRD) was used to determine the mineralogical structure of the materials. Energy Dispersive X-Ray Analysis (EDX) and X-Ray Photoelectron Spectroscopy (XPS) were employed to determine the quantitative elemental surface composition and the oxidation states of the surface species. Finally, BET technique was used to determine the specific areas of the prepared materials.

The prepared materials were subsequently used in the removal of methylene blue (as an example of cationic dyes) and methyl orange (as an example of anionic dyes). The dye removal was investigated under various solid-support/iron ratios, contact times, dye initial concentrations and pH values to determine and compare the dye removal kinetics and extent of removal. The dye concentration was monitored using UV-visible spectrophotometry to assess its concentration and Gas chromatography-mass spectrometry (GC-MS) to determine the dye degradation residues.

# Chapter 2

# EXPERIMENTAL

## 2.1  Chemicals and Reagents

Throughout this study iron(II) chloride tetrahydrate, $FeCl_2.4H_2O$, (Aldrich 22029-9), sodium borohydride, $NaBH_4$, (Merck 8.06373), absolute ethanol (J.T. Baker 8006), alumina powder (Fluka 06300) with particle size 50-150 µm, methylene blue (Certistain 15943), and methyl orange (Aldrich 140910) were used without further purifications. Natural zeolite (Inamarble) was obtained from Turkey and iron powder, ZVI, was obtained from a local blacksmith. All aqueous solutions were made using deionized water.

## 2.2  Synthesis of nano Iron and its Based Materials

The preparation of iron nanoparticles (nZVI) and the composites of nZVI supported on zeolite (Ze-nZVI) and on alumina (Al-nZVI) were followed as reported elsewhere [35,94] using the borohydride reduction method.

**2.2.1  Iron Nanoparticles (nZVI)**

For the preparation of nZVI, 5.34 g of $FeCl_2.4H_2O$ were dissolved in 25.0 mL 4:1 ethanol:water solution (20.0 mL ethanol + 5.0 mL water) and kept under magnetic stirring conditions for 15 min. $NaBH_4$ solution was prepared separately by dissolving 2.54 g of the material in 70.0 mL water. Subsequently, the borohydride solution was added to the iron salt solution using a burette under continuous magnetic stirring conditions at a constant addition rate of about 0.5 mL $sec^{-1}$. During the addition of the borohydride solution, the iron solution color started to fade from pale brown to black, $H_2$ gas evolution was observed and a sharp rise in pH was monitored, indicating a successful reduction of $Fe^{2+}$ to $Fe^0$ according to the equation [92]:

$$Fe^{2+} + 2BH_4^- + 6H_2O \rightarrow Fe^0 + 2B(OH)_3 + 7H_2 \uparrow$$
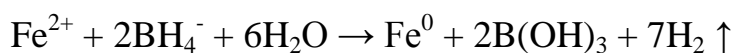
It's worth noting that the molar ratio of the used $BH_4^-$ to $Fe^{2+}$ was 2.5 in order to accelerate the nZVI synthesis reaction since the experimental parameters like pH, stirring rate, borohydride addition rate and external temperature can to some extent influence the

composition and surface properties of the produced nZVI and hence need to be maintained constant during the preparation process to insure consistent samples. [71] After completing the addition of the borohydride, the nZVI solution was kept under stirring conditions for another 15 min. Vacuum filtration was used to harvest the produced nZVI, and while still on suction, the black nZVI powder was washed at least three times with absolute ethanol. Finally, nZVI was dried in the oven at 90 ℃ for 6 hours and stored in amber glass bottle inside desiccator.

## 2.2.2  Alumina Supported Iron Nanoparticles (Al-nZVI)

The same procedure was followed for the preparation of Al-nZVI except that 1.5 g of alumina powder was added to the $FeCl_2$ solution and kept under continuous magnetic stirring for 15 min. before introducing the borohydride solution.

1.5 g of alumina powder was used to prepare 1:1 alumina:nZVI by weight composite, which is referred to in this study as 1Al-nZVI. For the preparation of 2Al-nZVI, 3Al-nZVI and 5Al-nZVI the same preparation procedure was followed by using 3, 4.5 and 7.5 g of alumina powder, respectively.

### 2.2.3 Zeolite Supported Iron Nanoparticles (Ze-nZVI)

As in the preparation of Al-nZVI, 1.5, 3.0, 4.5 and 7.5 g of zeolite were used to prepare 1Ze-nZVI, 2Ze-nZVI, 3Ze-nZVI and 5Ze-nZVI, respectively.

## 2.3 Dye Removal Experiments

Throughout this study, analytical grade 1000 mg L$^{-1}$ stock solution of methylene blue (MB) and methyl orange (MO) was prepared separately by dissolving exactly 1000.0 mg dye in 1.000 L deionized water. Subsequently, the dye solutions where stored in amber glass bottles and further analytical dilutions were made when needed by means of volumetric pipettes and micro pipettes.

Calibration curves in the range of 1.0-10.0 mg L$^{-1}$ for MB and 1.0-25.0 mg L$^{-1}$ for MO where constructed immediately after the preparation of the stock solutions and spared for future use. The calibration curve was obtained by measuring the UV-Visible absorbance at $\lambda_{max}$ for each dye using Varian Cary 50 UV-Visible Spectrophotometer located at the Chemistry Department in Birzeit University, Palestine.

All dye removal experiments where performed using freshly prepared analytical grade dye dilutions prepared from the stock solution. Following the decolorization experiments, the absorbance was measured directly for solution aliquots and in some cases further dilutions were made to account for high absorbance. All the experiments were carried under atmospheric pressure using polypropylene falcon tubes under non-disturbed (without shaking) conditions in thermostat water bath adjusted at 25℃. During dye removal experiments, parallel control dye solutions were placed in falcon tubes without introducing any adsorbent to account for any side dye adsorption.

### 2.3.1 Dye Aggregation Study

Methylene blue (Figure 2.1A) is a heterocyclic aromatic thiazine compound with a molecular formula of $C_{16}H_{18}N_3S^+\backslash Cl^-$. It's solid at room temperature and odorless with a characteristic deep blue color. Methyl orange (Figure 2.1B) is an anionic azo dye with a molecular formula of $Na^+\backslash C_{14}H_{14}N_3O_3S^-$. It has been studied by many researchers as a model of an azo dye.[89] The two dyes where chosen in this study as models for cationic and anionic dyes.

A



B
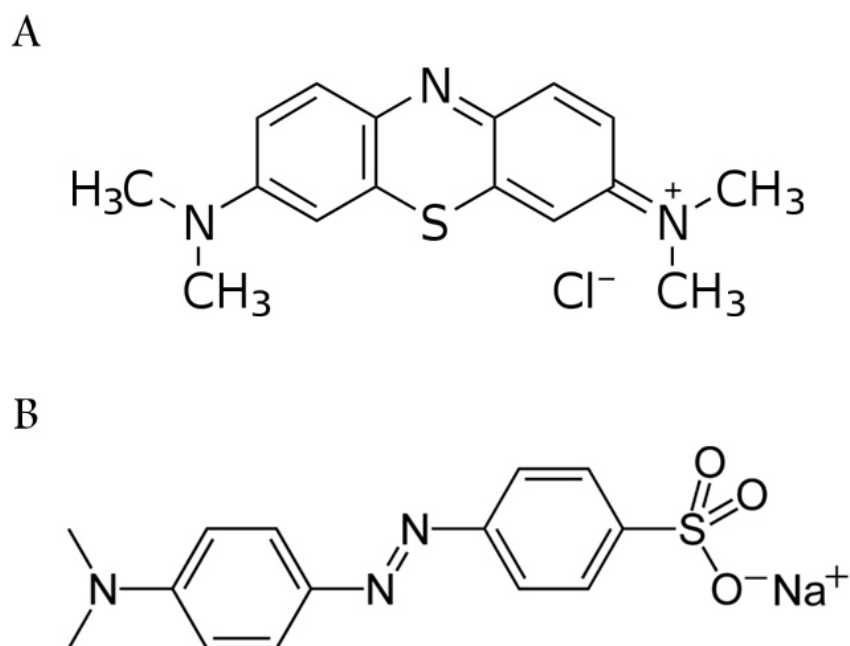


**Figure 2.1 Chemical structure of methylene blue (A) and methyl orange (B)**

In order to investigate the studied dyes aggregation possibility under the working concentrations, several 1.0-10.0 mg $L^{-1}$ MB solutions and 1.0-25.0 mg $L^{-1}$ MO solutions where prepared and their UV-Visible absorbance were recorded against wavelength to determine $\lambda_{max}$ and the possibility of spectral shifts at certain concentrations, moreover, the pH for 10.0 mg $L^{-1}$ dye solution was modified to acidity or alkalinity in order to determine any changes in the absorbance spectra for each dye. Lastly, several dye concentrations were left in contact with nZVI and their absorbance spectra were recorded to assess any effects of nZVI on the dyes aggregation.

**2.3.2  Dye Removal Kinetics**

To determine the dye removal kinetics, 0.100 g of the adsorbent (nZVI, zeolite, alumina, Ze-nZVI or Al-nZVI) was added separately to 25.0 mL portions of 10.0 and 100.0 mg L$^{-1}$ dye solutions (MB or MO). The mixtures were kept in contact under the aforementioned experimental conditions for certain periods that varied for each adsorbent in accordance to its dye removal speed. Subsequently, the dye solution was separated from the adsorbent by means of centrifugation and simple decantation.

For each set of composites with different support:nZVI ratios, 0.100 g was added from each composite separately to 25.0 mL of 100.0 mg L$^{-1}$ for each dye separately and kept in contact for 1 hour to determine the composite with fastest dye removal in order to study its kinetics at various contact times.

**2.3.3  Effect of Initial Dye Concentration**

The effect of initial dye concentration on the extent of the dye removal capacity for each adsorbent was investigated by introducing 0.100 g from each adsorbent separately to 25.0 mL portions of MB or MO dyes at initial concentrations of 5.0, 10.0, 20.0, 50.0 100.0 and

200.0 mg L$^{-1}$. However, from the composites Ze-nZVI and Al-nZVI, only one certain support:nZVI ratio was selected from each set, which was the one with highest dye removal potential. After achieving equilibrium time, which varied from one adsorbent to another, the dye was separated from the adsorbent by means of centrifugation and simple decantation.

The same experiments were also repeated with nZVI, Ze-nZVI and Al-nZVI under the same conditions except only with adjusting the thermostat water bath at 50℃.

## 2.3.4  Effect of pH

The initial pH of 100.0 mg L$^{-1}$ dye solutions (MB or MO) after introducing 0.100 g of nZVI, Ze-nZVI or Al-nZVI was maintained around 3.0, 5.0, 7.0 and 9.0 using 0.1 M HCl and 0.1 M NaOH, and kept in contact for 1 hour under the same experimental conditions. Subsequently, the final pH was measured and the dye was separated from the adsorbent. The absorbance of MO was measured after adjusting the pH of MO aliquots to 7.0, which is the pH at which its standard curve was deduced. The amount of added HCl or NaOH to

maintain the pH were less than 0.2 mL, consequently the effect of volume on dye concentration was neglected.

## 2.3.5 Reusability of the Adsorbents

The longevity and reusability of nZVI, Ze-nZVI and Al-nZVI in the dye removal process was addressed by introducing 0.100 g from the adsorbent to 25.0 mL from each dye separately at 10.0 mg $L^{-1}$ initial concentration under the experimental conditions and keeping them in contact for about 1 hour, then carefully filtering the adsorbent from the dye solution and reusing it in the removal of another 25.0 mL of 10.0 mg $L^{-1}$ dye solution, subsequently, each dye concentration was determined after each separation. The same process was repeated for 7 successive trials.

## 2.3.6 Desorption Studies

The possibility of dye desorption from the used adsorbents was determined by adding 0.100 g from the adsorbent to 25.0 mL of 500.0 mg $L^{-1}$ dye solution and keeping them in contact for 24 hours under the experimental conditions. Then the adsorbents were carefully separated and the dye concentrations were measured. Separated adsorbents were introduced to 50.0 mL deionized water, left in contact

at room temperature, and the desorped dye concentration was determined every 24 hour for the first two days and then every 2 days for the six days thereafter.

### 2.3.7  nZVI as a Fenton Catalyst

nZVI was tried as a Fenton catalyst. In the relevant experiments, the dye removal kinetics (for MB and MO) were determined by introducing 0.100 g nZVI to 25.0 mL of 100 mg L$^{-1}$ dye solution, and 5.0 mL of 10% (v/v) H$_2$O$_2$. The solutions were kept in contact for certain periods that varied with each dye. Subsequently, the dye was separated by centrifugation and simple decantation and tis absorbance was measured.

### 2.3.8  Dye Removal Using a Continuous Column Flow System

The applicability of the adsorbents (nZVI, zeolite, alumina, Ze-nZVI or Al-nZVI) in a continuous column system was investigated in a trial to assess and compare the potency of each adsorbent to be used in large scale water treatment systems like PRB's.

For this purpose, a glass column (Figure 2.2) was constructed by the technician Mr. Azmi Doudin at the glass blowing unit in Birzeit

University. 2.00 g of the adsorbent was placed in the column through which a continuous stream of either 10.0 or 100.0 mg L$^{-1}$ dye (MB or MO) passed and collected into about 2 mL portions, and their absorbance was measured.
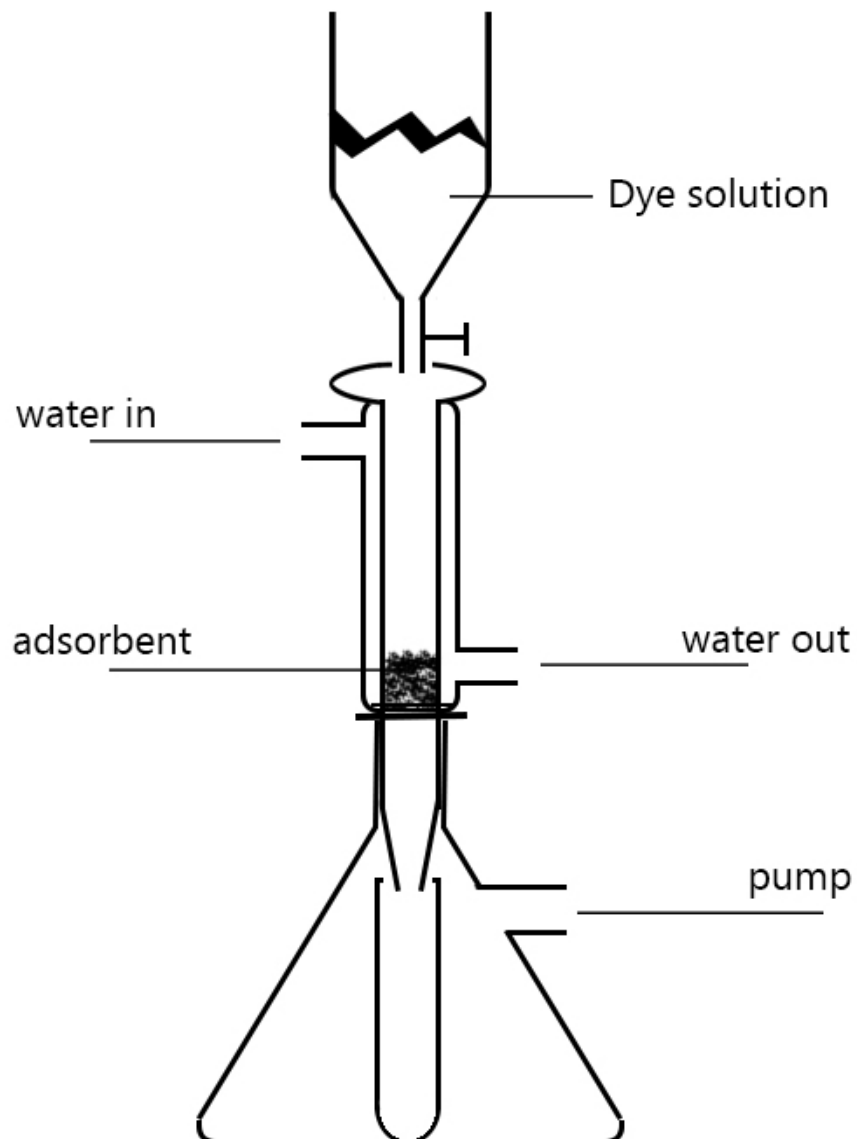


**Figure 2.2 Glass column for dye removal using a continuous flow system**

## 2.4 Characterization Techniques

The characterization of dye solutions and the prepared nZVI along with its based materials (Al-nZVI and Ze-nZVI) is described in the following subsections. The characterization of the iron based materials was carried mainly for 3Al-nZVI and 3Ze-nZVI samples unless otherwise stated.

### 2.4.1 Ultraviolet-Visible (UV-Vis) Spectrophotometry

This study was done using Varian Cary 50 UV-Visible Spectrophotometer located at the Chemistry Department in Birzeit University, Palestine. The spectrophotometer operates on dual beam using a Czerny-Turner monochromator and working at 190–1100 nm wavelength range with approximately 1.5 nm fixed spectral bandwidth, the light source consists from full spectrum Xe pulse lamp, and has dual Si diode detectors.

The spectrophotometer was used to obtain calibration curves of Abs. vs. concentration for MB and MO (Figure 2.3) dyes in the ranges of 1.0-10.0 and 1.0-25.0 mg $L^{-1}$ respectively at $\lambda_{max}$ for each dye which were determined to be 665 and 465 nm respectively. The

absorbance for each dye after every dye removal experiment was obtained using the same instrument and their concentration was accounted for using the previously prepared calibration curve.
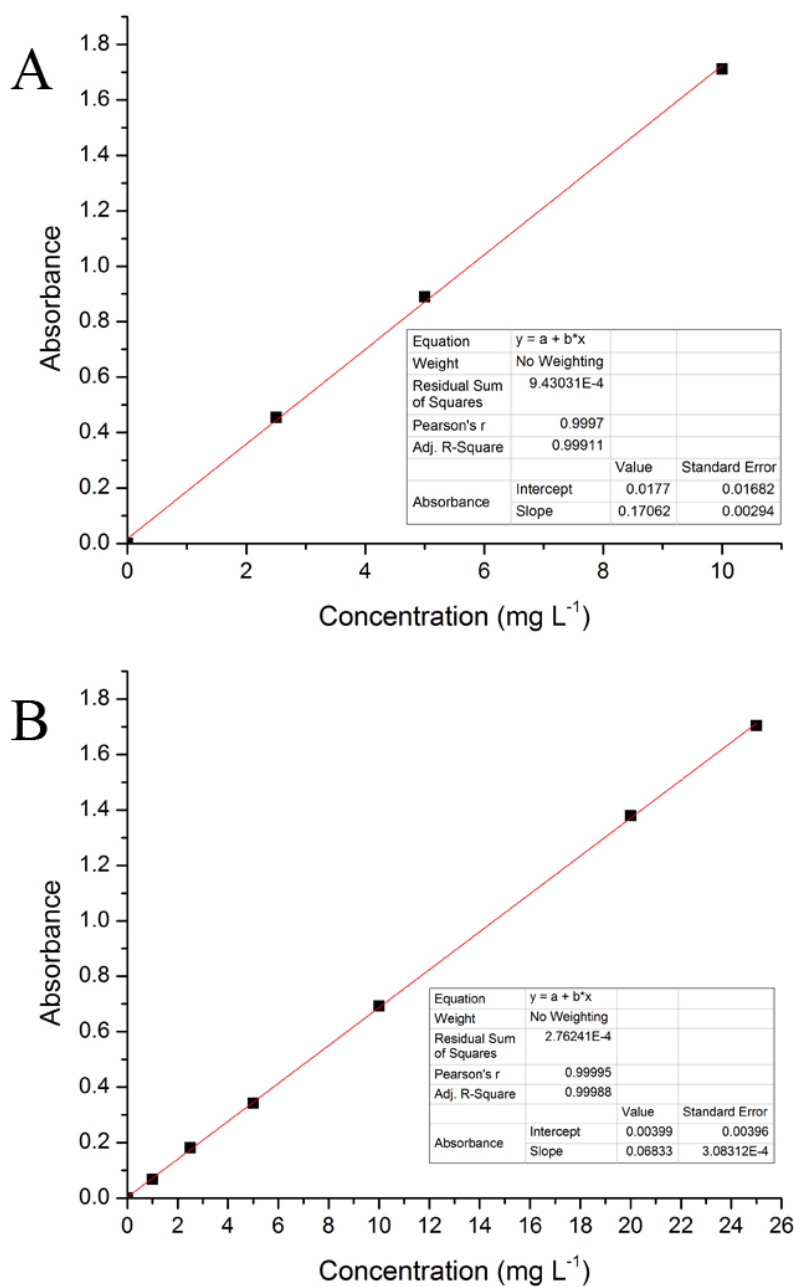


**Figure 2.3 Standard calibration curves for MB (A) and MO (B)**

## 2.4.2 Fourier Transform Infrared Spectroscopy (FTIR)

The FTIR characterization was done using Varian 660-IR Spectrometer located at the Chemistry Department in Birzeit University, Palestine. The spectrometer consists of an air cooled retro-reflector IR source with a collection efficiency of 0.7, a dynamically-aligned Michelson interferometer with an incident angle of $30^0$ as measured from normal on the beamsplitter, and a detector that is composed from deuterated L-alanine doped triglycine sulphate.

IR spectra were obtained for the adsorbents (nZVI, zeolite, alumina, Ze-nZVI and Al-nZVI) before and after both dyes removal experiments. The adsorbent was mixed with potassium bromide, KBr, grinded and pressed into pellets by the aid of vacuum, and then its IR spectrum was recorded in the range of 400-3900 cm$^{-1}$.

## 2.4.3 Powder X-Ray Diffraction (XRD)

Throughout this study X-ray diffraction diagrams were recorded for the adsorbents using Philips X'Pert Pro diffractometer (Panalytical), using the copper Kα-line ($\lambda$ = 1.54060 Å), at 40 kV, 30mA in line-focus mode. The diffractometer was set up with a PW3050/6x goniometer and data were collected from $2\theta = 10°$ to $70°$,

with a step size of 0.02° and a dwell time of 1 s per step. Experiments were run under atmospheric conditions and at room temperature. The instrument is located at Centre of Materials Research in Izmir Institute of Technology, Turkey.

## 2.4.4  Scanning Electron Microscopy (SEM)

Throughout this study, SEM images for the adsorbents where recorded either using Philips XL-30S FEG type instrument located at the Center of Materials Research in Izmir Institute of Technology, Turkey, or Gemini LEO 1530 VP located at the Center of Nanotechnology (CeNTech) in the University of Münster, Germany. The solid samples were first sprinkled onto adhesive carbon tapes supported on metallic disks. SEM images of the samples surface were recorded at different magnifications.

## 2.4.5  Energy Dispersive X-Ray Spectroscopy (EDX)

EDX characterization was carried using the SEM instruments mentioned above. However, Philips XL-30S FEG was employed in spot analysis mode, in which points on the sample's surface were randomly chosen and the elemental composition was revealed, while Gemini LEO 1530 VP was employed in integrated analysis mode, in

which a total area of about 1-3 mm$^2$ on the surface was scanned and the average elemental composition was revealed, moreover, EDX mappings for nZVI where obtained to show the elemental distribution of Fe and O.

## 2.4.6  Transmission Electron Microscopy (TEM)

Throughout this study, TEM images were recorded using ZEISS Libra 200FE located at the Institute of Physics in the University of Münster, Germany. The instrument was operated at 200 kV. The sample was dispersed in chloroform by means of ultrasonic shaker path, subsequently, few drops of the suspension where placed on a holey carbon film supported on copper substrate.

The same instrument was also used to obtain Scanning Transmission Electron Microscopy (STEM) images of the sample by focusing the transmitted electrons beam in a narrow spot and scanning over the sample in a raster, furthermore, the rastering beam was used to obtain EDX mappings of the samples.

## 2.4.7  X-Ray Photoelectron Spectroscopy (XPS)

The XPS measurements were performed using VG Scientific ESCALAB 250 located at the Center of Nanotechnology (CeNTech) in the University of Münster, Germany. The sample was dispersed in chloroform by means of ultrasonic shaker path, subsequently; few drops of the suspension were placed on roughened copper substrate. The XPS was operating using Al kα at 400 W, data acquisition was obtained at $10^{-8}$ mbar to insure a clean sample surface, analysis and manipulation of data were carried using CasaXPS software, the binding energies for the collected photoelectrons were refernced using adventitious C 1s peak at 284.6 eV.

## 2.4.8  Brunauer-Emmett-Teller (BET) Surface Area Analysis

The BET surface area of nZVI and its based materials was determined by BET-$N_2$ method using a Micromeritics Gemini 5 instrument located at the Center of Materials Research in Izmir Institute of Technology, Turkey. The samples were degassed for 3 hours at 353 K to insure clean surface and then pumped using $N_2$ gas.

### 2.4.9 Gas Chromatography – Mass Spectrometry (GC-MS)

GC-MS analysis was used to identify the presence of dye degradation products using Perkin Elmer Clarus 600 model located at the Chemistry Department in Birzeit University, Palestine. The aqueous treated dye solution was extracted by means of solid phase extraction on alumina powder using acetonitrile; subsequently the acetonitrile was dehydrated using sodium carbonate and passed through silica gel packed micro-column. The acetonitrile was injected in the GC-MS instrument; the column temperature was held at 50 ℃ for 2 minutes and was increased from 50 ℃ to 240 ℃ at a rate of 10 ℃ $min^{-1}$.

# Chapter 3

# RESULTS & DISCUSSION

## 3.1  Characterization of Dyes and Synthesized Materials

The characterization results of both dyes (MB and MO) along with the prepared nZVI and its based materials (Al-nZVI and Ze-nZVI) are discussed with details in following subsections.

### 3.1.1  Dye Aggregation Study

UV-visible spectra of MB under the working concentrations (1.0-10.0 mg $L^{-1}$) do show similarity and specific stable $\lambda_{max}$ at different concentrations as can be seen in Figure 3.1, hence indicating the absence of any MB aggregation and the possibility of using MB as a model to study its removal. Moreover, the spectra reveal wavelength matching in all peaks other than $\lambda_{max}$ at different concentrations and so assuring the absence of any dye aggregates or conjugates at the working concentrations.
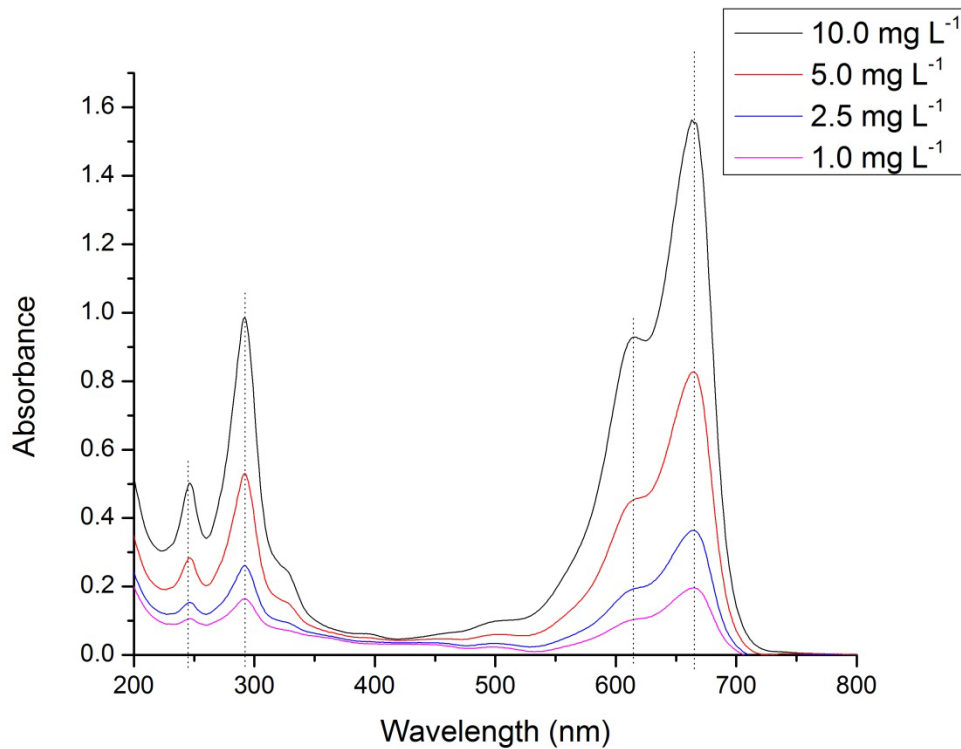
**Figure 3.1 Various MB concentrations absorbance spectra**

In the case of MO (Figure 3.2), the UV-visible spectra reveals a small hypsochromic shift (blue shift) of about 4 nm that can be seen at low MO concentrations, however, due to the nature of the absorbance spectrum of MO, being wide at $\lambda_{max}$ and with small differences in the absorbance values at around ±4 nm from $\lambda_{max}$, the dye can be possibly chosen as a model to study its removal.

Variation in pH of MB solution brought about no differences in its absorbance spectra in terms of peak shape and $\lambda_{max}$ position as shown in Figure 3.3.
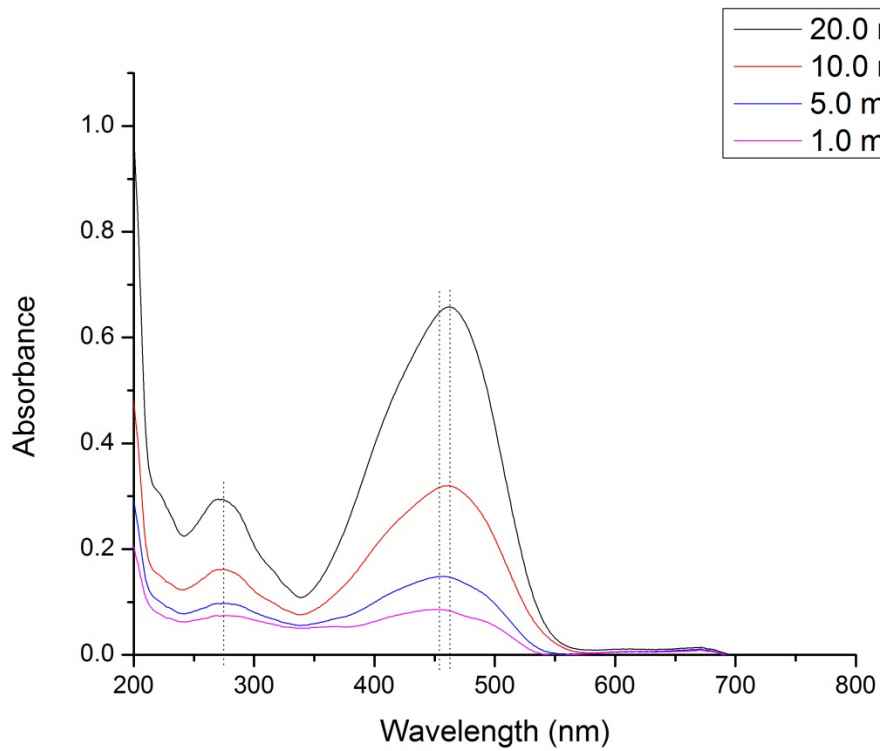
**Figure 3.2 Various MO concentrations absorbance spectra**
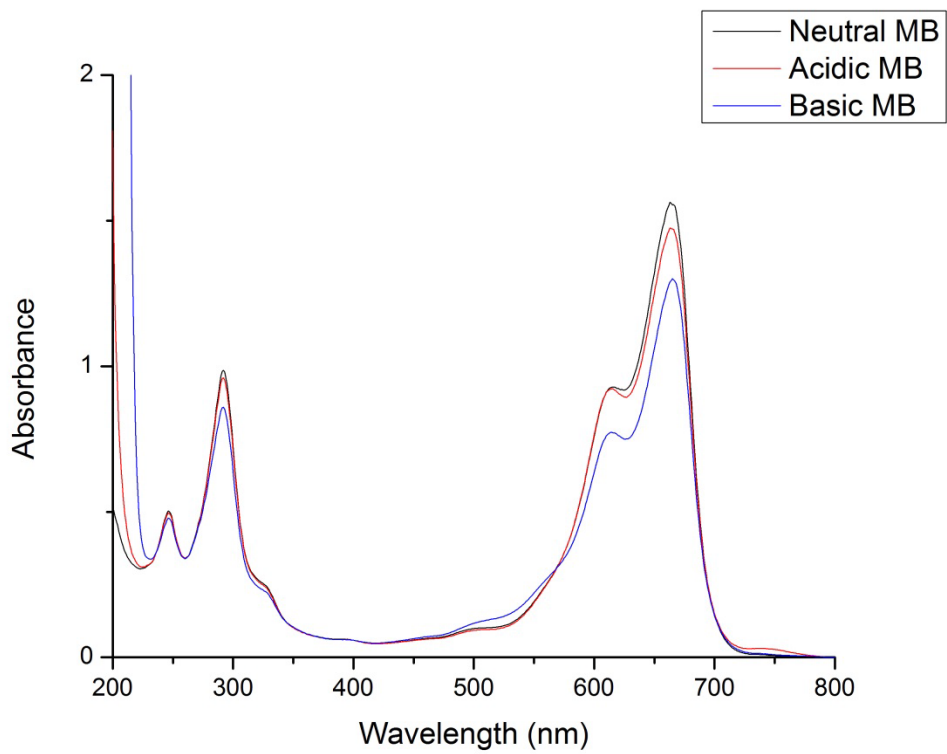


**Figure 3.3 MB solution at different pH**

While MO retained its spectra in the alkaline region (Figure 3.4), its acidic spectra did completely change due to the development of a different structure by attaching $H^+$ to the sulfanilic acid nitrogen in the azo linkage; this phenomenon is the reason behind its use as an acid-base indicator. The acidic MO structure would result in no effect in the study since MO absorbance after adsorbent separation was monitored in the neutral and alkaline region.
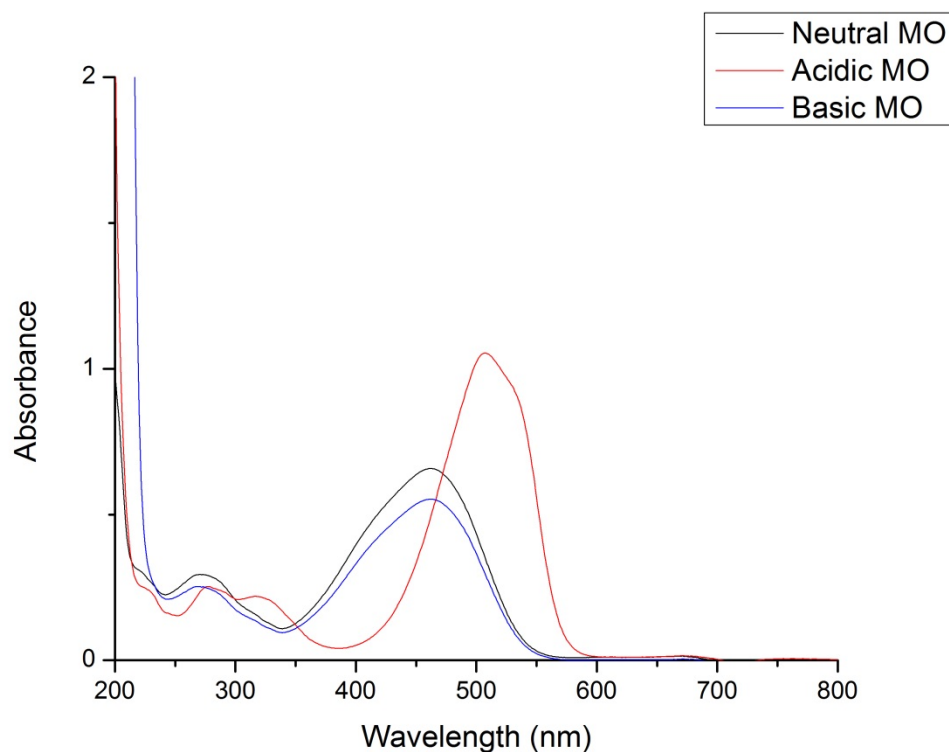


**Figure 3.4 MO solution at different pH's**

After separating MB solution from any nZVI material, its spectrum showed some fluctuation and some differences from the

obtained MB spectra regarding peak shape and $\lambda_{max}$ position. However, the separated MB spectra showed stabilization and spectra similarities at about 10 minutes after separation as can be seen in Figure 3.5. This is believed to occur due to gaining some electrons which were lost by nZVI during its oxidation in the aqueous medium to form leucomethylene blue (LMB), after about 10 minutes, the LMB readily oxidized and lost its electron to reform MB which can be easily measured using its absorbance spectrum. The MB-LMB combination account for the use of MB as a redox indicator.
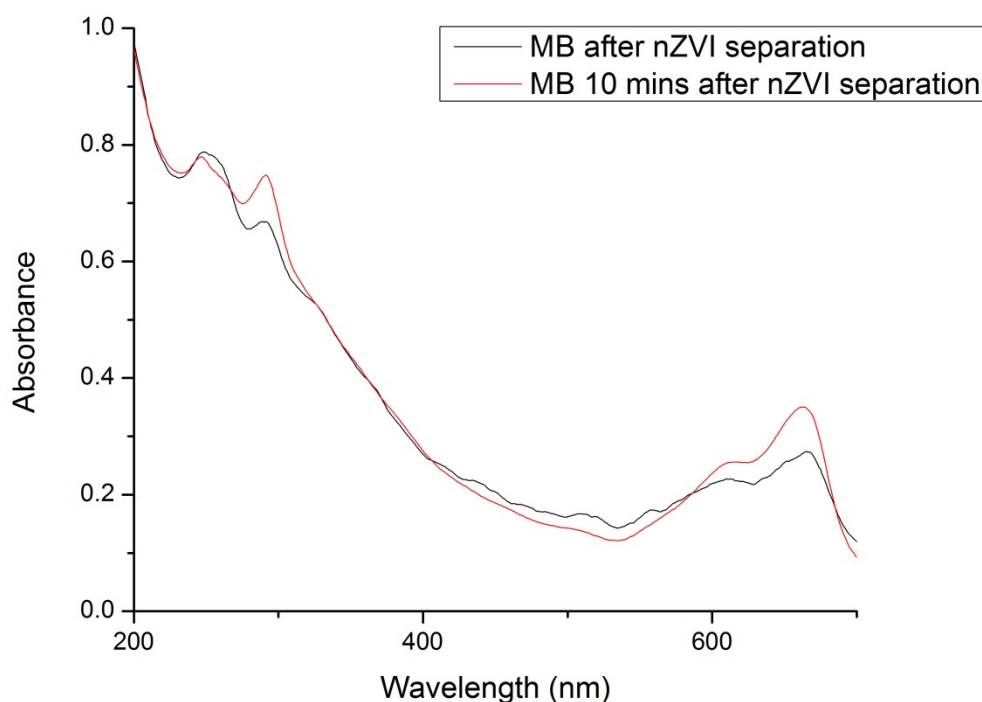


**Figure 3.5 MB spectra after nZVI separation**

The MO spectra showed no changes at the moment of immediate separation from nZVI and every minute thereafter as seen in Figure 3.6.
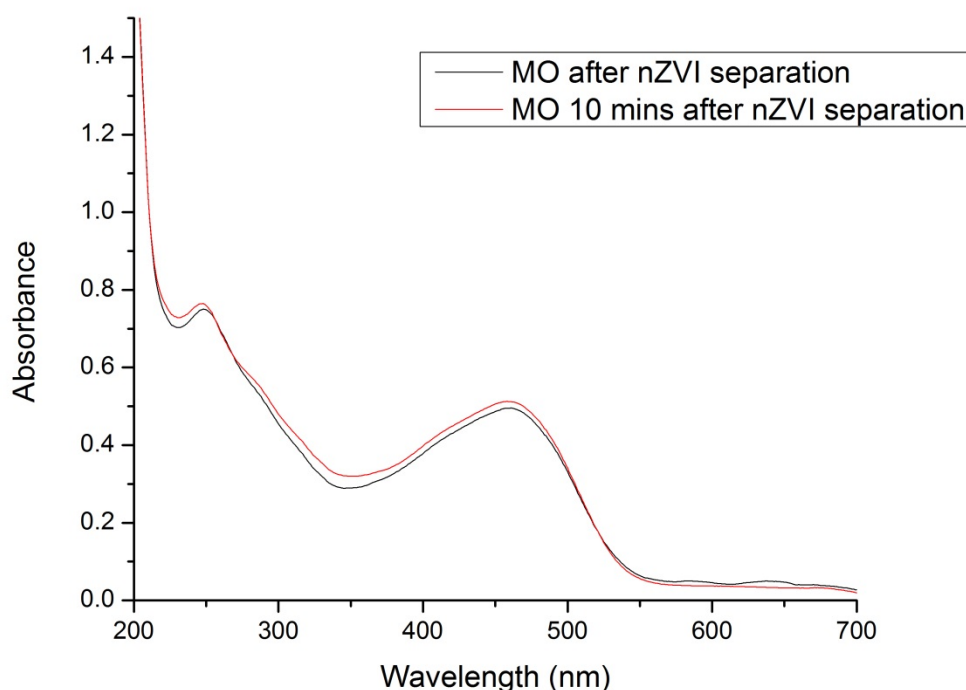


**Figure 3.6 MO spectra after nZVI separation**

## 3.1.2  Iron Nanoparticles (nZVI)

The obtained FTIR spectra for nZVI before and after being used in the removal of MB and MO (here referred to as nZVI MB and nZVI MO) are shown in Figure 3.7. By comparing those spectra at certain wavenumber ranges it can be stated that the broad hydroxyl stretching at around 3500 cm$^{-1}$ was broadened and became more

pronounced in the case of nZVI MB and nZVI MO indicating hydrogen bonding between the nZVI (hydr)oxides surface and the dyes. [121] The same stretching band is present in nZVI spectrum before adsorption is attributed to hydrogen bonding of nZVI with humidity.
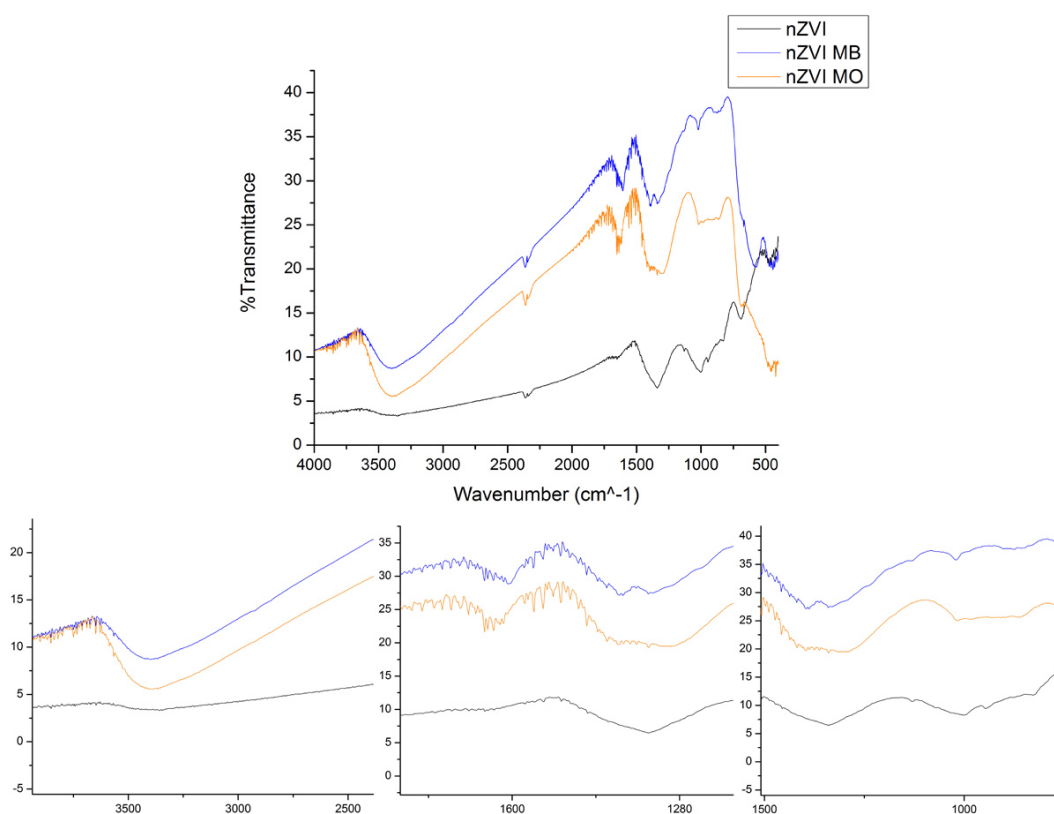


**Figure 3.7 FTIR spectra of nZVI, nZVI MB and nZVI MO**

More characteristic peaks that are observed in nZVI MB and nZVI MO are those in the 1500-1400 cm$^{-1}$ region due to the methyl C-H bending and aromatic C=C stretching of the dyes. Moreover, the appearance of peaks in the 1270-1000 cm$^{-1}$ and 900-690 cm$^{-1}$ due to

aromatic C-H bending indicates the presence of the dyes molecules or dye degradation residues on the nZVI surface.

The structure of nZVI was characterized by XRD to provide evidence about the presence of crystalline zero valent iron along with iron oxides ($Fe_3O_4$) [122] and iron oxyhydroxide (FeOOH). [123] The related XRD pattern is shown in Figure 3.8 for a 1 month aged nZVI sample, however, several reported examples [62] indicated the presence of crystalline nZVI solely in freshly prepared nZVI and the development of iron (oxyhydr)oxides with time.
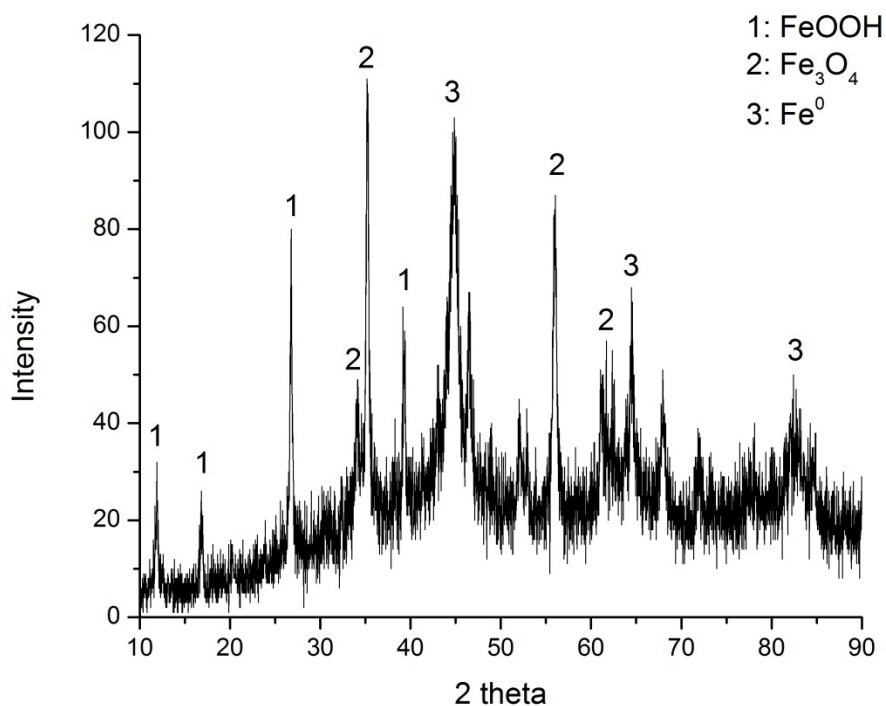


**Figure 3.8 XRD pattern of nZVI showing crystalline iron along with iron (hydr)oxides**

The morphology of the prepared nZVI resembles those reported elsewhere [35] with 50-100 nm spherical particles and being agglomerated into chain like structures due to the magnetic attraction forces between the particles, [75] as seen in the SEM images (Figure 3.9).
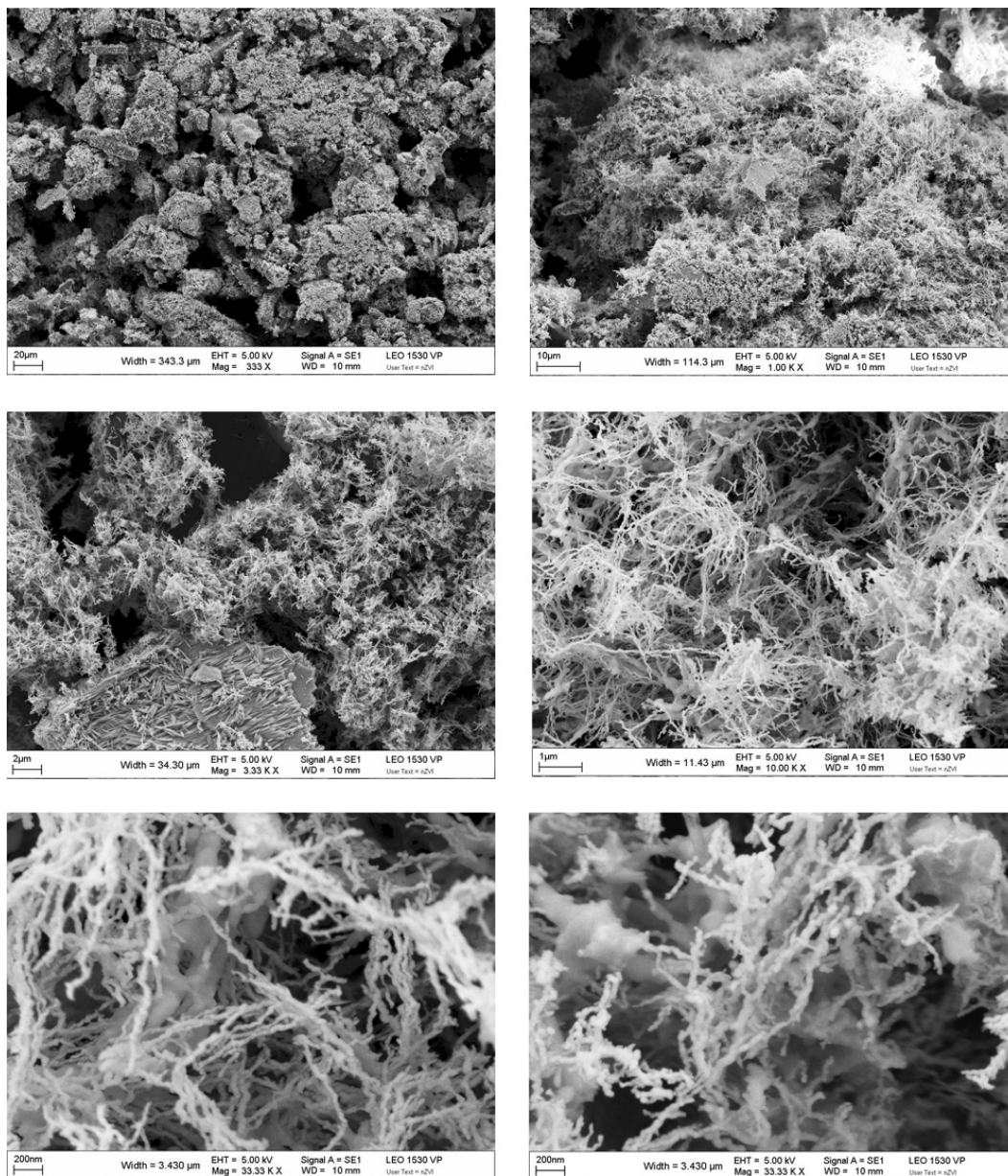


**Figure 3.9 SEM images of nZVI at various magnifications**

The assessment of the surface elemental composition of nZVI was performed using EDX analysis. The characterization results (see Figure 3.10) in integrated mode showed that the % composition by weight of Fe to be around 65% and O by about 24% indicating the presence of iron along with its oxides. Moreover, the EDX spectra showed the presence of small amounts of Na, Cl and C, the former two originate from $FeCl_2$ and $NaBH_4$ which were used as precursors for nZVI in its preparation, while C is believed to be from the carbon adhesive tape that has been used in the SEM measurements.
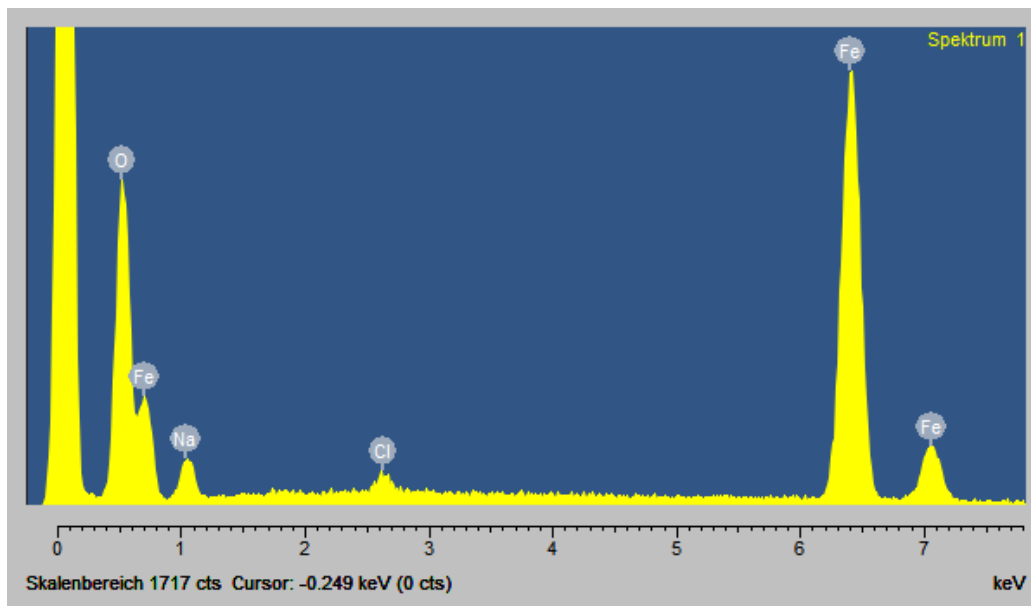


**Figure 3.10 EDX spectrum of nZVI**

Single spot EDX analysis for random selected points confirmed the percentage composition of the integrated mode by showing Fe

composition ranging between 60% and 70%, and oxygen ranging between 15% and 25%. Selected areas EDX analysis for a back-scattered SEM image was used to differentiate between the dark and the light areas (where in back-scattered SEM mode the light areas stand for high atomic number elements and the dark ones for lighter elements). The Fe composition seemed higher than the average in the light area and vice versa in the dark area as demonstrated by Figure 3.11. This is considered to support the idea of having various oxidation degrees on the nZVI surface.
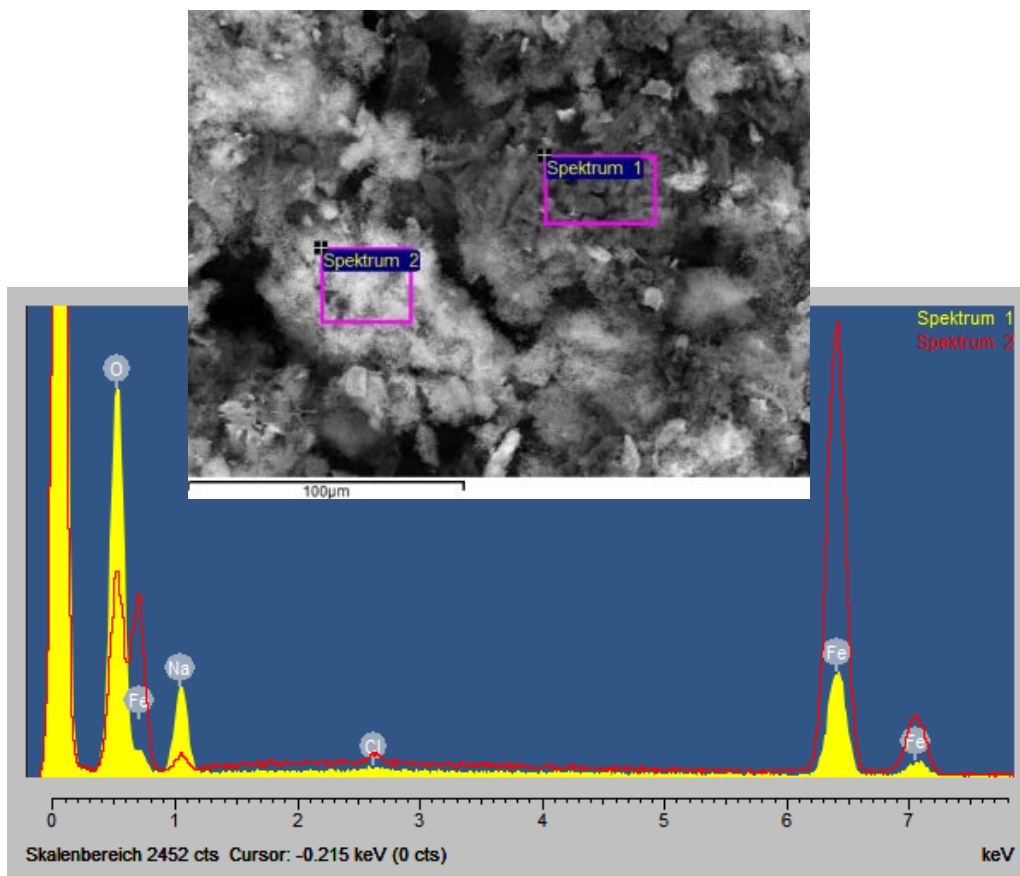


**Figure 3.11 Selected areas EDX spectra of a back-scattered SEM**

In a trial to investigate the topological composition of the nZVI surface and the arrangements of the main elements on it, EDX mappings for Fe, O and Na where acquired for the same back-scattered SEM image (Figure 3.11) to reveal the surface elemental composition. The corresponding EDX mapping images, shown in Figure 3.12, confirmed iron presence in most parts of the surface with elevated oxygen levels in the darks areas. It is noticed that the Na signals are present mainly in the areas where oxygen levels are high, hence indicating its presence as $Na^+$ ions associated with the highly electronegative oxygen.

In order to confirm the obtained picture about the nZVI morphology and structure and have a manifest view about its structure, TEM and STEM analysis were performed for the same nZVI sample. TEM images (Figure 3.13 a and b) clearly reveals the chain like morphology of nZVI particles with different particle sizes averaging around 50 nm, and the same conclusion can be drawn from the STEM images (Figure 3.13 c and d). Moreover, a confirmation about the nZVI core-shell structure (which was detailed previously in section 1.3 and Figure 1.4) can be drawn from Figure 3.13 b by the

palpable inner dark areas which stand for iron and the particles shell light areas that stand for oxygen.
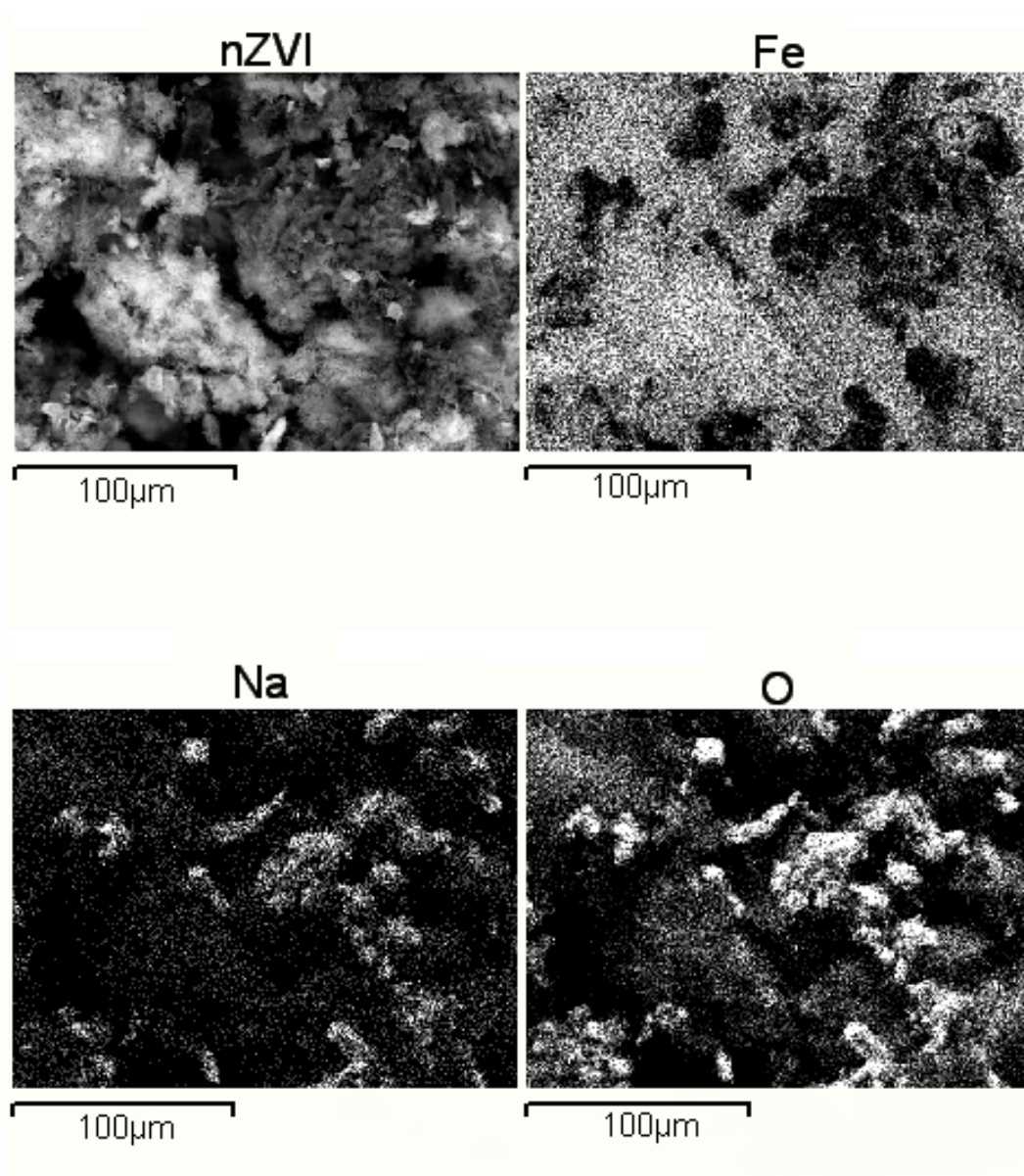


**Figure 3.12 EDX mappings of nZVI showing elemental maps for Fe, O and Na**
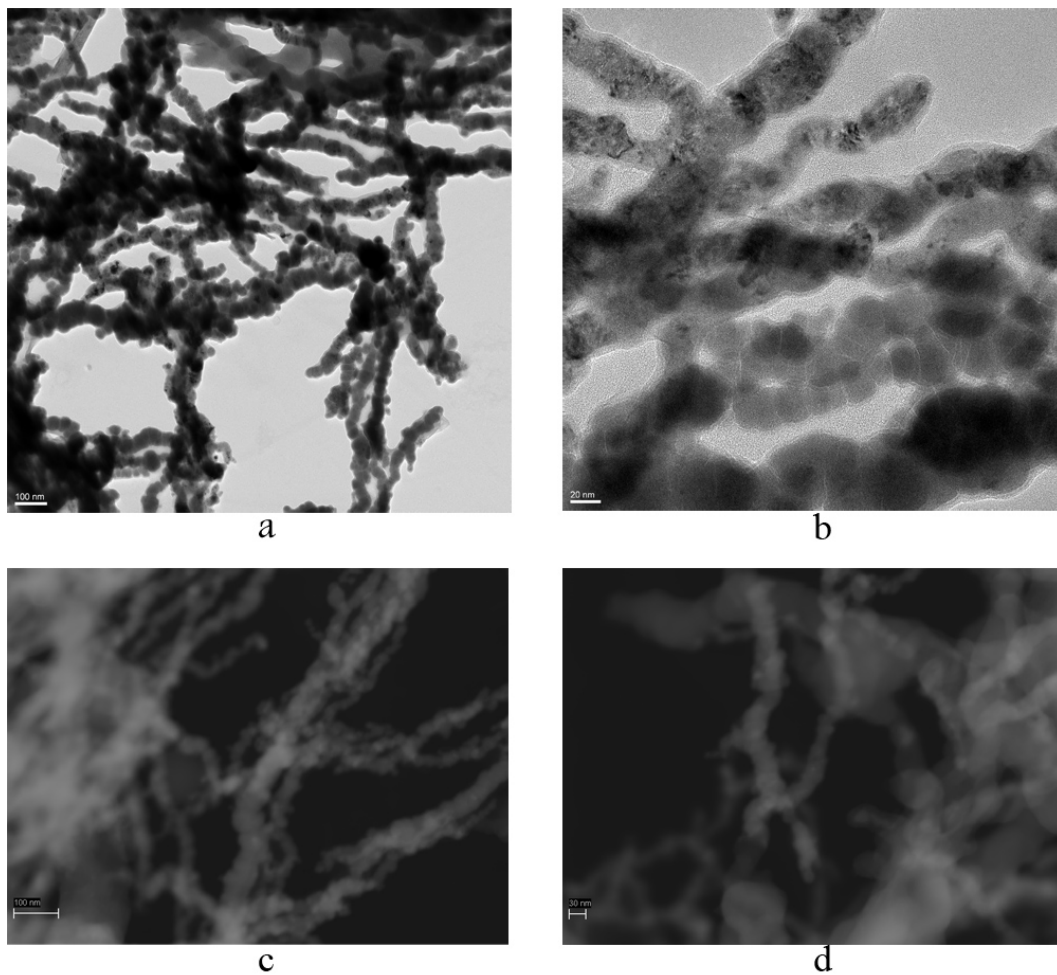
**Figure 3.13 nZVI TEM images (a and b) and STEM images (c and d)**

The nZVI core-shell structure was more obvious in the High Resolution TEM (HR-TEM) image shown in Figure 3.14. The inner zones consist of dark areas that stand for iron with a clear light shell around it. In the case of small particles the oxidation degree seemed to be higher thus showing smaller dark zones and larger oxidized iron shells.
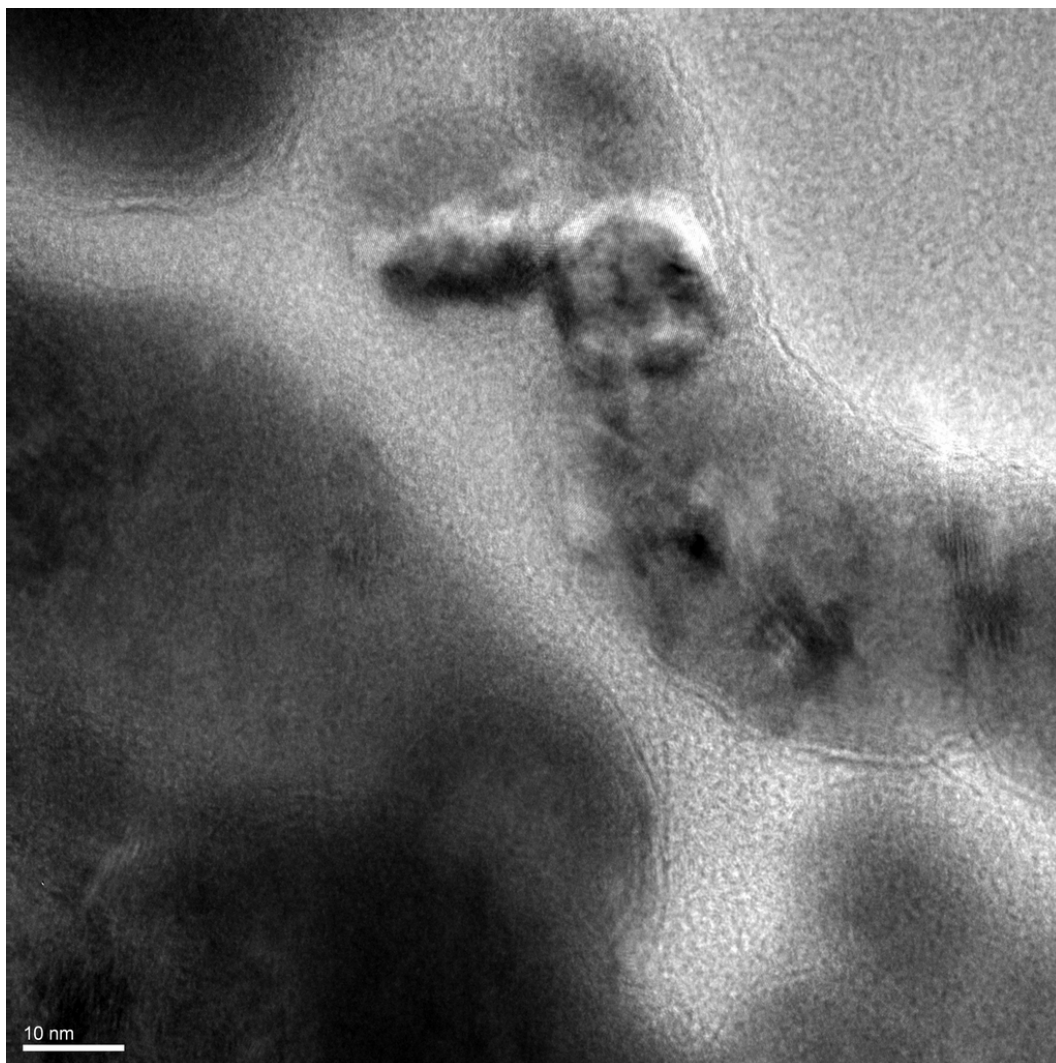
**Figure 3.14 HR-TEM of nZVI showing the core-shell structure**

The Fe distribution in nZVI structure was elucidated using STEM EDX mapping mode. Figure 3.15 shows that Fe constitutes the inner zones of the nZVI chains.

BET and Langmuir surface areas were determined as 10.99 m$^2$ g$^{-1}$ and 76.72 m$^2$ g$^{-1}$, respectively, for the prepared nZVI. This surface area is more than 10 folds larger than some commercially available

powder ZVI that has specific area of around 0.9 m$^2$ g$^{-1}$, [35] hence accounting for the higher reactivity of nZVI. However, the prepared nZVI showed lower surface area than other reported nZVI samples prepared using the same borohydride reduction method, some of the reported examples are 14.5 m$^2$ g$^{-1}$ [71], 33.5 m$^2$ g$^{-1}$ [35] and 36.5 m$^2$ g$^{-1}$, [124] and this could be attributed to partial oxidation and aggregation of nZVI samples since BET characterization was carried abroad for prolonged stored samples and not freshly prepared ones.
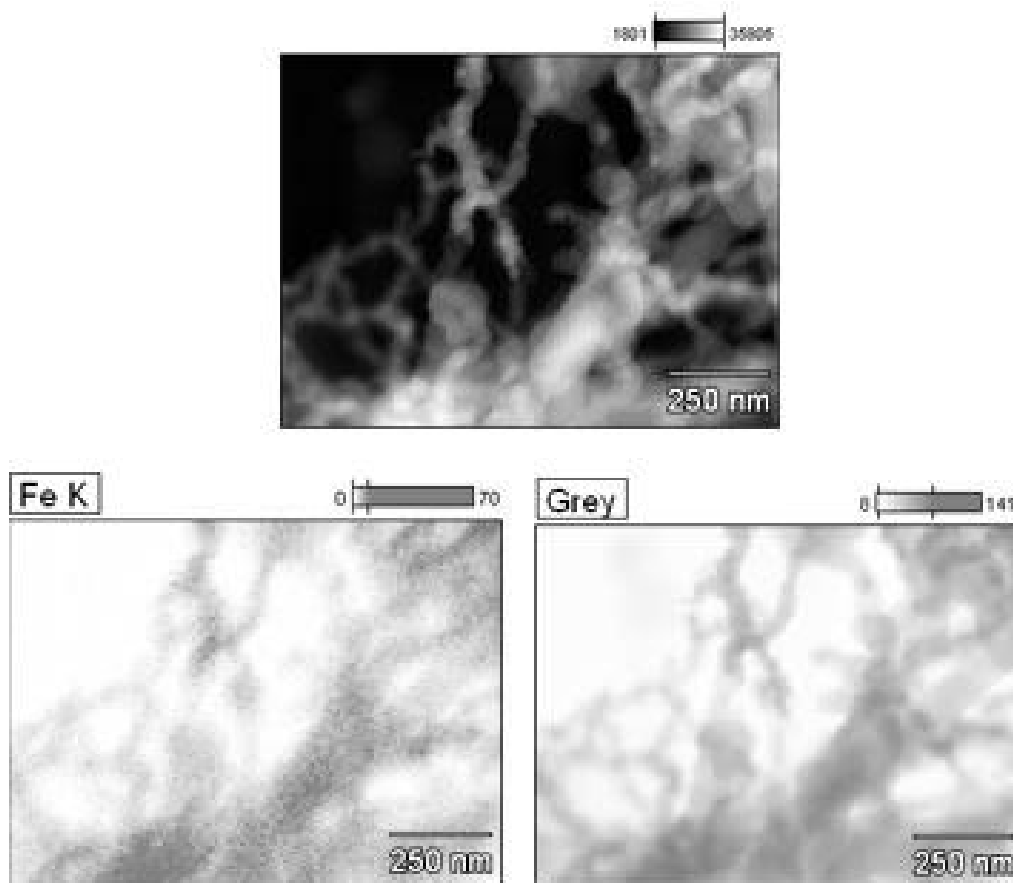


**Figure 3.15 nZVI STEM image and Fe EDX mapping**

Lastly, the surface elemental composition and their electronic environment for the outer 10 nm surface of an nZVI sample was revealed using XPS. Figure 3.16 shows a full scan survey of an nZVI sample, the surface elemental composition do agree with the previous discussed EDX results (Figure 3.10). Auger electron peaks for Na and O appear in the full scan along with their photoelectron peaks. Enhanced scan over the Fe 2p photoelectron peaks shown in the inset of Figure 3.16 reveals the features appearing at 725.2 eV, 719.4 eV and 710.8 eV which correspond to the binding energies of Fe 2p1/2, shake-up satellite 2p3/2 and 2p3/2, respectively. The peaks suggest that iron shell is composed mainly from iron oxides and iron oxyhyroxides. [92] Moreover, the two shoulders in the 2p3/2 photoelectron peak confirm the iron oxides and oxyhyroxides composition of the shell. The feature of the small shoulder at 706.8 eV confirms the presence of $Fe^0$ within the outer surface of these nanoparticles. [71] The O 1s photoelectron peak which is shown in the inset of Figure 3.16 appear to have shoulders at 531.1 eV, 531.9 eV and 532.7 eV in addition to the 531.4 eV peak, the broadening in the peak suggest the presence of O in different states, [125] mainly in two regions, lower energy component that can be assigned to surface $O^{2-}$

possessed in the oxide and higher energy component attributed adsorbed oxygen (OH⁻). [126] The 531.4 eV and 531.9 eV can be assigned to structural O in OH⁻, [127] while the 531.1 eV peak can correspond to O in the iron oxide lattice, [125] last shoulder at 532.7 can be attributed to O in physisorbed water. [89]
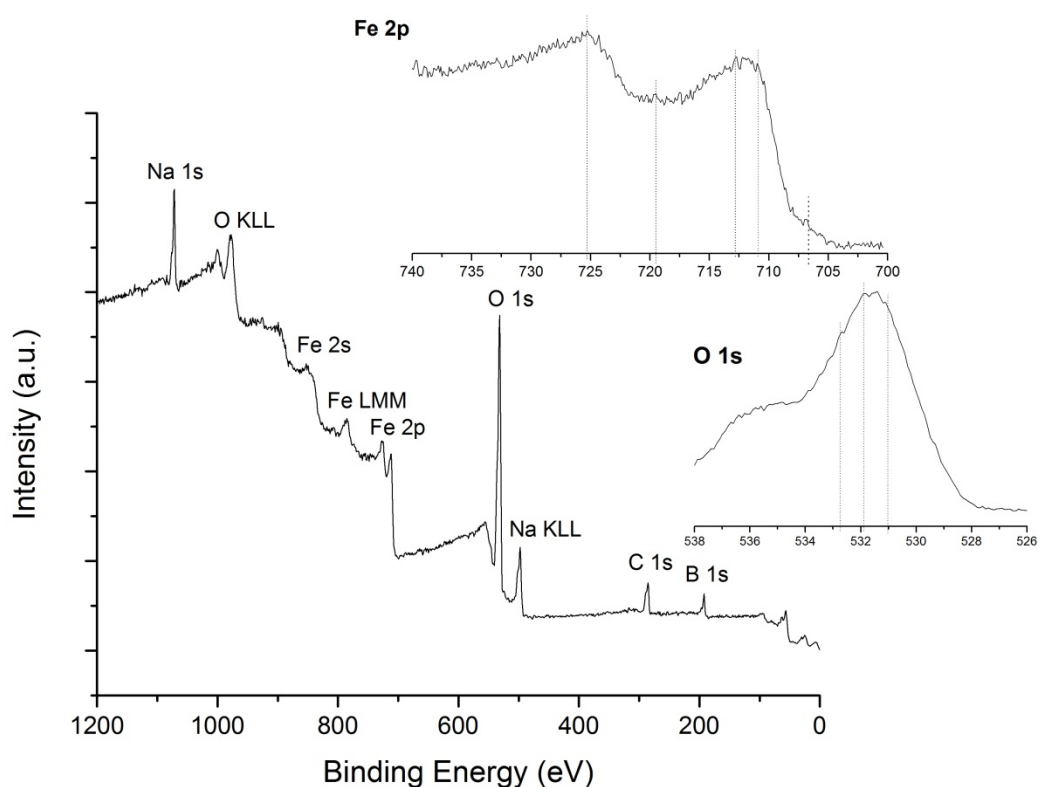


**Figure 3.16 XPS spectrum of nZVI with an inset of Fe2p and O1s peaks**

### 3.1.3 Alumina Supported Iron Nanoparticles (Al-nZVI)

For the sake of comparing the structure and crystalline properties of Al-nZVI with nZVI, XRD patterns were obtained for

both materials and plotted in Figure 3.17. It can be clearly seen that Feº and its (hydr)oxides peaks are present in Al-nZVI sample as in nZVI, hence indicating the development of iron nanoparticles on the alumina surface with the same crystalline structure as in pure nZVI.
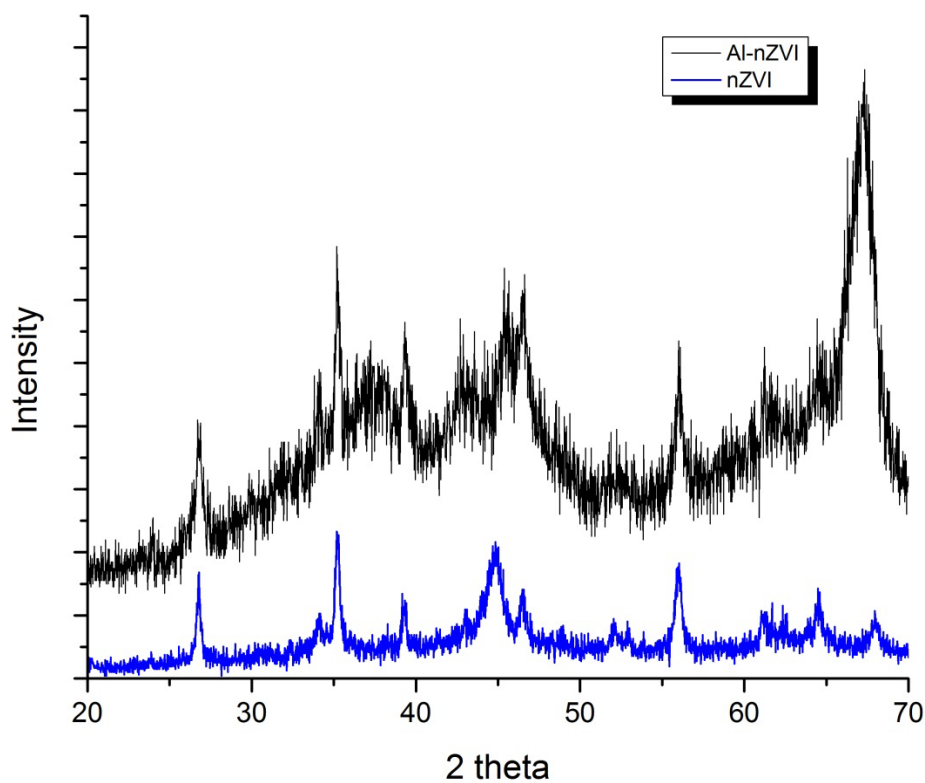


**Figure 3.17 XRD patterns for Al-nZVI and nZVI**

The XRD patterns of Al-nZVI after the removal of MB and MO showed slight differences when compared to Al-nZVI, as seen in Figure 3.18. These differences can be attributed to partial oxidation of $Fe^0$ during the dye removal process and the development of iron oxyhyroxides.
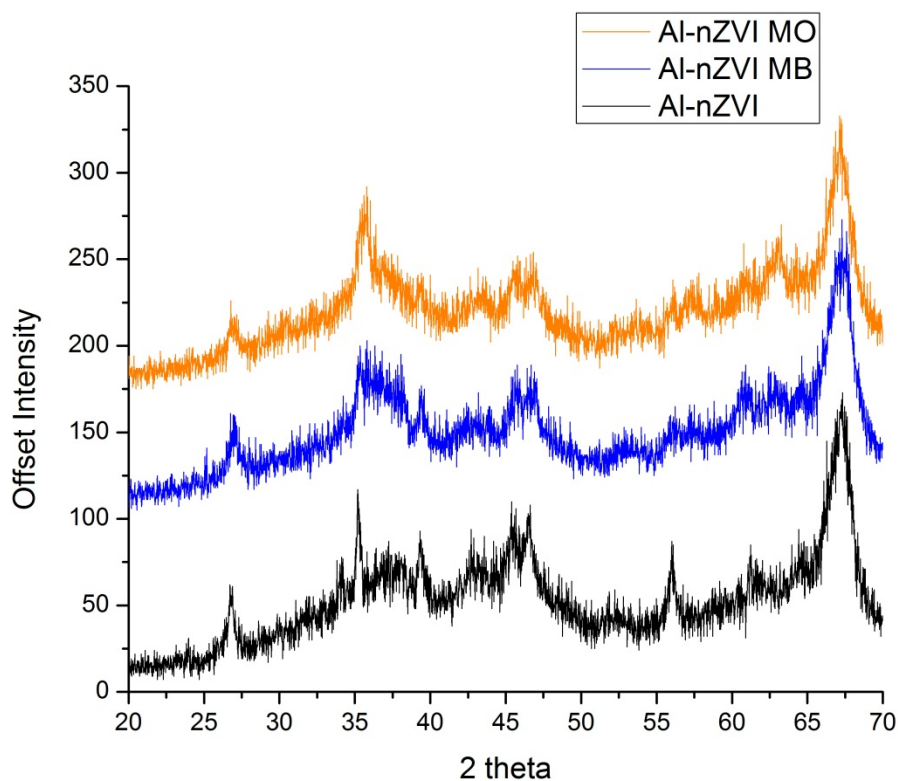
**Figure 3.18 XRD patterns of Al-nZVI, Al-nZVI MB and Al-nZVI MO**

The Al-nZVI SEM images in Figure 3.19 reveals the iron nanoparticles distribution on the alumina surface in a chain like manner resembling those of pure nZVI. However, smaller chains of nZVI can be seen in various areas on the alumina surface indicating successful use of alumina as a solid support to decrease the aggregation of the nanoparticles, and stand as a barrier preventing the agglomeration of these chains to form further larger clusters.
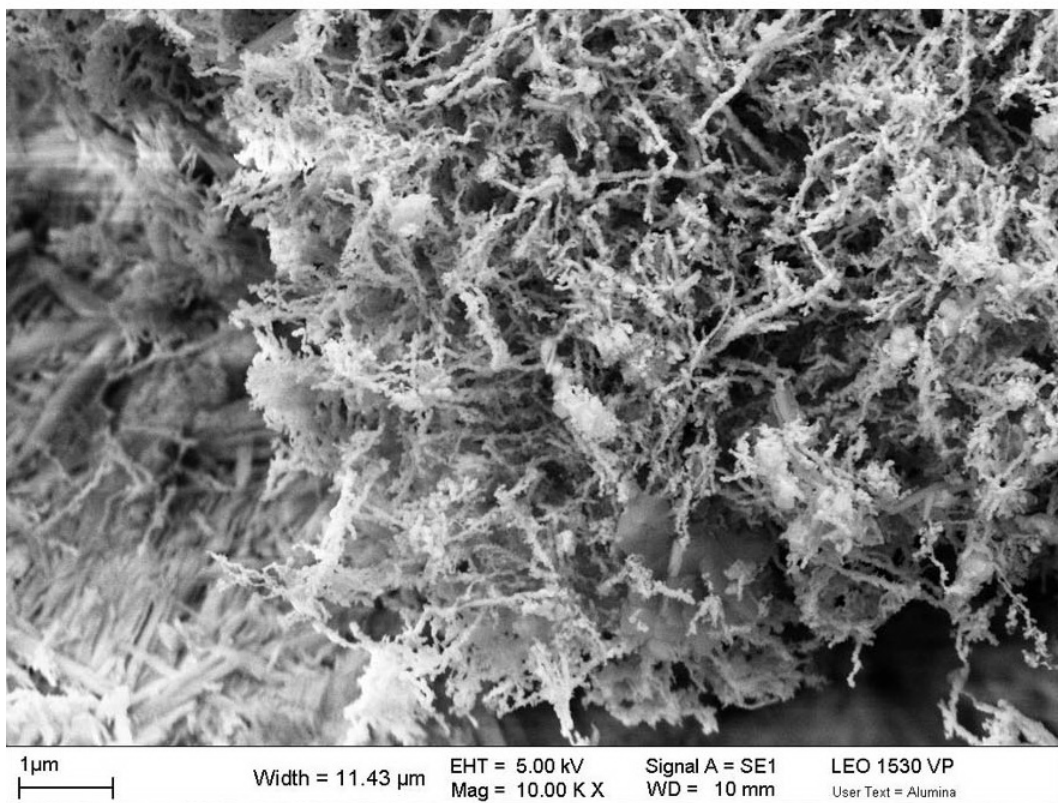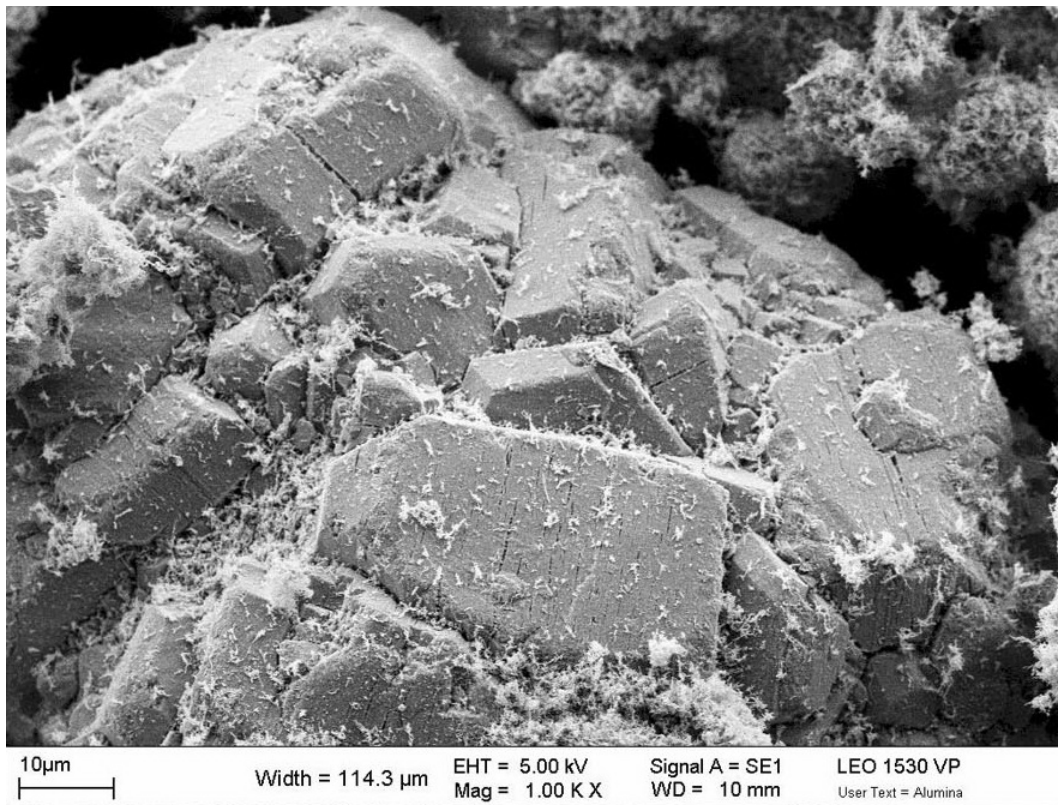
**Figure 3.19 SEM images of Al-nZVI at various magnifications**

Back-scattered SEM images were obtained to validate the presence of iron nanoparticles on the surface of alumina. As can be seen in Figure 3.20 A, nZVI covers most of the alumina surface as revealed by light areas while leaving some dark areas representing light weight elements that can be attributed to alumina. The enhanced zoom SEM image (Figure 3.20 B) and its back-scattered SEM (Figure 3.20 C) show that the dark areas as large particles that lack porosity and chain-like morphology, thus confirming their alumina identity.
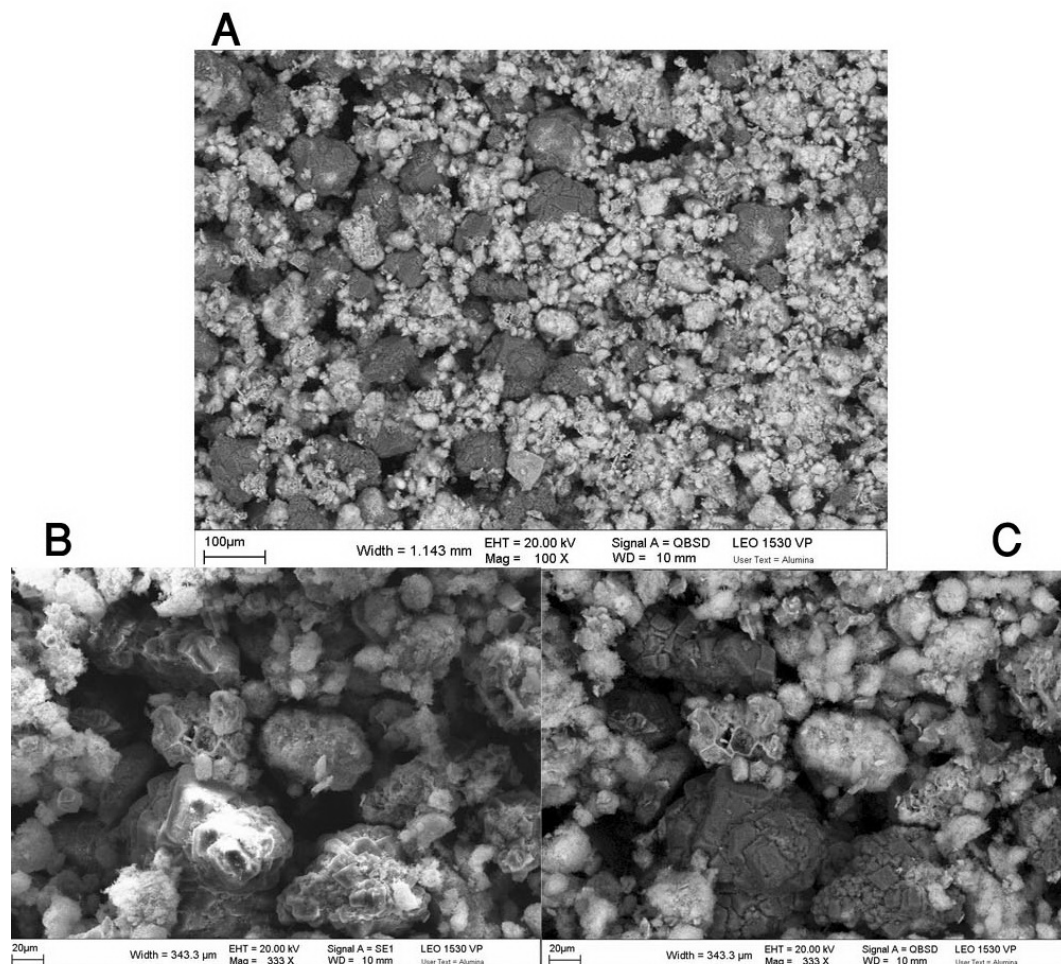


**Figure 3.20 Al-nZVI back-scattered SEM (A & C) and SEM (B)**

The surface elemental composition of Al-nZVI by weight was revealed using EDX analysis in integrated mode to be about 60% Fe, 26% O and 11% Al as seen in the EDX spectrum (Figure 3.21). It's worth noting that the amount of Fe and O in Al-nZVI is very close to their percentages in nZVI. The percentage of O in the nZVI sample comes solely from iron (hydr)oxides while in Al-nZVI it can originate also from iron (hydr)oxides along with structural O signals of alumina surface. Based on this, it can be concluded that a lesser amount of oxidized iron exist in the Al-nZVI composite when compared with nZVI.
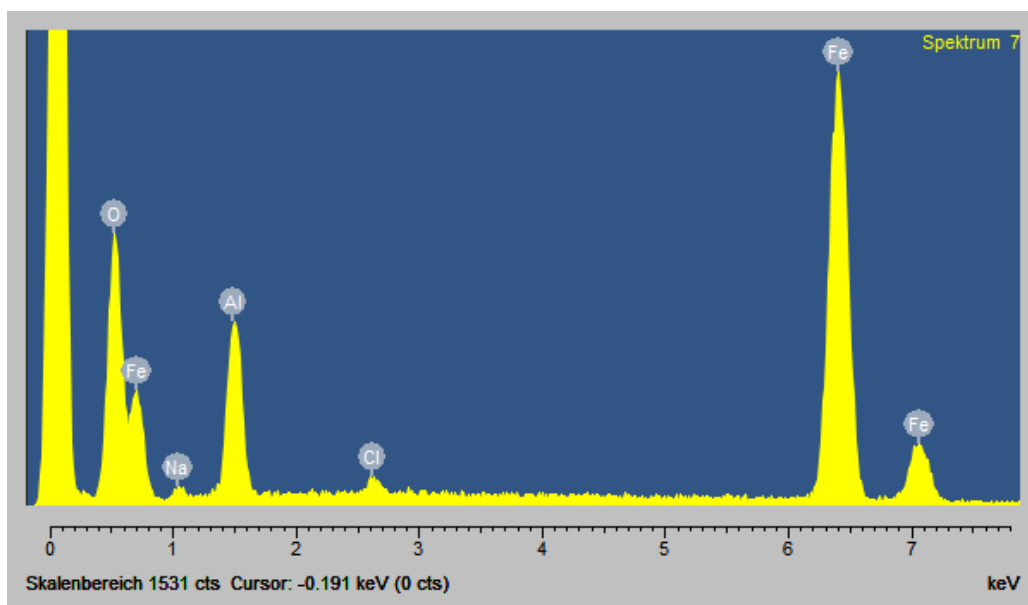


**Figure 3.21 EDX spectrum of Al-nZVI**

TEM and STEM images (Figure 3.22) of Al-nZVI confirmed that the chain-like morphology of iron nanoparticles in the composite resembles that in pure nZVI, with particles sizes being around 50 nm.
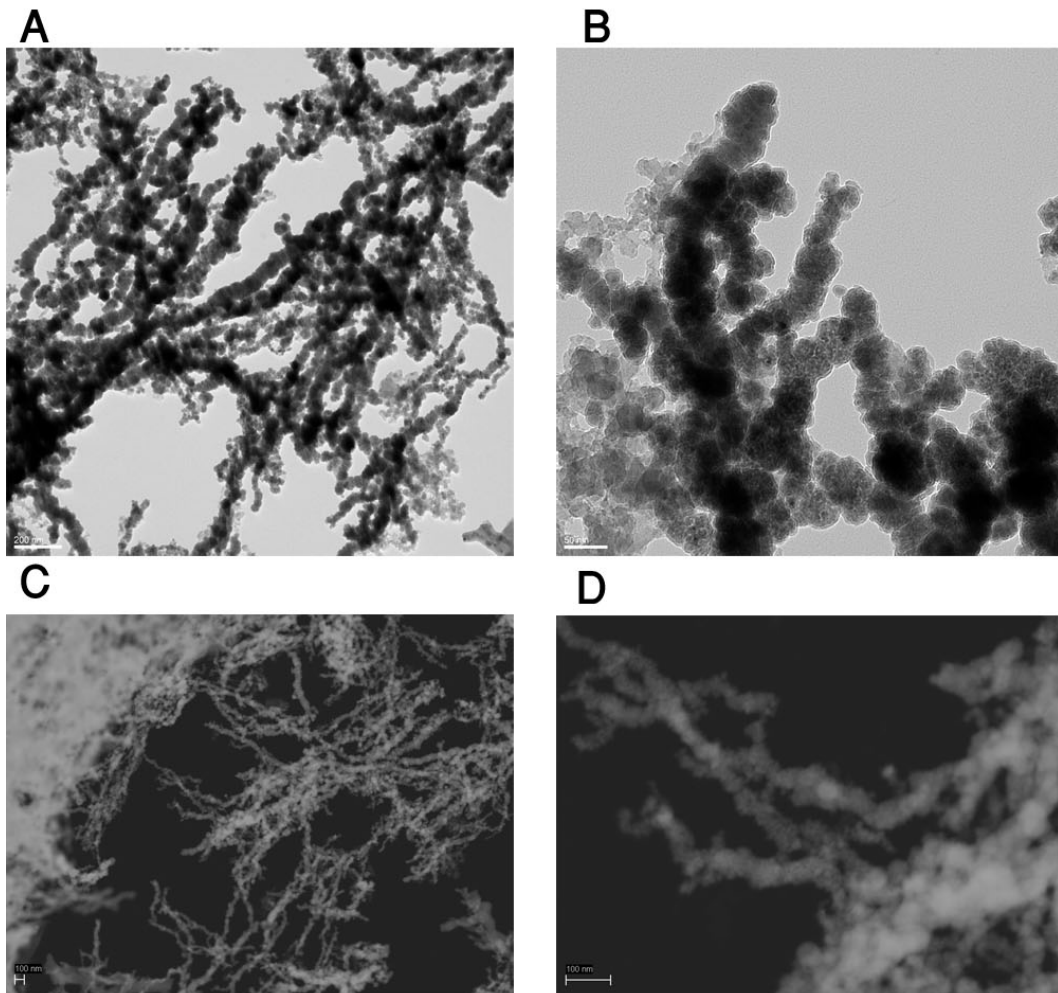


**Figure 3.22 Al-nZVI TEM images (A & B) and STEM images (C & D)**

The chains were found to be composed mainly of iron as seen in EDX iron mappings of the STEM image. Iron appears to be present mainly in the inner zones of the chains, while the outer areas are

thought to consist of oxidized iron, thus confirming the core-shell structure as in nZVI.
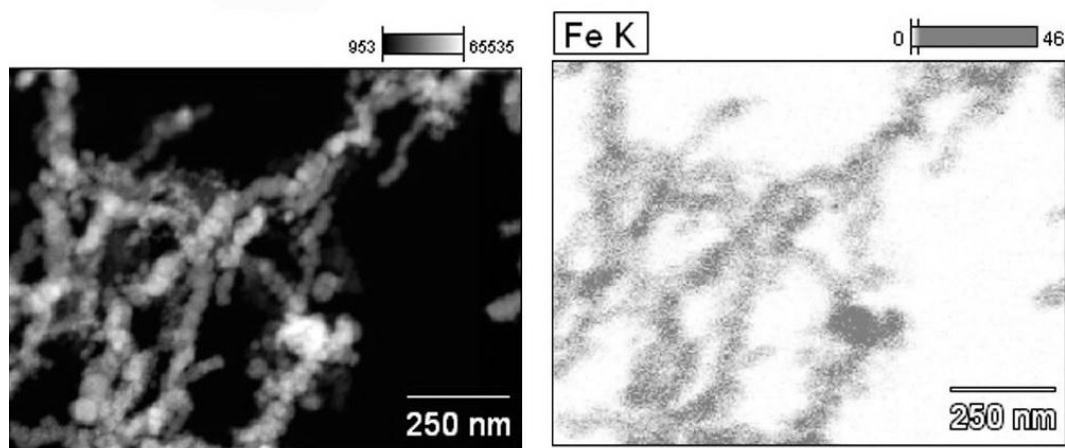


**Figure 3.23 Al-nZVI STEM image and its EDX Fe mapping**

Full scan XPS spectrum (Figure 3.24) reveals the same elemental composition as obtained from EDX (Figure 3.21). The inset in the same figure reveals an enhanced scan of Fe 2p photoelectron peak with features at 706.5 eV, 710.8 eV, 719.4 eV and 724.5 eV that correspond to the binding energies of zero valent Fe ($Fe^0$), Fe 2p3/2, shake-up satellite 2p3/2 and 2p1/2, respectively. [71] The Fe 2p photoelectron peak from Al-nZVI seem to correlate with the Fe 2p from nZVI as can be seen in Figure 3.25, hence indicating same electronic environment for the iron nanoparticles in nZVI and the composite Al-nZVI. Moreover, The Al 2p photoelectron peak appeared at 73.6 eV which is similar to $Al_2O_3$ values. [128]
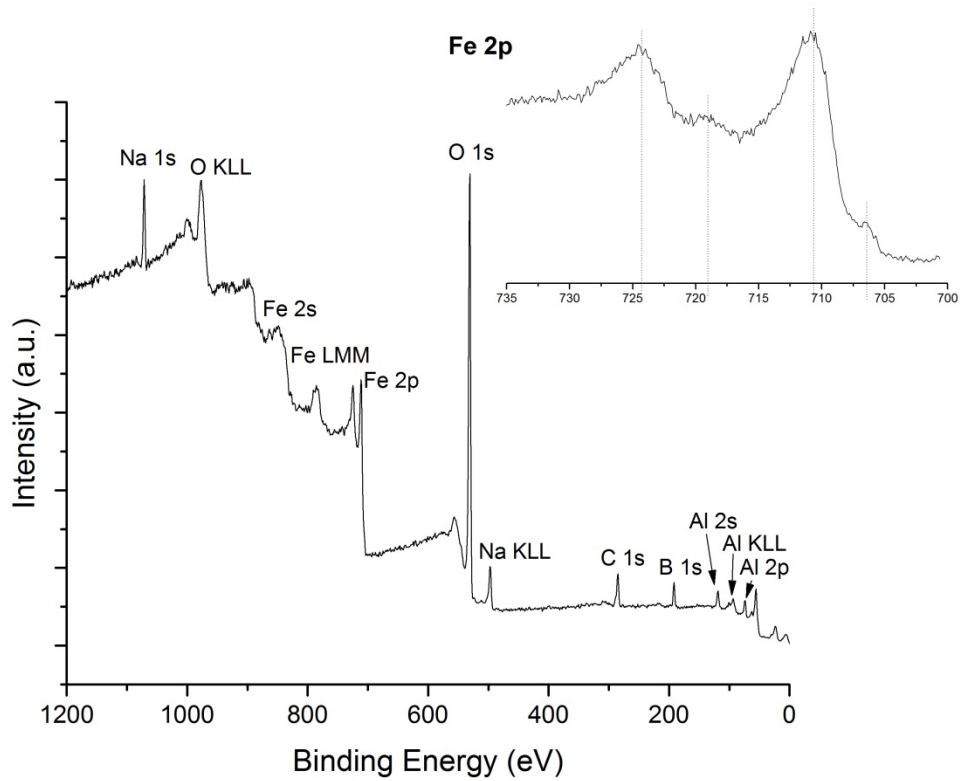
**Figure 3.24 XPS spectrum of Al-nZVI with an inset of Fe2p**
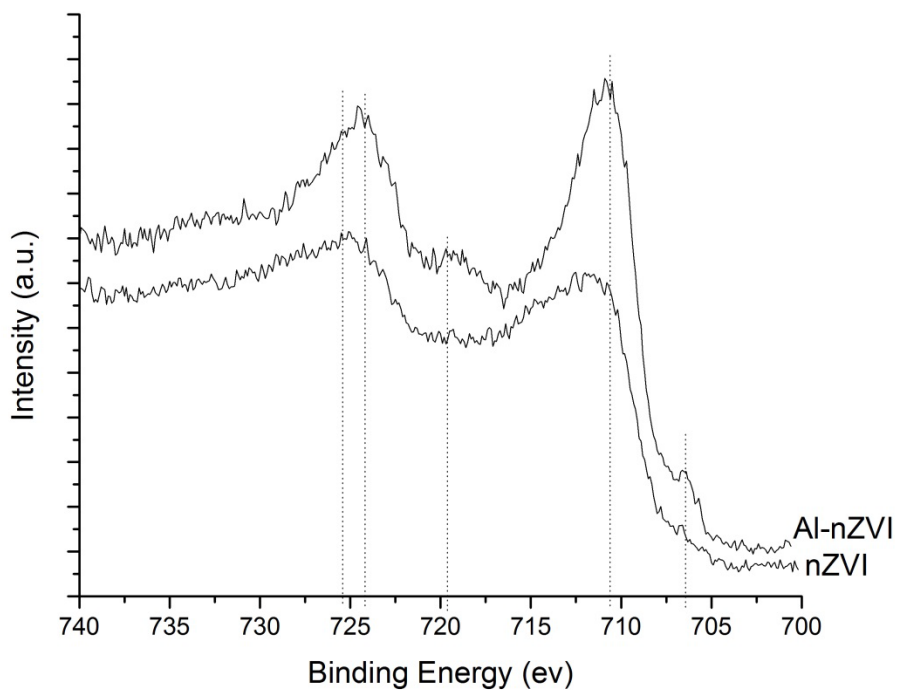


**Figure 3.25 Fe 2p photoelectron peaks of nZVI and Al-nZVI**

The O 1s photoelectron peak appears to be centered at 531.0 eV as shown in Figure 3.26. It's worth noting that structural O 1s photoelectron peak for $Fe_3O_4$ occurs between 529.7-530.1 eV [129,130] while that for $Al_2O_3$ occurs between 530.9-531.6 eV. [131,132] Curve fitting the O 1s photoelectron peak (Figure 3.26) identifies three main components at 530.0 eV, 530.9 eV and 532.1 eV that can be ascribed to structural O in the lattice of $Fe_3O_4$, structural O in $Al_2O_3$ and physisorbed water. [89]
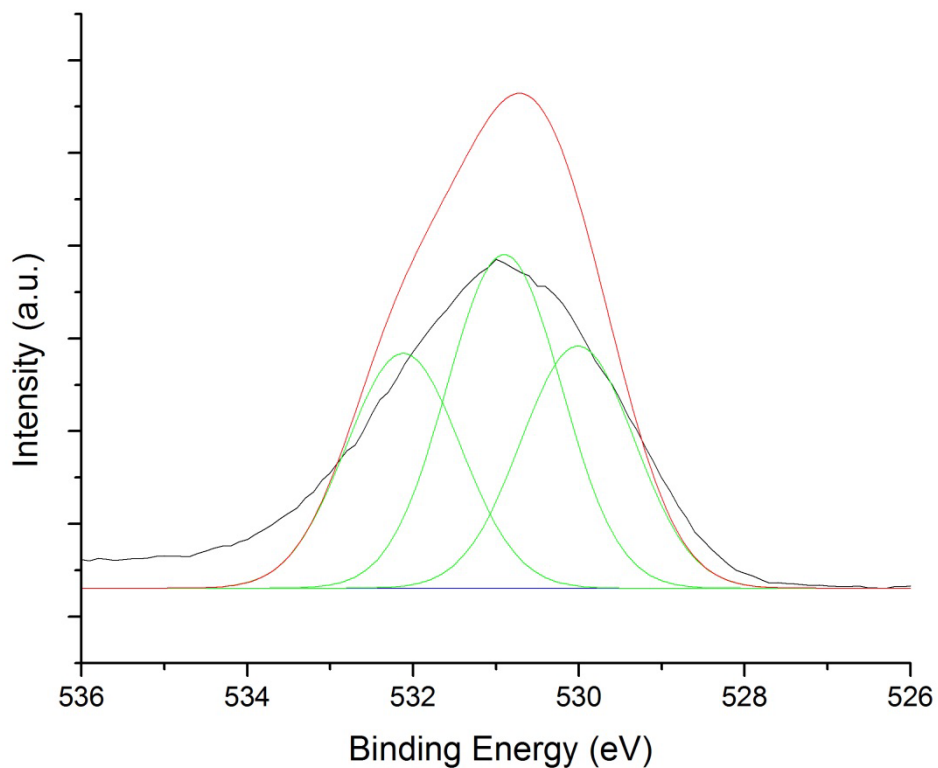


**Figure 3.26 O 1s photoelectron peak with curve fitting**

### 3.1.4  Zeolite Supported Iron Nanoparticles (Ze-nZVI)

Zeolite used in this study as a solid support for nZVI was of a natural source, obtained from Inamarble in Turkey. The chemical structure consists mainly of sodium, potassium, calcium, and aluminasilicate. The mineralogical structure is composed mainly of Clinoptilolite, which is the most widely available natural zeolite. Table 3.1 shows the chemical composition of the zeolite used in this work. [133]

**Table 3.1 Chemical composition of zeolite**

| $SiO_2$ | 68% | $K_2O$ | 2.73% | $TiO_2$ | 2.73% |
|---|---|---|---|---|---|
| $Al_2O_3$ | 11.6% | $Fe_2O_3$ | 1.49% | $MnO$ | 0.16% |
| $SiO_2/Al_2O_3$ | 5.8-6% | $MgO$ | 0.63% | | |
| $CaO$ | 0.82% | $Na_2O$ | 3.39% | | |

A comparison between the FTIR spectra of pure zeolite samples and others employed in the removal of MB and MO (here referred to as zeolite MB and zeolite MO, respectively) was carried out to elucidate any change in the spectra after dye removal. Figure 3.27 shows the corresponding spectra in which minor variations are

observed, thus possibly suggesting that the removal of the dyes did not take place through adsorption on the surface, but rather through molecular degradation.
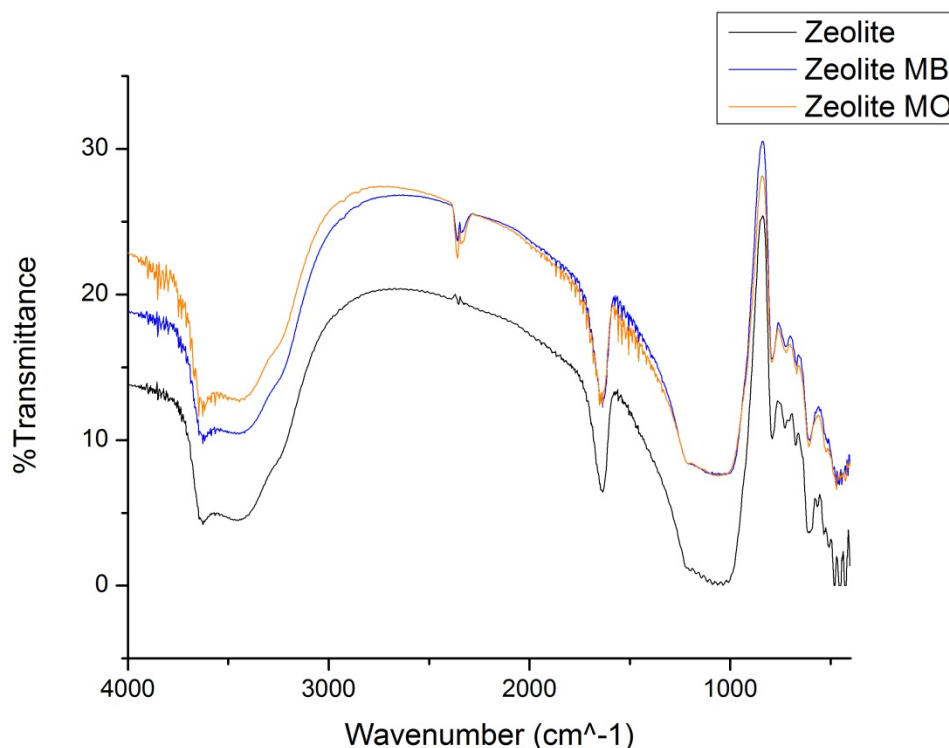


**Figure 3.27 FTIR spectra of zeolite, zeolite MB and zeolite MO**

FTIR spectra of the composite Ze-nZVI before and after its usage in the removal of MB and MO are shown in Figure 3.28. There was no clear appearance of new peaks on the Ze-nZVI MB and Ze-nZVI MO spectra as was the case with nZVI previously (Figure 3.7). The reason of this could be the desorption of dyes or their degradation products from the composite Ze-nZVI while still in the aqueous

solution, or that the dye removal process could be a direct dye degradation with prolonged adsorption involved. Still, further studies should be carried out to confirm so.
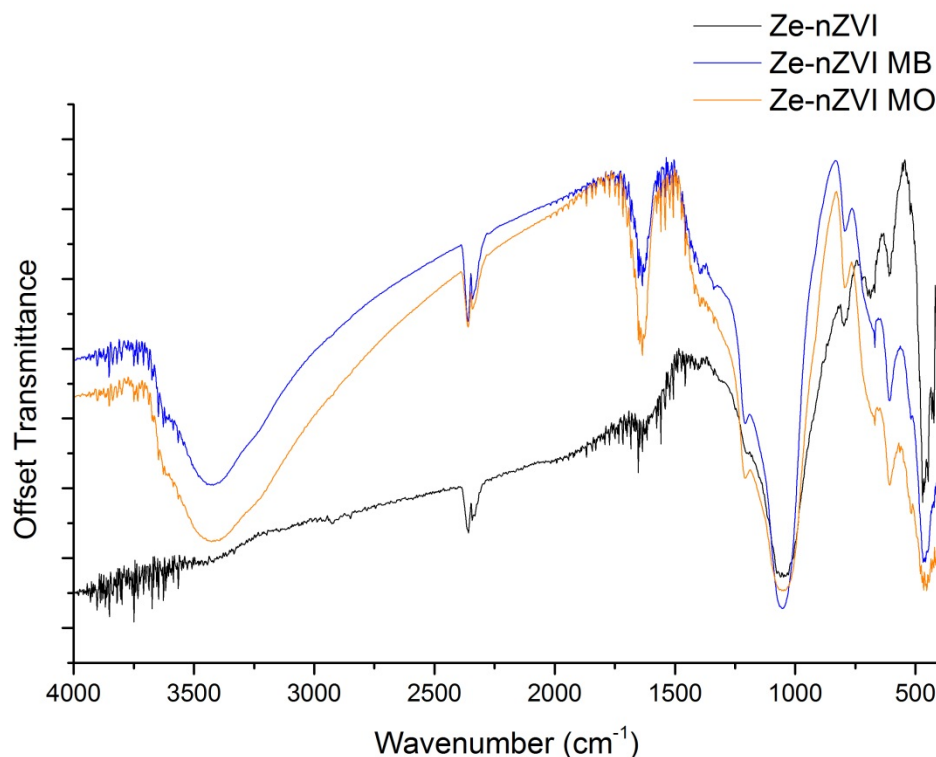


**Figure 3.28 FTIR spectra of Ze-nZVI, Ze-nZVI MB and Ze-nZVI MO**

The crystal structures of zeolite and Ze-nZVI were studied and compared by XRD to provide insights about the presence of crystalline zero valent iron along with iron oxides ($Fe_3O_4$) [122] and iron oxyhydroxide (FeOOH) [123] along the lattice of zeolite crystals. Figure 3.29 shows XRD diagram for zeolite and Ze-nZVI, the $Fe_3O_4$ features at 2θ 35.5 and 43 correspond to hkl values of 311 and 400, same as

those found in nZVI previously, however, the $Fe^0$ feature that is supposed to appear at 2θ 44.8 cannot be distinguished in the XRD diagram.
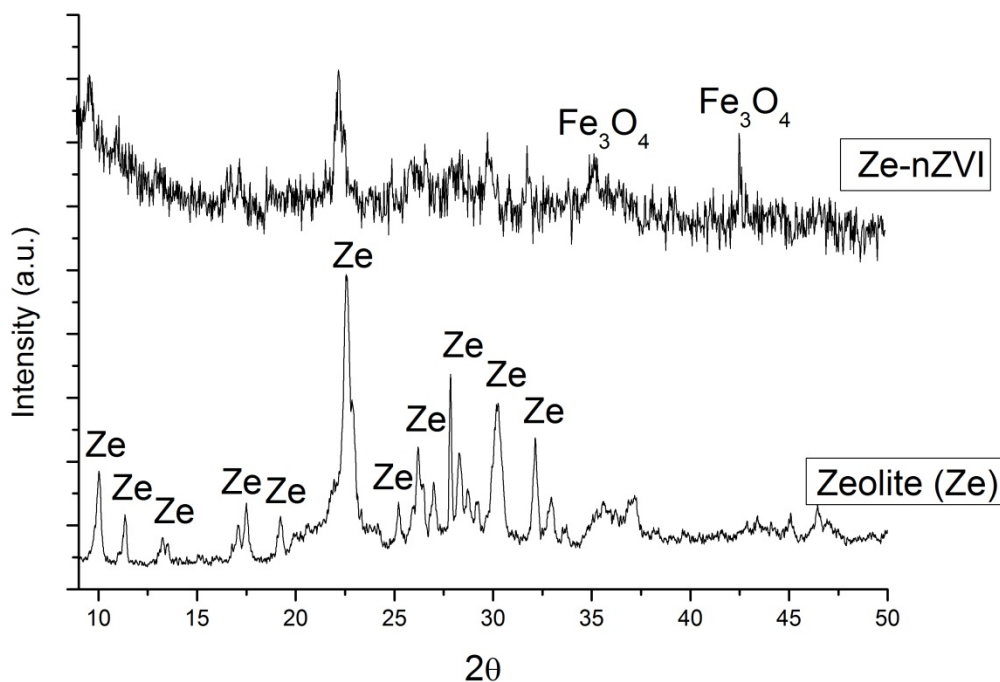


**Figure 3.29 XRD patterns of zeolite and Ze-nZVI**

SEM images of zeolite (Figure 3.30) show its tabular and coffin like morphologies typical for clinoptilolite. The edge sizes appear to range from 1 to 5 µm. The presence of some irregular globular shaped species along with the zeolite crystals can also be seen in the SEM images indicating the presence of some mineralogical impurities.
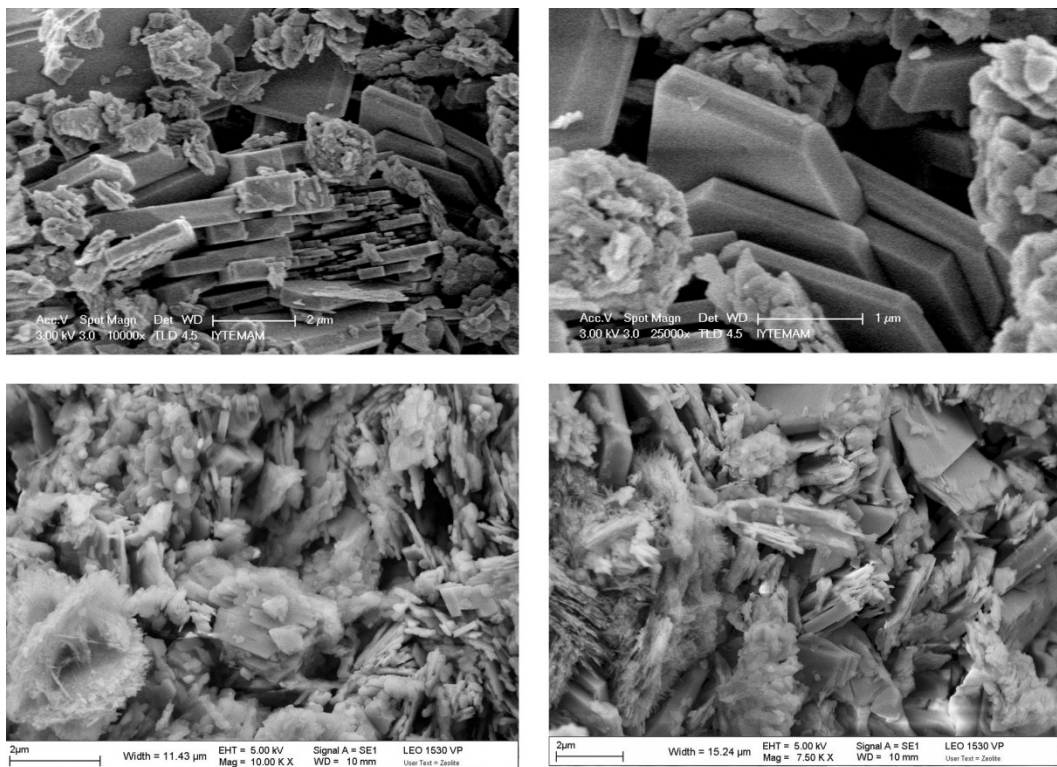
**Figure 3.30 SEM images of zeolite at various magnifications**

SEM images of the composite Ze-nZVI in Figure 3.31 show how nZVI morphology resembles that of pure nZVI (Figure 3.9) in its characteristic chain-like shape. Some of iron nanoparticles appear to grow in between the zeolite crystals while others seem to cover the surface of these crystals. Moreover, in some SEM images, part of the zeolite surface seem to be uncovered with any nZVI chains and this was further confirmed using back-scattered SEM images (Figure 3.32) by the presence of dark areas that stand for zeolite crystals and light ones that correspond to nZVI.
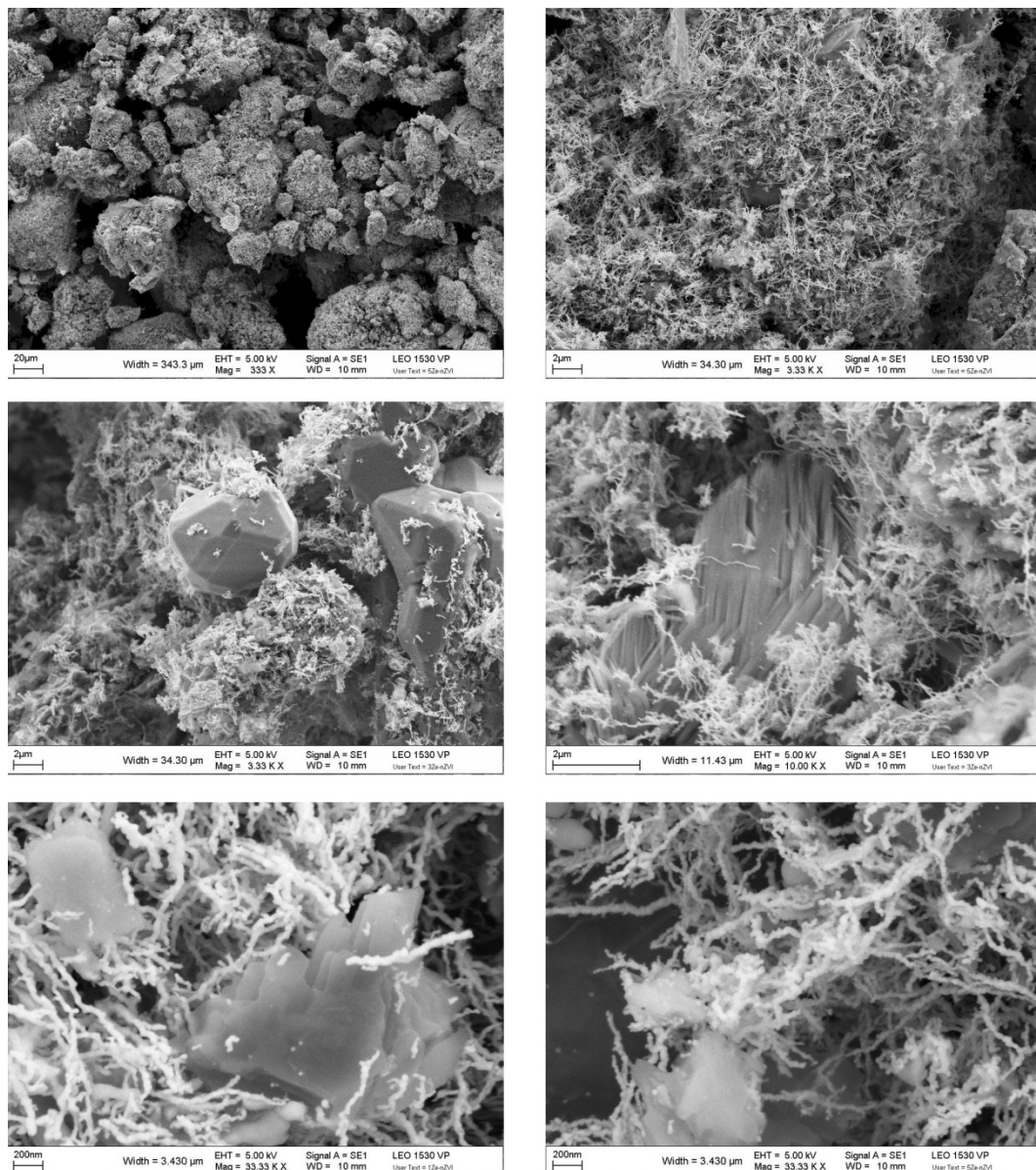
**Figure 3.31 SEM images of Ze-nZVI at various magnifications**

The elemental surface composition of zeolite by weight was revealed to contain 57.06% O, 0.39% Na, 0.51% Mg, 5.66% Al, 31.04 Si, 2.75% K, 1.43% Ca and 1.17% Fe as shown in the EDX spectrum in Figure 3.33 A. The obtained surface composition does agree with the previous mineral composition of zeolite in Table 3.1.
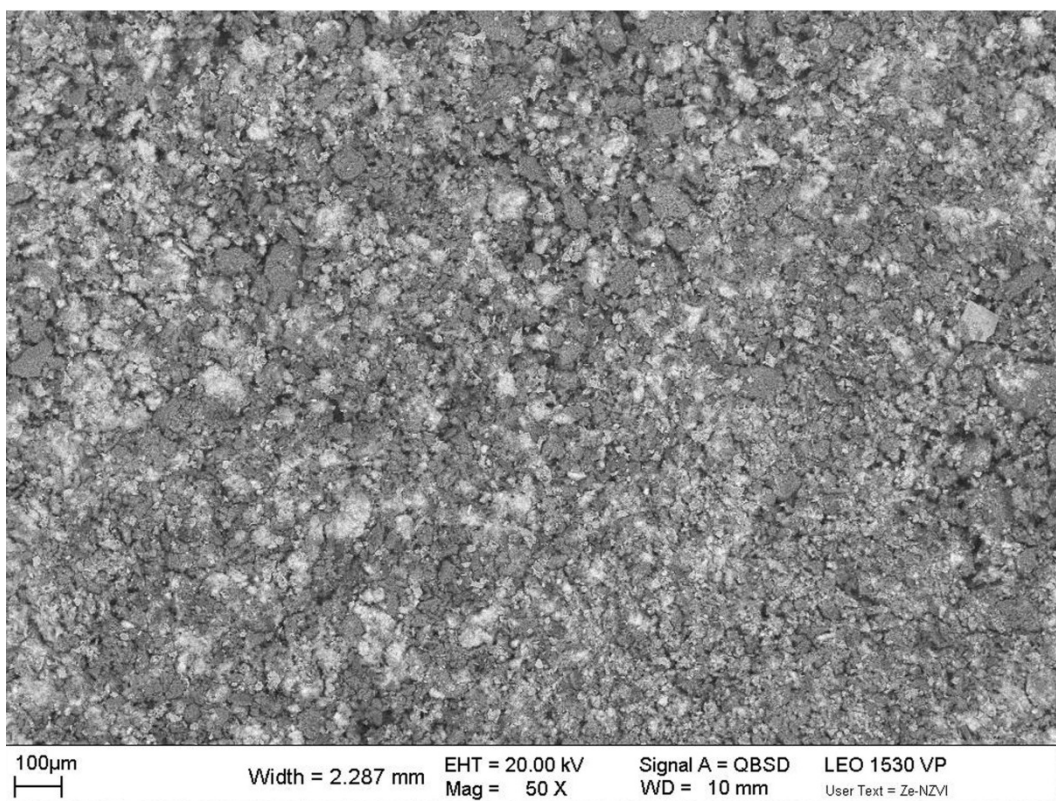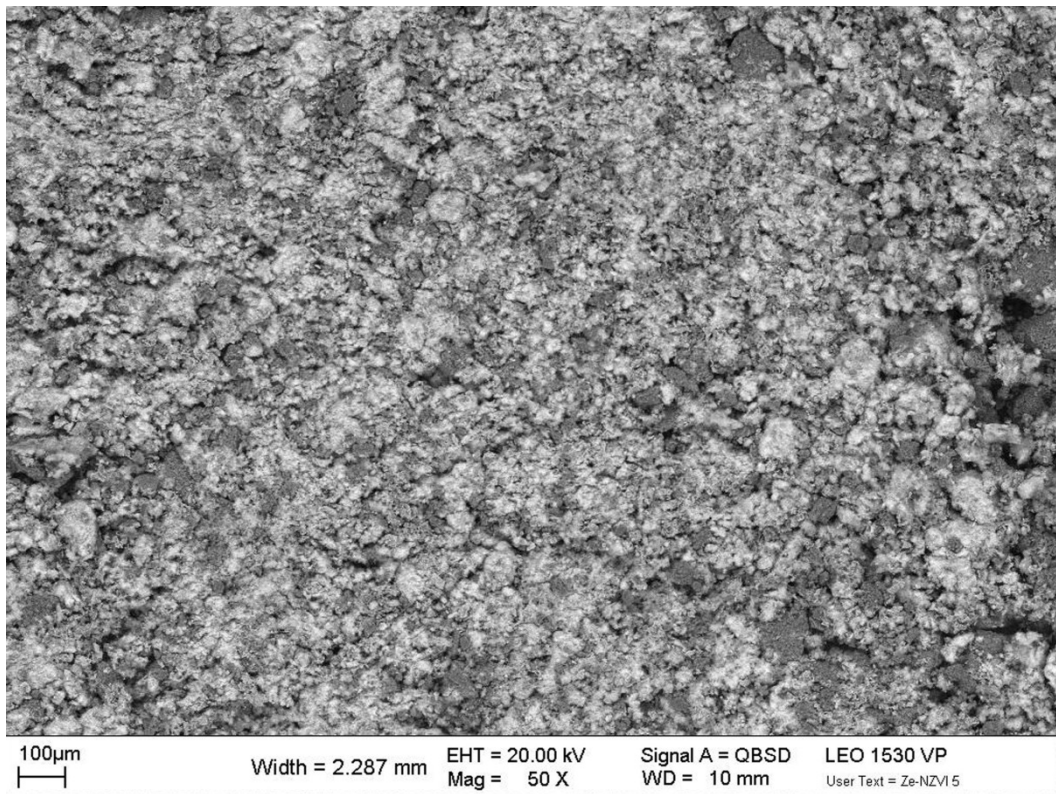
**Figure 3.32 Back-scattered SEM images of Ze-nZVI**
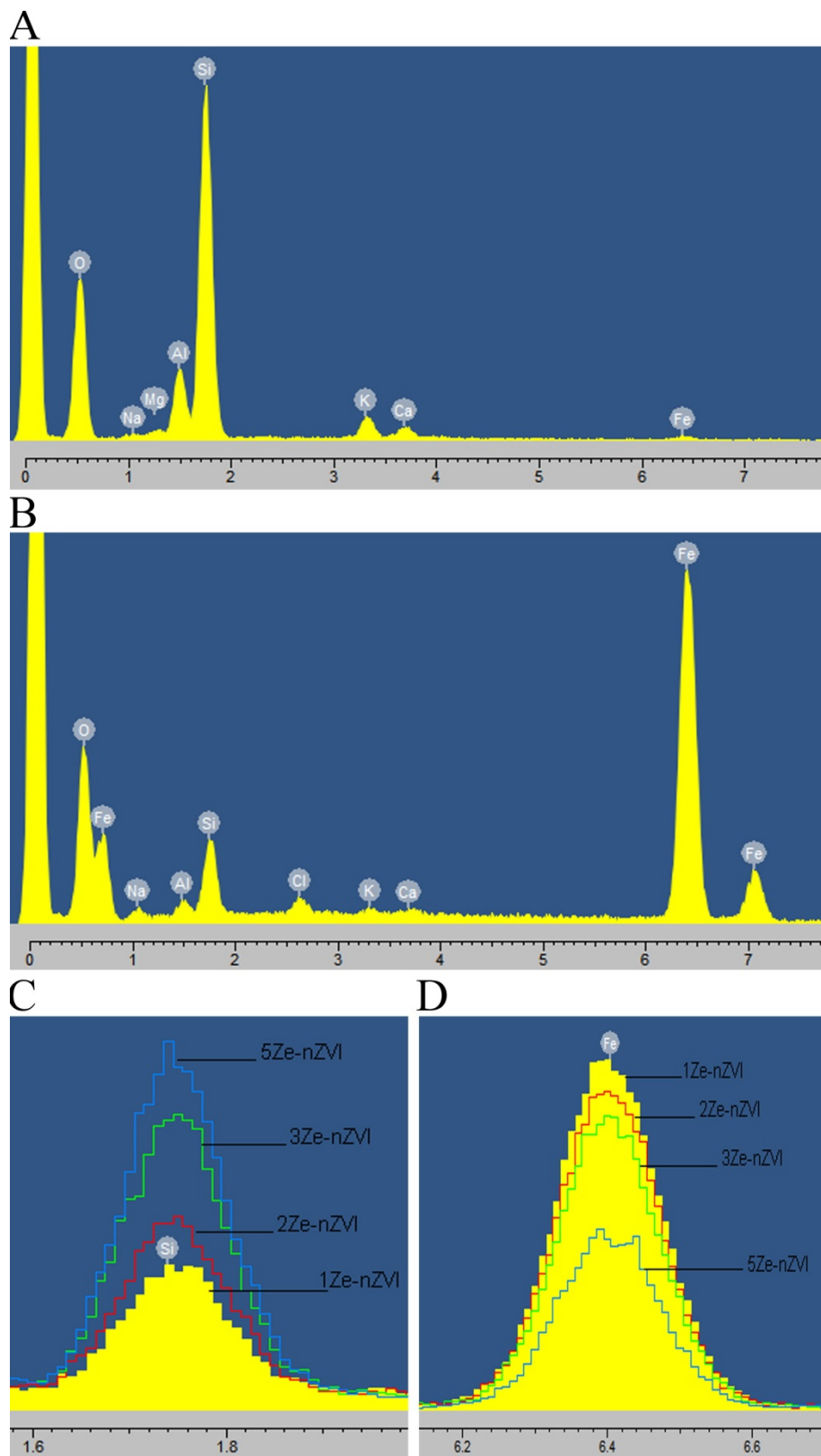
**Figure 3.33 EDX spectra of zeolite (A), Ze-nZVI (B), Si peak in Ze-nZVI (C) Fe peak in Ze-nZVI (D)**

EDX spectrum of Ze-nZVI confirms the presence of Fe reflected by the elevation in Fe content from 1.17% to 63.45% as shown in Figure 3.33 B. Moreover, EDX spectra of Ze-nZVI samples with different iron:zeolite ratios reveal Si content to be 5.22%, 7.27%, 10.31% and 12.70% (Figure 3.33 C) while iron content to be 65.72%, 63.45%, 52.42% and 35.09% (Figure 3.33 D) for the composites 1Ze-nZVI, 2Ze-nZVI, 3Ze-nZVI and 5Ze-nZVI, respectively. This is indicative of increase in the uncovered zeolite surface with decreasing the initial Fe content during the composite preparation.
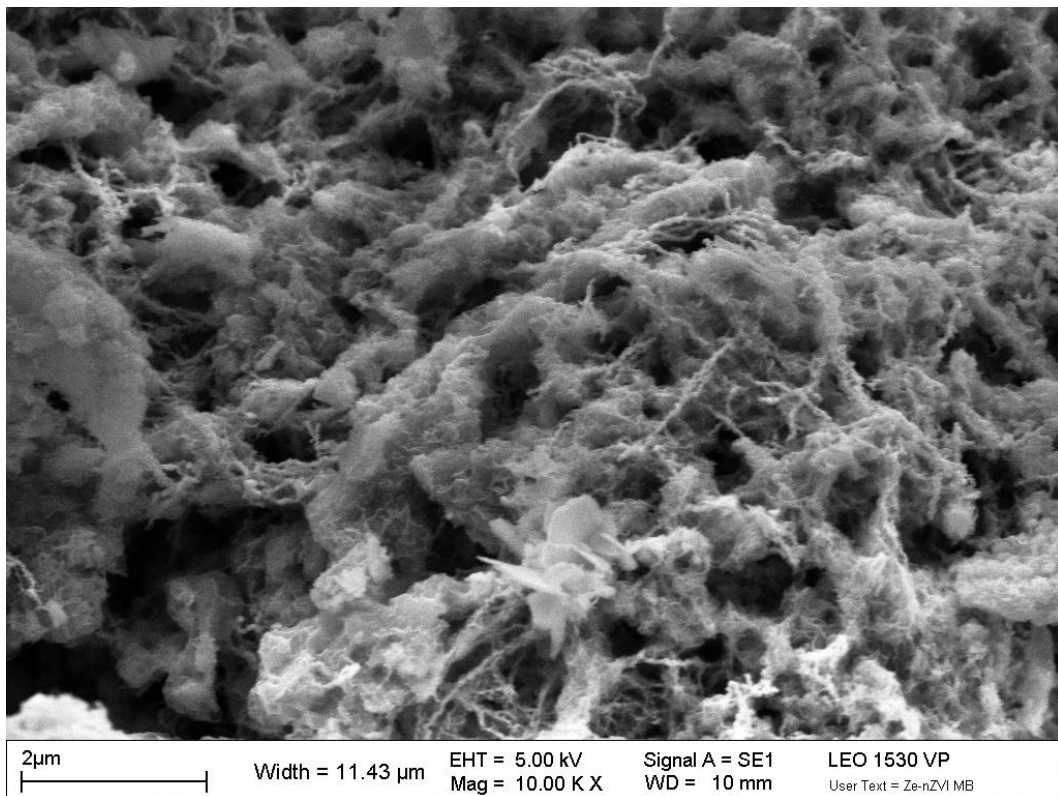


**Figure 3.34 SEM image of Ze-nZVI sample used in the removal of MB**

After employing the 3Ze-nZVI sample in the removal of MB, the Fe content decreased from 63.54% to 41.22%, and the O content increased from 24.74% to 40.03%. Figure 3.34 shows a SEM image of the 3Ze-nZVI and it's clear that a large part of the nZVI has lost its chain like structure and aggregated into random shapes over the zeolite surface.

TEM and STEM images (Figure 3.35) of Ze-nZVI confirmed that the chain-like morphology of iron nanoparticles in the composite resembles that in pure nZVI, with the particle size being around 50 nm. Moreover, the TEM image shows some irregular shaped structures behind the nZVI chains which are believed to be zeolite crystals upon which the nZVI chains were grown.

EDX maps for Fe and O confirms that the chains are composed mainly from Fe as seen in the STEM image along with its EDX maps in Figure 3.36. Iron appears to be present mainly in the inner zones of the chains, while the outer areas are thought to consist of oxidized iron, thus confirming the core-shell structure of these nZVI chains in the composite Ze-nZVI as in pure nZVI.
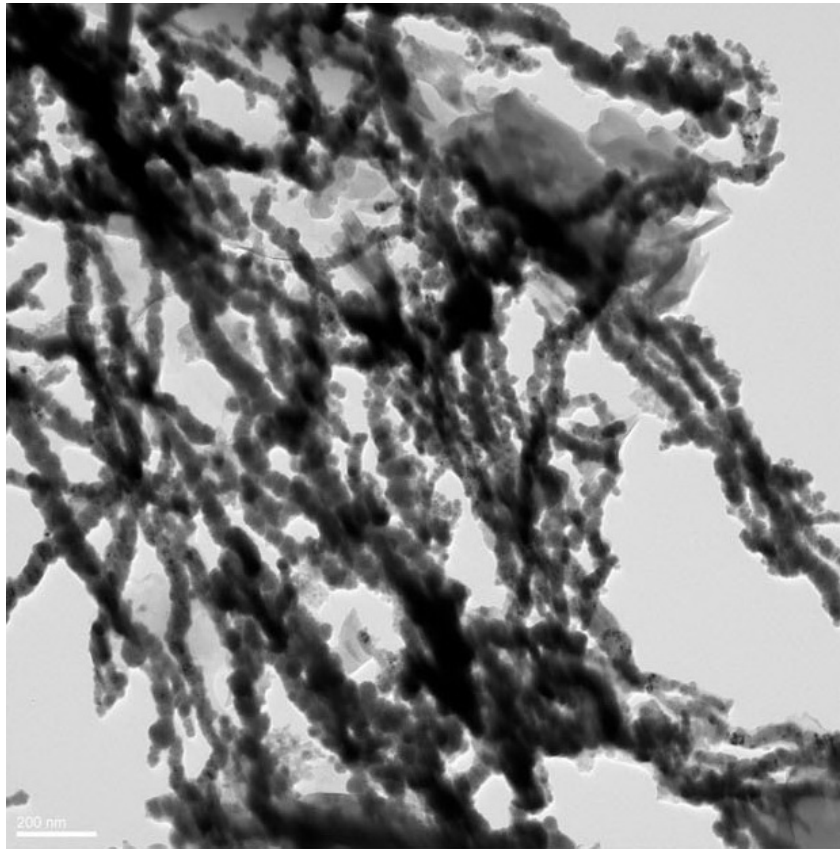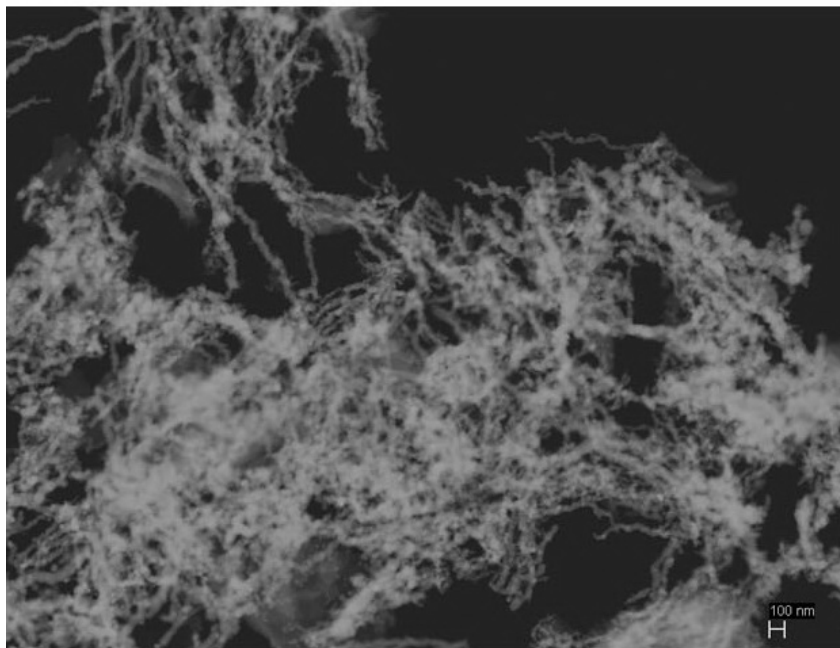
**Figure 3.35 Ze-nZVI TEM image (A) and STEM image (B)**
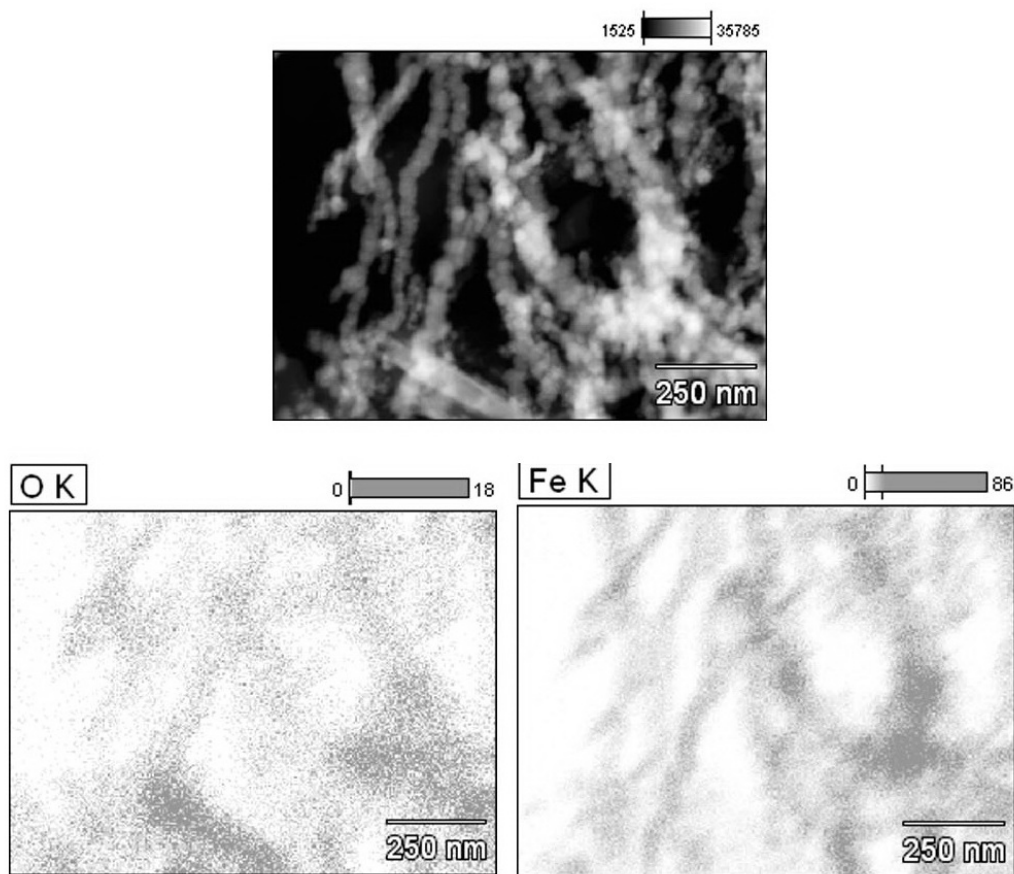
**Figure 3.36 STEM image of Ze-nZVI and elemental mappings for O and Fe**

XPS spectrum of Ze-nZVI (Figure 3.37) displays the same elemental composition as obtained from EDX (Figure 3.33 B). Enhanced scan over Fe 2p photoelectron peak reveals its features at 705.6 eV, 710.5 eV, 719.5 eV and 724.9 eV that correspond to the binding energies of zero valent Fe ($Fe^0$), Fe 2p3/2, shake-up satellite 2p3/2 and 2p1/2, respectively.[71] The Fe 2p photoelectron peak from Ze-nZVI seem to correlate with the Fe 2p from nZVI as can be seen in

Figure 3.38, hence indicating same electronic environment for the iron nanoparticles in nZVI and the composite Ze-nZVI.
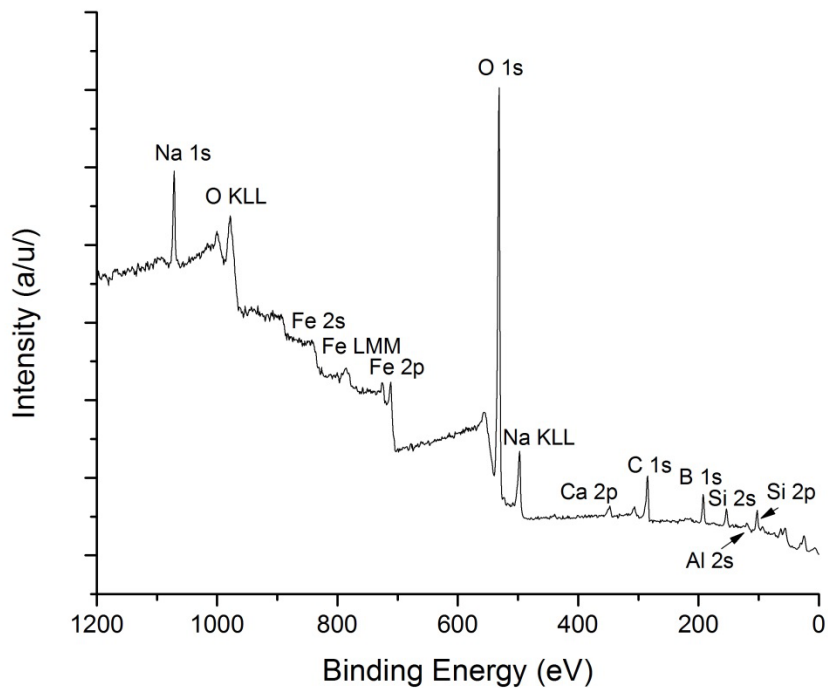


**Figure 3.37 XPS spectrum of Ze-nZVI**
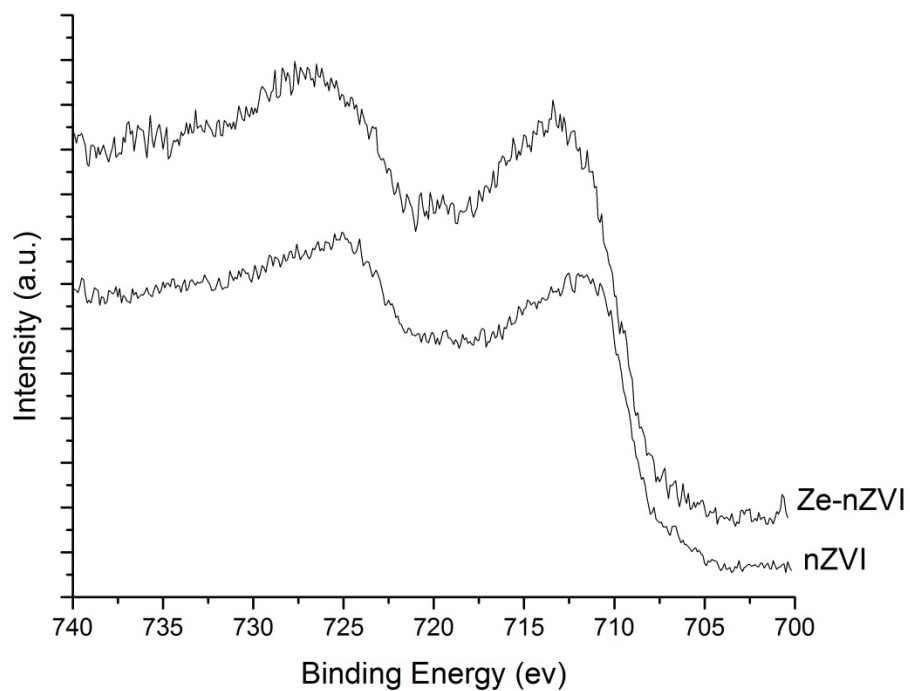


**Figure 3.38 Fe 2p photoelectron peaks of nZVI and Ze-nZVI**

The Si 2p photoelectron peak appears to be centered at 102.5 eV which is lower than the reported value of 103.3 eV for Si 2p in $SiO_2$ of zeolites. [134] However, the Si 2p peak displayed several shoulders that when fitted with Gaussian function (Figure 3.39) and resulted in several deconvoluted peaks at 101.8 eV, 102.5 eV, 103.2 eV, 104.1 eV. Shifts in the Si 2p peak of the composite Ze-nZVI can be attributed to variation in crystalline structure, elemental distribution and chemical treatments of nZVI over the $SiO_2$ surface and hence resulting in different Si electronic environment. [135]
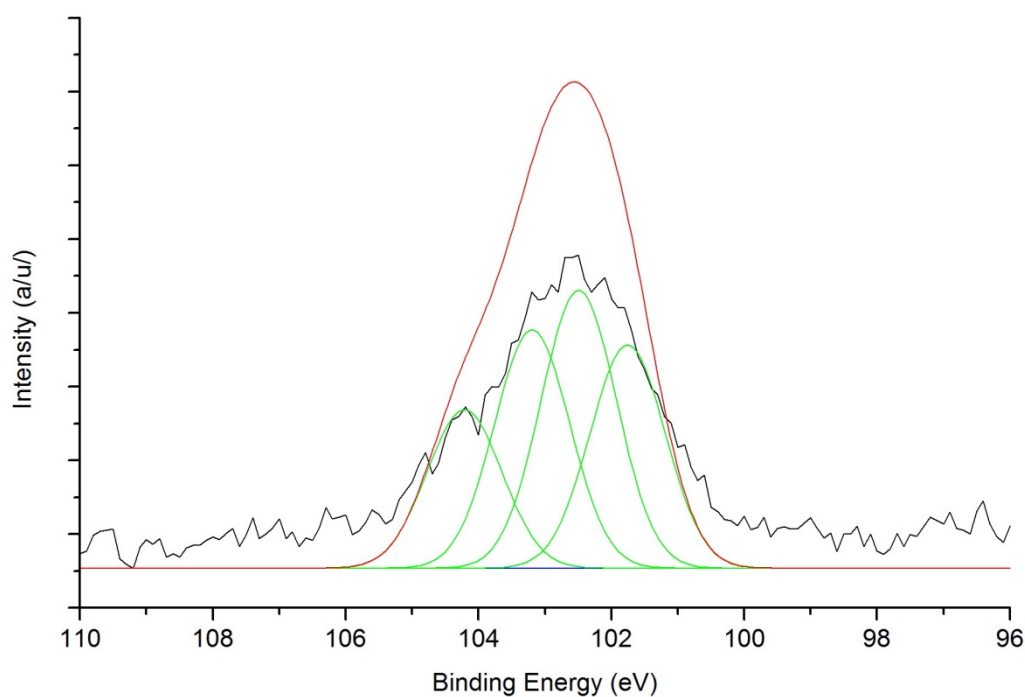


**Figure 3.39 Si 2p photoelectron peak with curve fitting**

Peak fitting of the O 1s photoelectron feature displayed several deconvoluted peaks at 529.7 eV, 530.5 eV, 531.4 eV, 532.4 eV, 533.3 eV and 534.2 eV as shown in Figure 3.40. The variations in binding energies of these deconvoluted peaks can be attributed to the presence of different oxides within the zeolite lattice (see Table 3.1) along the nZVI chains in the composite.
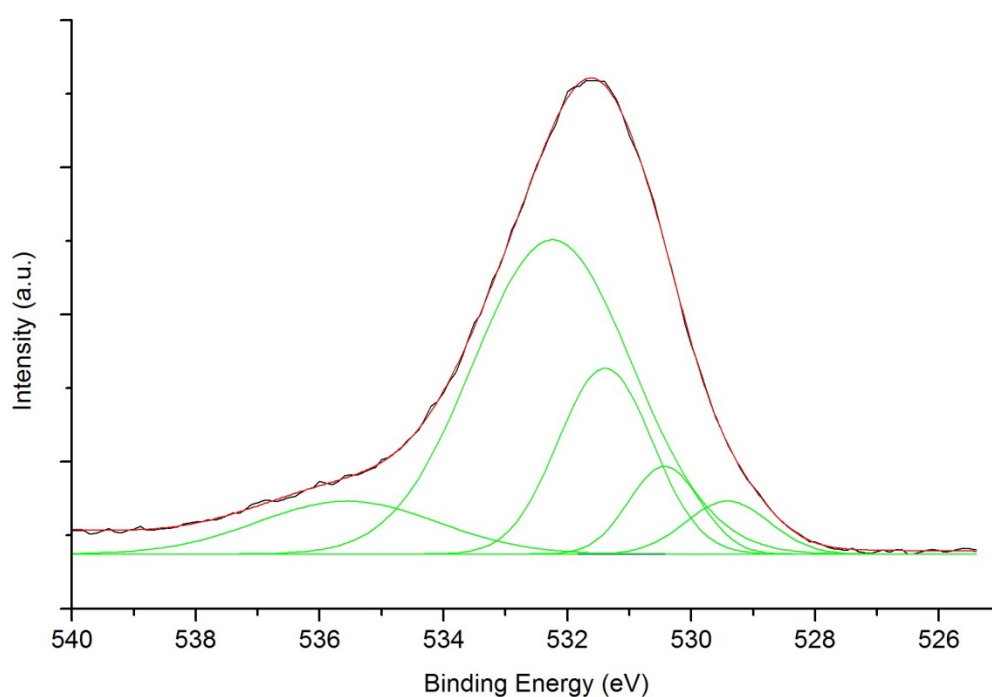


**Figure 3.40 O 1s photoelectron peak with curve fitting**

BET and Langmuir surface areas of zeolite were found to be 8.41 $m^2$ $g^{-1}$ and 57.30 $m^2$ $g^{-1}$, respectively. While those of the composite Ze-nZVI were 21.08 $m^2$ $g^{-1}$ and 160.84 $m^2$ $g^{-1}$, respectively. It's worth noting that the composite Ze-nZVI has much higher specific

surface area than pure nZVI (10.99 m$^2$ g$^{-1}$), and hence it should provide higher surface activity in the dye removal process.

## 3.2 Dye Removal Experiments

The following subsections provide the results and the related discussion related with the removal of MB and MO dyes using nZVI, Al-nZVI and Ze-nZVI materials.

### 3.2.1 Dye Removal Kinetics

Before starting the dye removal experiments, preliminary assessment of the composites Al-nZVI and Ze-nZVI with different support:iron ratios (1Al-nZVI, 2Al-nZVI, 3Al-nZVI and 5Al-nZVI; 1Ze-nZVI, 2Ze-nZVI, 3Ze-nZVI and 5Ze-nZVI) was performed to elucidate their highest dye removal potential. The results are shown in Figure 3.41 for the removal of MB and MO using the two composites with different support:iron ratios that were left in contact with the dye solution for certain periods of time. The result suggests that 3Al-nZVI and 3Ze-nZVI showed the highest dye removal potential. Hence only 3Al-nZVI and 3Ze-nZVI were used in the remaining dye removal experiments and they were named as Al-nZVI and Ze-nZVI.
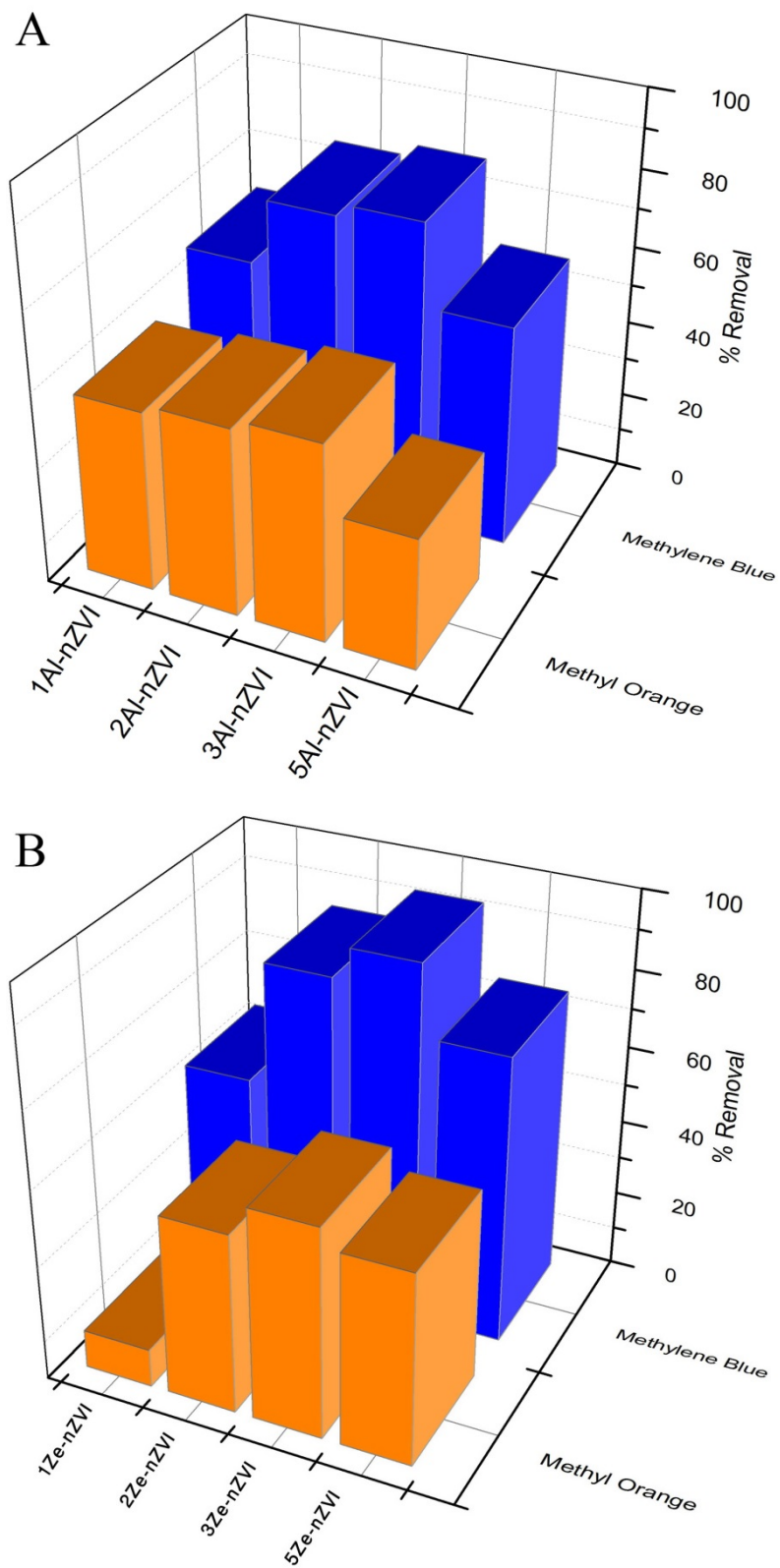
**Figure 3.41 MB and MO removal using different alumina:nZVI (A) and zeolite:nZVI (B) ratios**

The effect of time on the removal of MB using nZVI, alumina, zeolite, Al-nZVI and Ze-nZVI was investigated at initial concentrations of 10.0 mg L$^{-1}$ and 100.0 mg L$^{-1}$, and the results are given in Figure 3.42. The discoloration of MB was found to approach equilibrium after about 7 hours of contact time for the lower concentration and 4 hours for the higher concentration. The earlier attainment of equilibrium at the higher concentration can be attributed to the smaller bulk diffusion resistance, and increased molecular density of the dye at the boundary layer surrounding Fe nanoparticles.
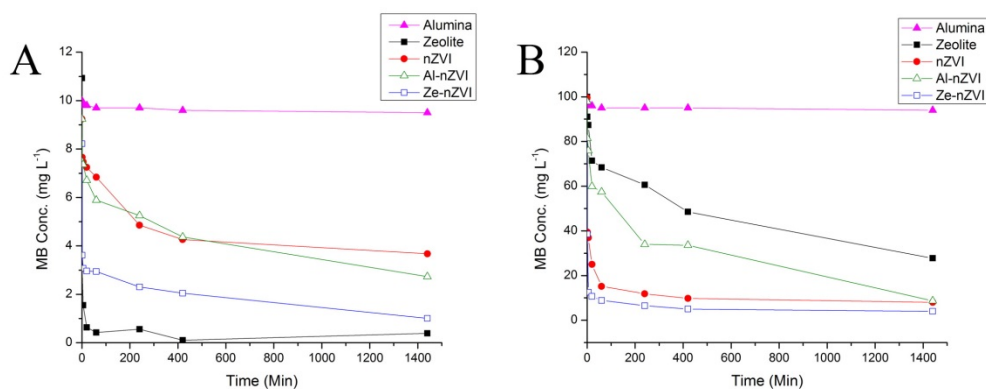


**Figure 3.42 MB removal at initial conc. 10.0 mg L$^{-1}$ (A) and 100.0 mg L$^{-1}$ (B)**

From the same figure it can be stated that alumina showed no obvious MB removal potential at all studied initial concentration, while Al-nZVI showed a relatively comparable MB removal potential with nZVI at low MB concentrations and a lower MB removal potential at higher MB concentrations. Furthermore, at low initial MB

concentration, zeolite showed the highest dye removal capacity, while Ze-nZVI showed better removal efficiency than nZVI. On the other hand, Ze-nZVI showed the highest dye removal potential at high MB concentration while zeolite gave the least dye removal potential.

The data were fitted to pseudo first order and second order kinetics. The corresponding differential rate equations can be formulated as [89]:

$$-\frac{dC_t}{dt} = k_1(C_t - C_e) \qquad \text{(Eq. 1)}$$

$$-\frac{dC_t}{dt} = k_2(C_t - C_e)^2 \qquad \text{(Eq. 2)}$$

Where $C_t$ is the dye concentration at any given time, $C_e$ is the dye concentration at equilibrium. The difference between these two quantities serves as the driving force for fixation on the solid surface. The parameters $k_1$ and $k_2$ stand for the 1st order and 2nd order rate constants, respectively. Integrating both equations under the boundary conditions $C_t=C_0$ at $t=0$ and $C_t=C_t$ at $t=t$ yields:

$$\ln\left(\frac{C_t - C_e}{C_0 - C_e}\right) = -k_1 t \qquad \text{(Eq. 3)}$$

$$\frac{1}{C_t - C_e} - \frac{1}{C_0 - C_e} = k_2 t \qquad \text{(Eq. 4)}$$

The last two equations were employed on the pre-equilibrium data for MB removal at the concentrations of 10.0 mg $L^{-1}$ and 100.0 mg $L^{-1}$. Figures 3.43 and 3.44 show linear fit with first order and second order kinetics, respectively, for MB removal at the concentration of 100.0 mg $L^{-1}$ while Table 3.2 summarizes all the obtained results.
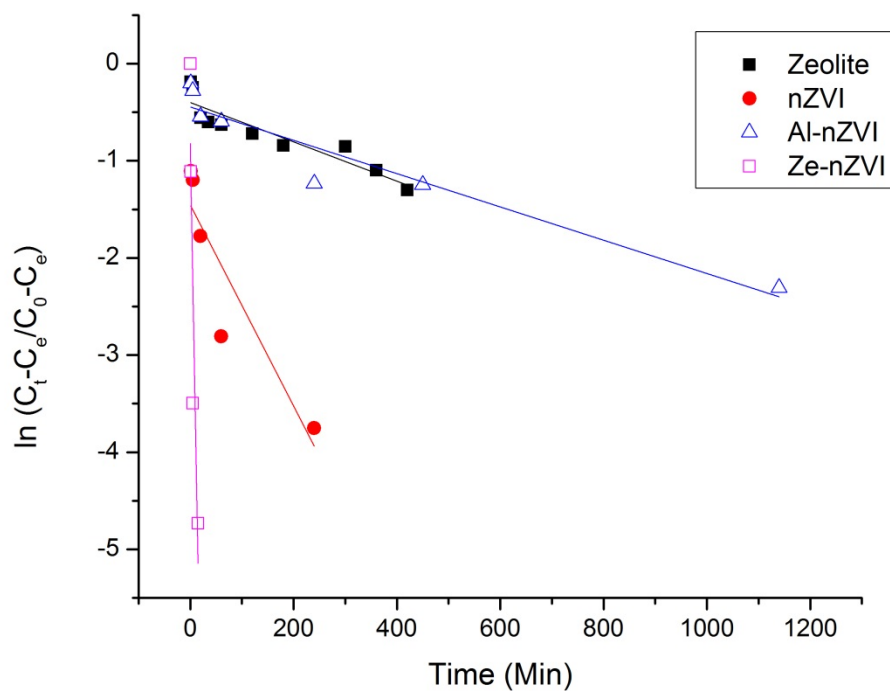


**Figure 3.43 First order linear fit for the removal of MB at initial concentration of 100.0 mg $L^{-1}$**
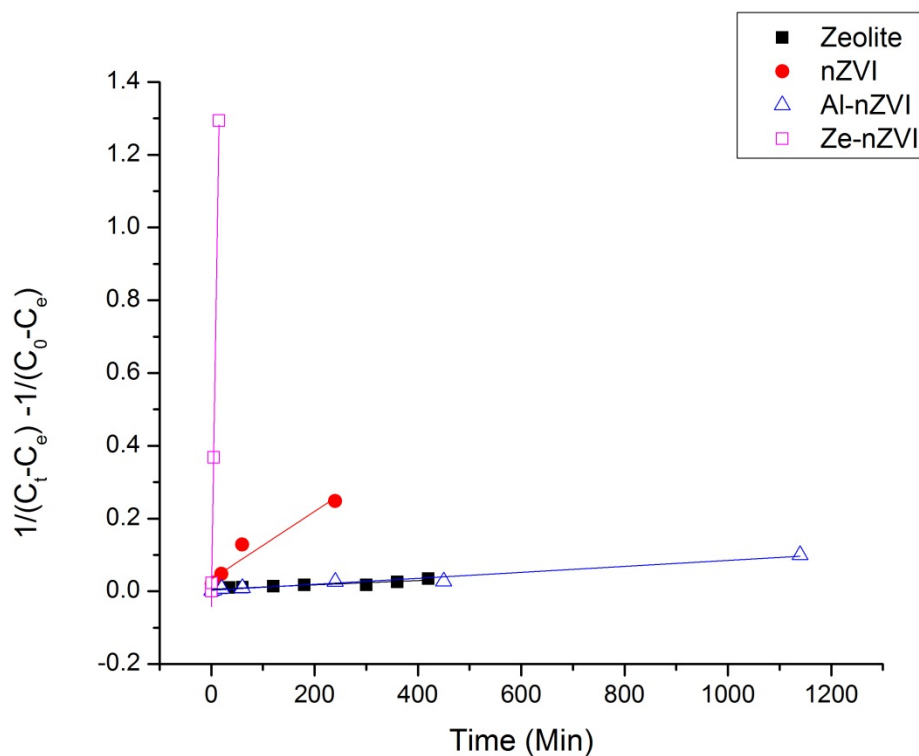
**Figure 3.44 Second order linear fit for the removal of MB at initial concentration of 100.0 mg L$^{-1}$**

**Table 3.2 Rate constants for MB removal processes**

| Sorbent | MB Conc (mg L$^{-1}$) | Equilibrium Time | 1$^{st}$ order | | 2$^{nd}$ order | |
|---------|------|----------|----------|-----|----------|-----|
| | | | $k_1$ (min$^{-1}$) | $R^2$ | $k_2$ (L mg$^{-1}$ min$^{-1}$) | $R^2$ |
| Zeolite | 10 | 20 min | $1.2\pm0.2 \times 10^{-1}$ | 0.9754 | $1.8\pm0.1 \times 10^{-1}$ | 0.9950 |
| | 100 | >24 hr | $2.0\pm0.7 \times 10^{-3}$ | 0.8543 | $5.9\pm1.7 \times 10^{-5}$ | 0.8929 |
| nZVI | 10 | 4 hr | $5.5\pm2.9 \times 10^{-3}$ | 0.9698 | $2.4\pm0.9 \times 10^{-3}$ | 0.9835 |
| | 100 | 4 hr | $1.0\pm0.8 \times 10^{-2}$ | 0.8427 | $1.9\pm0.4 \times 10^{-3}$ | 0.9951 |
| Al-nZVI | 10 | 7 hr | $2.3\pm0.8 \times 10^{-3}$ | 0.9428 | $8.8\pm2.0 \times 10^{-4}$ | 0.9733 |
| | 100 | 19 hr | $1.7\pm0.6 \times 10^{-3}$ | 0.9245 | $8.2\pm1.5 \times 10^{-5}$ | 0.9723 |
| Ze-nZVI | 10 | 15 min | $2.7\pm6.1 \times 10^{-1}$ | 0.9686 | $9.9\pm4.9 \times 10^{-1}$ | 0.9969 |
| | 100 | 15 min | $2.9\pm0.9 \times 10^{-2}$ | 0.8312 | $8.8\pm1.5 \times 10^{-2}$ | 0.9969 |

From the $R^2$ (linear correlation coefficients) values, MB removal using nZVI at both concentrations was adequately described using second order kinetics with rate constants of $2.4\pm0.9\times10^{-3}$ L mg$^{-1}$ min$^{-1}$ and $1.9\pm0.4\times10^{-3}$ L mg$^{-1}$ min$^{-1}$ for the removal of MB at initial concentrations of 10.0 mg L$^{-1}$ and 100.0 mg L$^{-1}$, respectively.

The MB removal using Al-nZVI was better described using second order kinetics with $k_2$ values of $8.8\pm2.0\times10^{-4}$ L mg$^{-1}$ min$^{-1}$ and $8.2\pm1.5\times10^{-5}$ L mg$^{-1}$ min$^{-1}$ at the initial dye concentrations of 10.0 mg L$^{-1}$ and 100.0 mg L$^{-1}$, respectively. In both cases, $k_2$ values were smaller than those of nZVI, hence indicating slower MB removal rate of Al-nZVI compared with nZVI.

The data for the removal of MB at the concentrations of 10.0 mg L$^{-1}$ using zeolite was better described with second order kinetics having $k_2$ value of $1.8\pm0.1\times10^{-1}$ L mg$^{-1}$ min$^{-1}$, which is higher than nZVI value. Moreover, the data of MB removal at 100.0 mg L$^{-1}$ correlated poorly with the two kinetic equations. Using the composite Ze-nZVI, MB removal indicate adequate fits using second order kinetic equation with $k_2$ values of $9.9\pm4.9\times10^{-1}$ L mg$^{-1}$ min$^{-1}$ and $8.8\pm1.5\times10^{-2}$ L mg$^{-1}$ min$^{-1}$ for the two concentrations. Comparing $k_2$

values of Ze-nZVI with the nZVI indicates a much faster MB removal kinetics that can be attributed to the presence of the zeolite crystals between the nZVI chains which served to decrease the aggregation behavior of the nanoparticles, thus enhancing their surface activity. One last thing also worth noting about $k_2$ values for all the adsorbents is the decrease in its value with increasing initial dye concentration.

The effect of time on the removal of the anionic dye MO was also investigated, and the outcome is given in Figure 3.45. It's worth noting that the removal of MO using nZVI was achieved at a much slower rate than MB. This is believed to occur due to the alkaline (negatively charged) surface of nZVI, as the pH during the reduction phase was around pH=9.0, which conveys to the material higher affinity towards cationic dye.
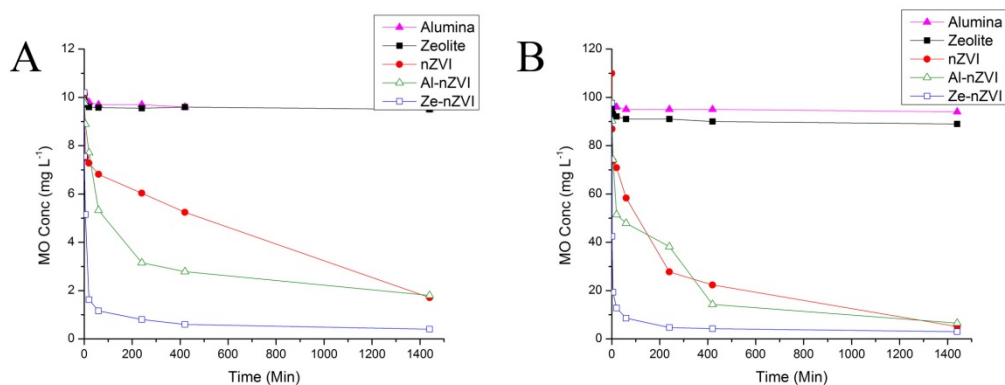


**Figure 3.45 MO removal at initial conc. 10.0 mg L$^{-1}$ (A), and 100.0 mg L$^{-1}$ (B)**

It can be seen that neither alumina nor zeolite was capable of showing any clear MO removal, unlike MB which was effectively removed using zeolite. The composite Ze-nZVI showed the highest MO removal potential at the two studied concentrations. It is interesting to see that, at low initial MO concentration, the dye discoloration using Al-nZVI was more effective than nZVI.

The first and second order kinetic equations were employed on the pre-equilibrium data for MO removal at initial concentrations of 10.0 mg L$^{-1}$ and 100.0 mg L$^{-1}$. Linear fits for first and second order data are plotted in Figure 3.46 and 3.47, respectively.
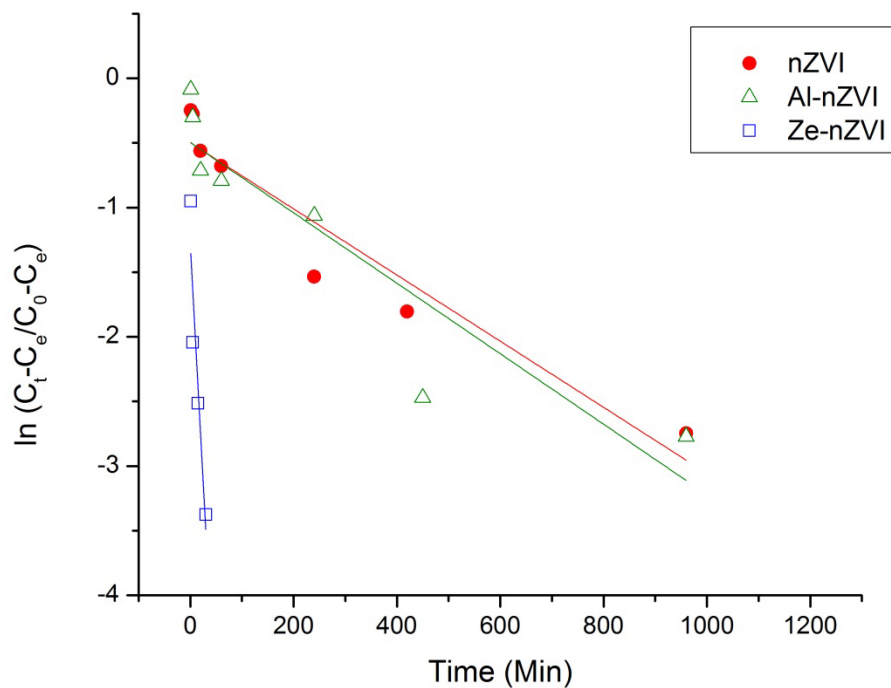


**Figure 3.46 First order linear fit for the removal of MO at 100.0 mg L$^{-1}$**
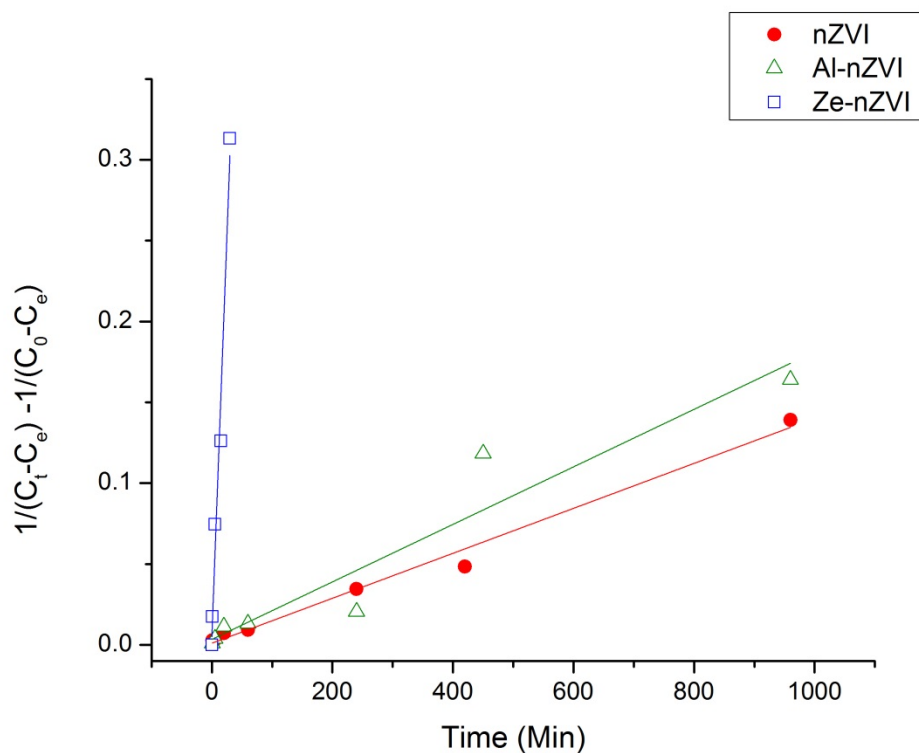
**Figure 3.47 Second order linear fit for the removal of MO at 100.0 mg L$^{-1}$**

**Table 3.3 Rate constants for MO removal processes**

| Sorbent | MO Conc (mg L$^{-1}$) | Equilibrium Time | 1$^{st}$ order | | 2$^{nd}$ order | |
|---|---|---|---|---|---|---|
| | | | $k_1$ (min$^{-1}$) | $R^2$ | $k_2$ (Lmg$^{-1}$min$^{-1}$) | $R^2$ |
| nZVI | 10 | 16 hr | $9.8\pm1.3\times10^{-4}$ | 0.9907 | $2.8\pm0.2\times10^{-3}$ | 0.9963 |
| | 100 | 16 hr | $2.6\pm0.8\times10^{-3}$ | 0.9251 | $1.4\pm0.2\times10^{-4}$ | 0.9892 |
| Al-nZVI | 10 | 4 hr | $1.2\pm0.2\times10^{-2}$ | 0.9916 | $1.1\pm0.3\times10^{-2}$ | 0.9784 |
| | 100 | 19 hr | $2.7\pm1.3\times10^{-3}$ | 0.8566 | $1.8\pm0.6\times10^{-4}$ | 0.9229 |
| Ze-nZVI | 10 | 15 min | $1.9\pm2.7\times10^{-1}$ | 0.9875 | $1.1\pm3.2\times10^{-1}$ | 0.9495 |
| | 100 | 15 min | $7.4\pm8.0\times10^{-2}$ | 0.8861 | $9.8\pm4.8\times10^{-3}$ | 0.9793 |

From the $R^2$ values, MO removal using nZVI at initial
concentration of 10.0 mg L$^{-1}$ gave good correlation with the two

kinetic equations but was described relatively better using second order kinetics, with a rate constant of $2.8\pm0.2\times10^{-3}$ L mg$^{-1}$ min$^{-1}$. The MO removal at initial concentration of 100.0 mg L$^{-1}$ was better described using second order kinetics, and gave a rate constant of $1.4\pm0.2\times10^{-4}$ L mg$^{-1}$ min$^{-1}$. In both cases, the MO removal rate constants were smaller than those corresponding to MB removal using nZVI.

According to the results with Al-nZVI, the removal of MO at initial concentration of 10.0 mg L$^{-1}$ obeys the first order kinetic model with $k_1$ value of $1.2\pm0.2\times10^{-2}$ min$^{-1}$, while the MO removal at initial concentration of 100.0 mg L$^{-1}$ was poorly described using both equations. It's worth noting that MO removal at low concentration using Al-nZVI was much faster than that of nZVI. At high concentration both of Al-nZVI and nZVI demonstrated almost the same removal activity. Moreover, Al-nZVI showed higher MO removal efficiency than MB at low initial concentrations, unlike the previous results obtained in the removal of MB.

Using Ze-nZVI, MO removal at 10.0 mg L$^{-1}$ concentration was adequately described using first order kinetics with $k_1$ value of

$1.9\pm2.7\text{x}10^{-1}$ $\text{min}^{-1}$, while it was better described using second order kinetics at initial concentration of 100.0 mg $\text{L}^{-1}$ with $k_2$ value of $9.8\pm4.8\text{x}10^{-3}$ L $\text{mg}^{-1}$ $\text{min}^{-1}$.

Comparing the rate constants for the removal of both dyes using Ze-nZVI indicates faster cationic dye removal than anionic one, hence confirming the same withdrawn conclusion in the discoloration of both dyes using nZVI. Moreover, MO removal using Ze-nZVI was faster than nZVI, hence in total it can be stated that the composite Ze-nZVI showed faster cationic and anionic dye removal compared with nZVI.

### 3.2.2 Effect of Initial Dye Concentration

The effect of initial concentration on the extent of dyes removal using zeolite, nZVI, Al-nZVI and Ze-nZVI was studied at the initial dye concentrations of 5.0, 10.0, 20.0, 50.0, 100.0 and 200.0 mg $\text{L}^{-1}$. The time of contact was kept at 6 hours, and the experiments were conducted at 25 ℃. The related results are provided in Table 3.4. It can be clearly seen that zeolite demonstrated the highest extent of MB removal at low initial concentrations (lower than 50.0 mg $\text{L}^{-1}$), this could be attributed to the fact that the adsorption of MB on nZVI

occurs on the outer surface of the material, while the adsorption of the

dye on zeolite occurs mostly on the internal pore surface of the

mineral, a process that is usually controlled by pore diffusion and

internal surface diffusion barriers at low initial dye concentrations.

**Table 3.4 Extent of dye removal at 25.0 $^{\circ}$C**

| Initial Conc. (mg L$^{-1}$) | MB | | | | MO | | | |
|---|---|---|---|---|---|---|---|---|
| | Zeolite | nZVI | Al-nZVI | Ze-nZVI | Zeolite | nZVI | Al-nZVI | Ze-nZVI |
| | % Removal | | | | | | | |
| 5.0 | 96.0 | 30.5 | 31.1 | 85.7 | NA | 39.9 | 28.2 | 56.6 |
| 10.0 | 98.9 | 55.6 | 43.3 | 75.1 | NA | 83.1 | 52.8 | 80.3 |
| 20.0 | 98.1 | 87.3 | 56.8 | 90.4 | NA | 88.5 | 46.7 | 81.6 |
| 50.0 | 95.7 | 89.5 | 68.9 | 91.3 | NA | 91.8 | 63.9 | 89.9 |
| 100.0 | 54.6 | 90.9 | 55.5 | 95.1 | NA | 91.0 | 60.6 | 90.5 |
| 200.0 | 58.6 | 96.5 | 72.5 | 96.6 | NA | 90.1 | 52.6 | 90.2 |

Both dyes extent of removal using nZVI, Al-nZVI and Ze-nZVI

increased with increasing initial dye concentration, keeping in mind

that dye removal was slower at higher initial dye concentration as can

be concluded from the previous section, while at high initial dye

concentrations (more than 50 mg L$^{-1}$), the extent of both dyes removal

was higher than 90%. The lower discoloration percentage at lower

concentrations might be attributed to the stronger hydration effects in

the solution.

Using the composite Al-nZVI the dye removal percentage was smaller than their nZVI counterparts. This suggests that the alumina contribution to dye removal is minimal, and that it serves only as a support to decrease the nanoparticles agglomeration.

The results of both dyes removal using Ze-nZVI clearly indicates higher dye removal percentage than the other adsorbents over a wide range of concentrations.

### 3.2.3  Effect of Temperature

The effect of increasing the temperature from 25.0 ℃ to 50.0 ℃ on the extent of dyes removal using nZVI, Al-nZVI and Ze-nZVI was studied at the initial dye concentrations of 5.0, 10.0, 20.0, 50.0, 100.0 and 200.0 mg L$^{-1}$. The time of contact was kept at 6 hours. Results are shown in Table 3.5.

**Table 3.5 Extent of dye removal at 50.0 ℃**

| Initial Conc. (mg L$^{-1}$) | MB | | | MO | | |
|---|---|---|---|---|---|---|
| | nZVI | Al-nZVI | Ze-nZVI | nZVI | Al-nZVI | Ze-nZVI |
| | % Removal | | | | | |
| 5.0 | 56.1 | 43.4 | 92.8 | 82.9 | 40.8 | 66.8 |
| 10.0 | 70.6 | 51.4 | 95.5 | 91.8 | 61.7 | 80.5 |
| 20.0 | 78.2 | 64.4 | 97.3 | 94.0 | 53.5 | 91.9 |
| 50.0 | 90.3 | 74.1 | 92.6 | 96.7 | 68.7 | 97.8 |
| 100.0 | 95.9 | 62.5 | 96.5 | 98.3 | 64.6 | 94.7 |
| 200.0 | 96.6 | 77.6 | 96.9 | 97.1 | 59.1 | 96.9 |

Comparing the dye removal percentages in Table 3.4 with Table 3.5 indicates an obvious increase in the removal of both dyes using the three studied adsorbents at elevated temperatures, hence indicating the endothermic behavior of the dye removal process. This can be referred to the higher molecular mobility of the dyes associated with increasing temperature.

### 3.2.4  Effect of pH

The dye removal percentages using nZVI, Al-nZVI and Ze-nZVI after modifying the initial solution's pH are shown in Figure 3.50. It appears that both dyes removal percentages decreased at high pH values. However, the MO removal % readily decreased from about 90% to 45% at initial pH of 9.0 when was removed using nZVI, while MB removal % when was removed using nZVI decreased only from 95% to 80%, the thing that can be attributed to electrostatic repulsion of the anionic dye at alkaline pH. Moreover, the final solution pH for the removal of MB using nZVI at initial pH of 3.0, 5.0, 7.0 and 9.0 were 5.83, 8.14, 8.73 and 9.23, respectively. On the other hand, the final solution pH for the removal of MO using nZVI at initial pH of

3.0, 5.0, 7.0 and 9.0 were 6.75, 7.76, 7.85 and 8.93. In summary, the discoloration processes of both dyes yield elevation in alkalinity of the medium. The same pH elevation was noticed during the removal of both dyes using Al-nZVI and Ze-nZVI.
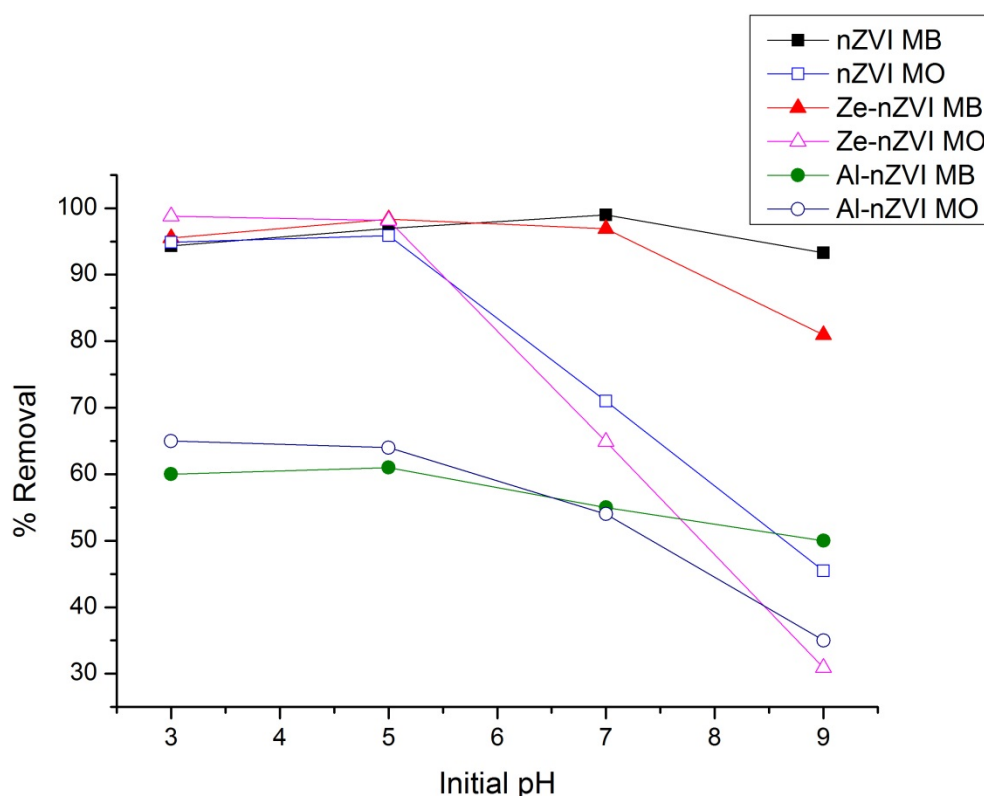


**Figure 3.48 Dye removal % at different initial pH values**

One last thing that is worth noting regarding the two composites Al-nZVI and Ze-nZVI compared to nZVI, is the high pH sensitivity in their efficiency in the dye removal process as can be seen from the higher drop in both dyes removal percentages at high alkaline pH, this is more pronounced with Ze-nZVI than Al-nZVI.

### 3.2.5 Reusability of the Adsorbents

The reusability of nZVI, Al-nZVI and Ze-nZVI in the removal of MB and MO was also investigated. According to the results, stable removal percentage of both dyes was observed for about four successive trials using nZVI and Al-nZVI, moreover, Ze-nZVI demonstrated longer reusability for another fifth trial as shown in Figure 3.49.
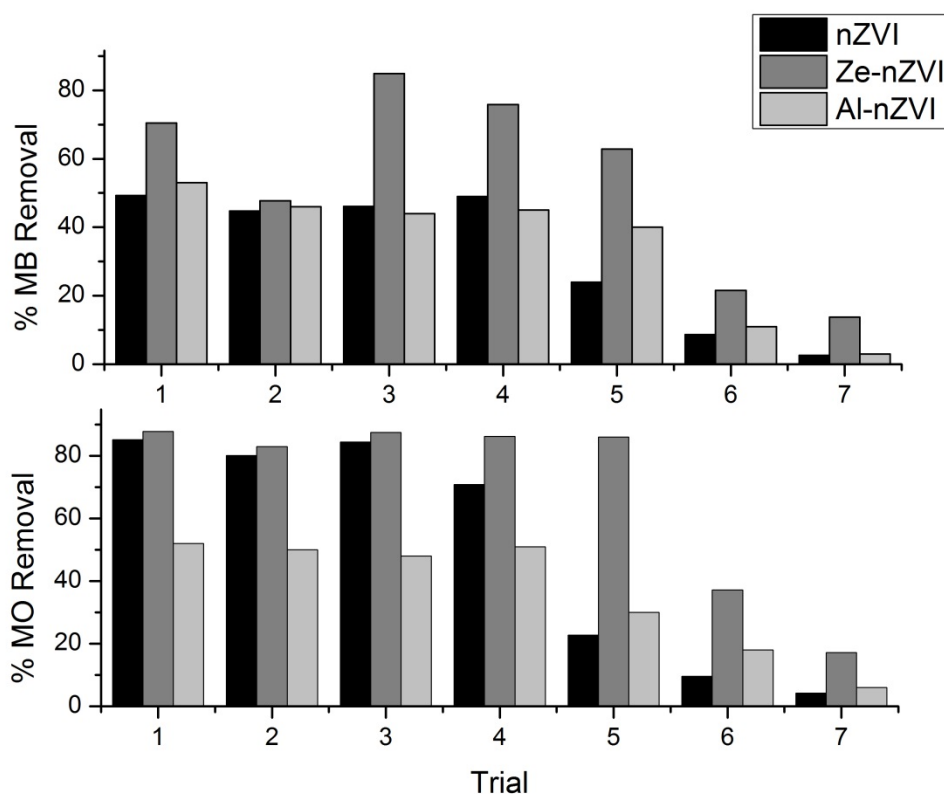


**Figure 3.49 Reusability of nZVI, Al-nZVI and Ze-nZVI in dye removal**

This shows that nZVI does not lose its discoloration ability upon oxidation, and consequently than iron oxide and oxyhydroxide continue to display effective removal. This, however, is expected to have implications on the discoloration mechanism. Moreover, the longer reusability of Ze-nZVI is believed to occur due to the imparted stability of the nanoparticles chains due to the presence of zeolite crystals between the nanoparticles chains which causes lesser aggregation and so higher dye removal longevity and reusability.

### 3.2.6  Desorption Studies

The assessment of desorption of both dyes from nZVI after being used in the removal process is shown in Figure 3.50. It can be seen that both dyes concentration in the deionized water after the first day of desorption period were about 5 mg $L^{-1}$. This small amount of desorbed dye can be attributed to partially sorbed dye on the nZVI surface. Moreover, no obvious dye desorption was noticed during the eight successive days thereafter, hence indicating that the mechanism of the dye removal could be: (I) degradation process, (II) strong irreversible adsorption or (III) combination of both.
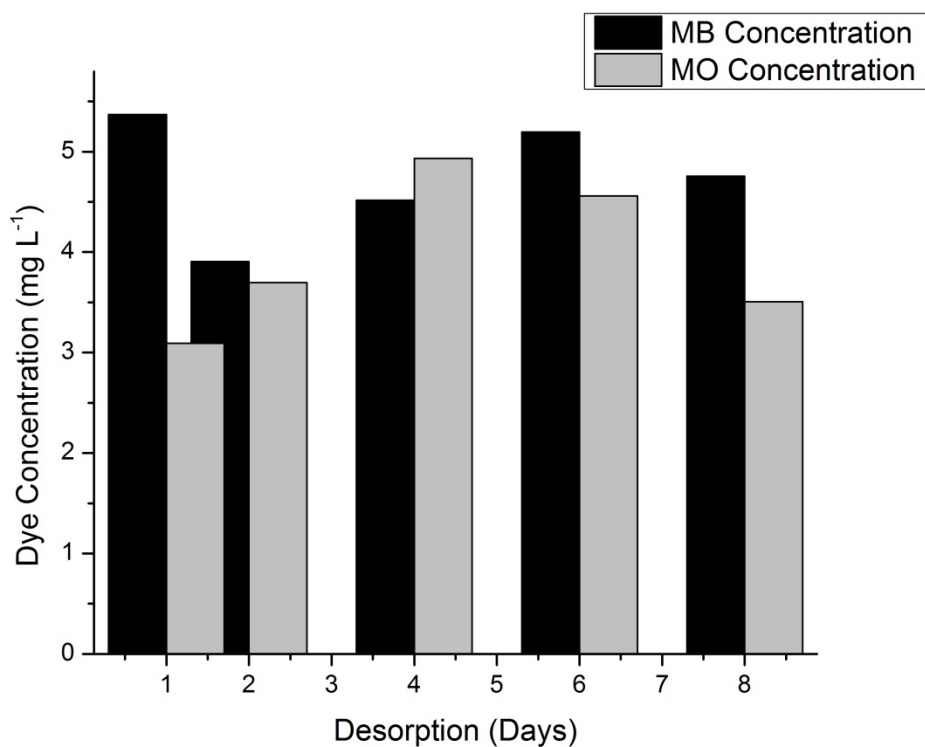
**Figure 3.50 MB and MO desorption from nZVI**

### 3.2.7  nZVI as a Fenton Catalyst

An interesting application of nZVI is to employ it as a Fenton catalyst. Fenton system is an oxidation technique that involves the usage of hydrogen peroxide and an iron source to generate hydroxyl radicals which in turn serves in the degradation of organic molecules. The results related to this part were reported in a recent publication by our group. [89] The related experiments were performed at MB initial concentrations of 10.0 and 100.0 mg $L^{-1}$, and the results are shown in

Figure 3.51. Compared with the previous results obtained in the absence of $H_2O_2$, the removal of MB by the Fenton mechanism (see Figure 3.42) seems to be slower at high MB initial concentrations, and faster at low initial MB concentration.
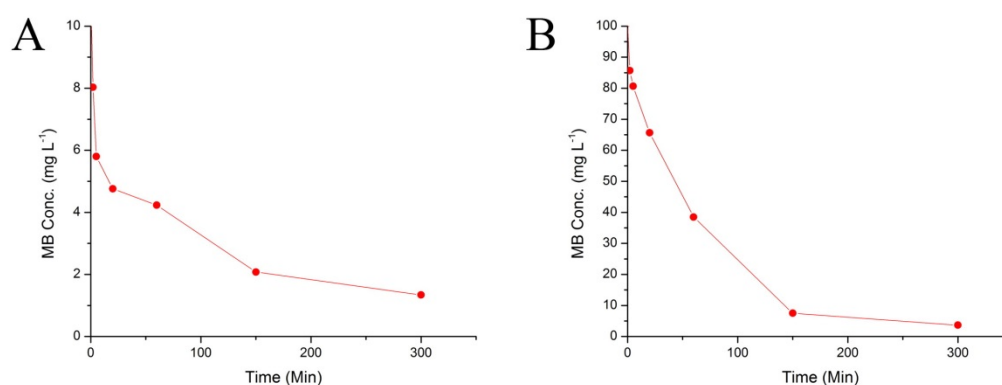


**Figure 3.51 MB removal using nZVI as a Fenton catalyst at 10.0 mg L$^{-1}$ (A), and 100.0 mg L$^{-1}$ (B)**

The first and second order kinetic equations were employed for the pre-equilibrium data of MB disscoloration at the concentrations of 10.0 mg L$^{-1}$ (Figure 3.52) and 100.0 mg L$^{-1}$ (Figure 3.53). From the $R^2$ values, MB removal at initial concentration of 10.0 mg L$^{-1}$ gave poor correlation with both kinetic equations. While MB removal at initial concentration of 100.0 mg L$^{-1}$, was adequately described using both kinetic equations with $k_1$ constant of $1.58 \pm 0.9 \times 10^{-2}$ min$^{-1}$ and $k_2$ constant of $3.4 \pm 0.9 \times 10^{-4}$ L mg$^{-1}$ min$^{-1}$, which is lower than $k_2$ obtained upon using nZVI solely.
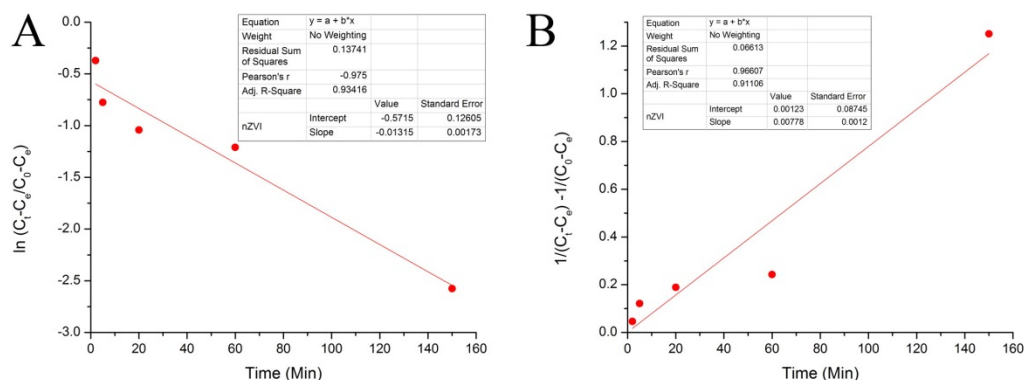
**Figure 3.52 First order (A), and second order (B) kinetics for the removal of 10.0 mg L$^{-1}$ MB using nZVI as a Fenton catalyst**
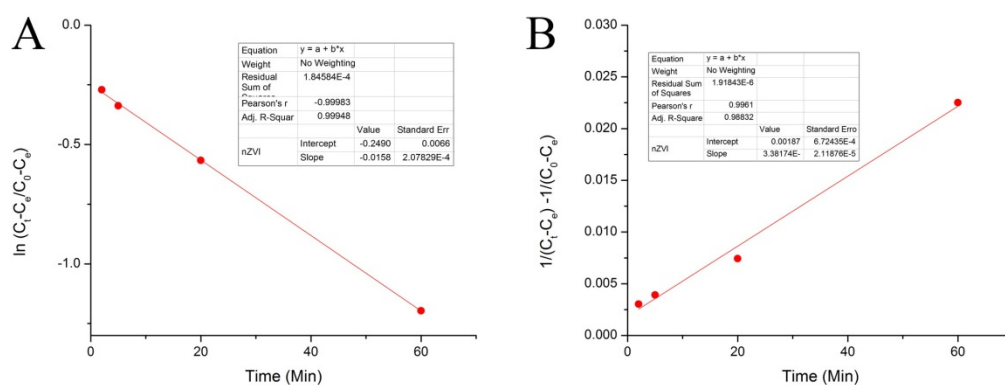


**Figure 3.53 First order (A), and second order (B) kinetics for the removal of 100.0 mg L$^{-1}$ MB using nZVI as a Fenton catalyst**

The effect of time on the removal of the anionic dye MO was also investigated using Fenton operation, and the obtained results are given in Figure 3.54. In the removal of MO using nZVI as a Fenton-like catalyst, equilibrium was achieved at a much slower rate than MB, which is inline with the results reported previously, in the absence of $H_2O_2$.
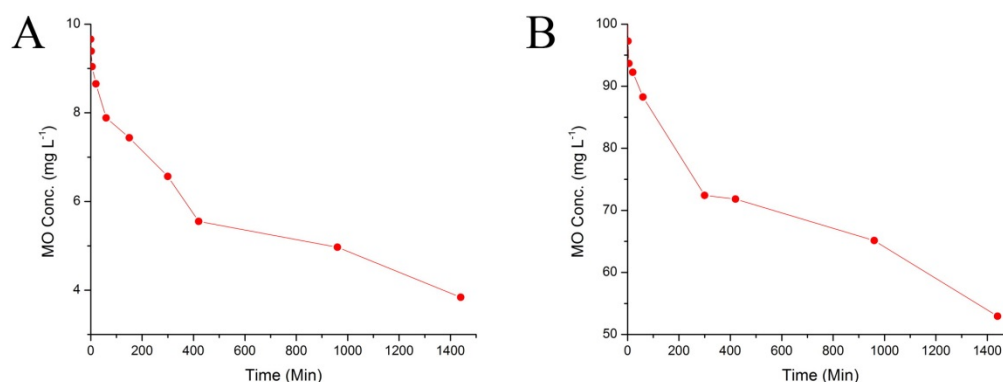
**Figure 3.54 MO removal using nZVI as a Fenton catalyst at 10.0 mg L$^{-1}$ (A), and 100.0 mg L$^{-1}$ (B)**

The first and second order kinetic equations were employed for the pre-equilibrium data of MO removal at the concentrations of 10.0 mg L$^{-1}$ (Figure 3.55) and 100.0 mg L$^{-1}$ (Figure 3.56). From the R$^2$ values, MO removal can be described more adequately using the 2$^{nd}$ order kinetics, and the k$_2$ values were $7.5\pm1.1\times10^{-4}$ L mg$^{-1}$ min$^{-1}$ and $6.2\pm1.2\times10^{-5}$ L mg$^{-1}$ min$^{-1}$ at the initial concentrations of 10.0 mg L$^{-1}$ and 100.0 mg L$^{-1}$, respectively. Comparing k$_2$ values for the removal of MO using nZVI in the presence and absence of H$_2$O$_2$ confirms the same conclusion as with the removal of MB, i.e. slower removal at high initial concentrations and faster removal at low initial MO concentration.
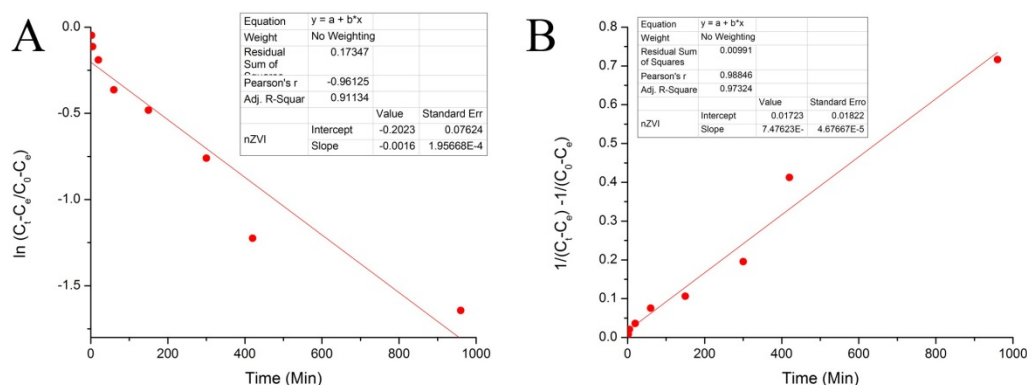
**Figure 3.55 First order (A). and second order (B) kinetics for the removal of 10 mg L$^{-1}$ MO using nZVI as a Fenton catalyst**
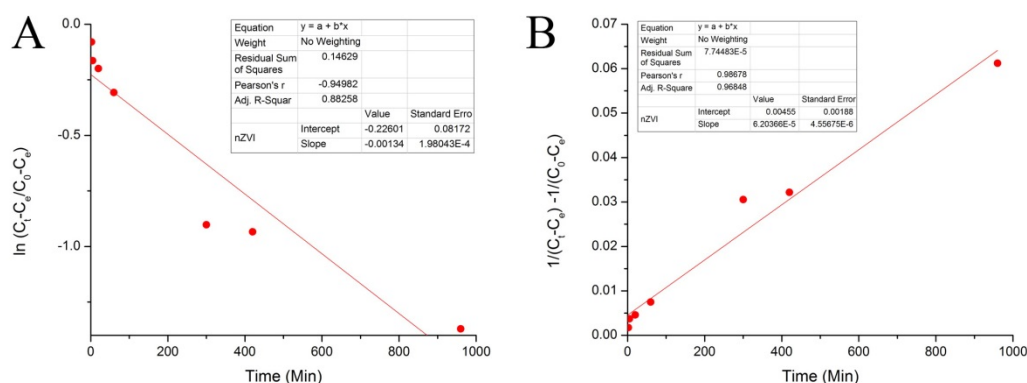


**Figure 3.56 First order (A) and second order (B) kinetics for the removal of 100 mg L$^{-1}$ MO using nZVI as a Fenton catalyst**

## 3.2.8 Dye Removal Using a Continuous Column Flow System

In a separate set of experiments, the discoloration ability of nZVI was investigated under continuous flow. For this purpose, nZVI was used as a filling material in a glass column designed for this purpose. The flow system resulted in about 100% dye removal for the first 11 successive portions with 2 mL in each. However, due to the oxidation and aggregation of nZVI the column was totally clogged

and no further portions of dye solution could be collected, hence indicating the difficulty of using nZVI solely as a filling material in continuous column flow system.
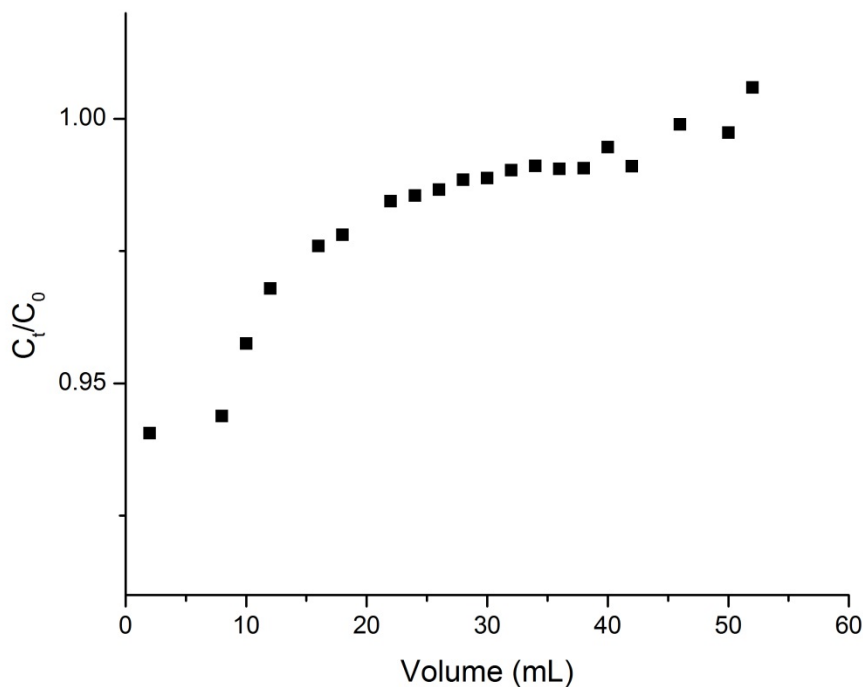


**Figure 3.57 Breakthrough curve for the removal of MB using alumina**

Using alumina as the filling material in a continuous column flow system for the removal of 10.0 mg L$^{-1}$ MB solution brought about 5% dye removal from the first collected portion. MB portions were successively collected till a breakthrough curve was constructed as shown in Figure 3.57. Al-nZVI was employed as a filling material in the column and it showed about 100% dye removal for about 10

portions with 2 mL in each. Then as was the case with nZVI the column was clogged and no further samples were collected. The results illustrate the efficiency of iron- based materials in flow operations; however, further work is needed to develop appropriate filters for such operations.

Application of Ze-nZVI as a filling material in a continuous column flow system for the removal of 100.0 mg $L^{-1}$ MB solution brought about 100% dye removal for several successive trials that were collected into 2 mL portions. The number of collected portions reached about 30, which is much higher than nZVI and Al-nZVI before the column was clogged. This imparted longevity of the column system using Ze-nZVI indicates more success in using nano iron based materials with such flow systems. Still, further studies should be sought for the sake of development of appropriate filters for such operations.

### 3.2.9 Dye Degradation Products Study

Trials to identify the presence of any degradation products for MB treated solution after contact with nZVI resulted in the appearance of numerous peaks in the GC chromatogram that might be attributed

to the nature of MB which decomposes at around 110 ℃, hence leaving hardship in differentiating between MB decomposition products or those of any possible degradation using nZVI.

MO removal using nZVI has been previously reported[50] to be an adsorption and reduction process to sulfanilic acid, N,N-dimethyl-p-phenylenediamine and N-methyl-p-phenylenediamine. However, the use of alumina and acetonitrile in the solid phase extraction to identify those products resulted with failure in identifying any of the mentioned products. Yet, further studies are needed to confirm and identify any dye degradation products using different solvents or extraction methods.

## Conclusion

Iron nanoparticles (nZVI) and iron nanoparticles supported on natural zeolite (Ze-nZVI) and alumina (Al-nZVI) were prepared and characterized using XRD, XPS, FTIR, SEM, TEM, EDX and BET-$N_2$. The characterization confirms the presence of iron nanoparticles chains on the support material in a manner resembling nZVI.

All the prepared materials were successfully applied in the removal of the cationic dye methylene blue (MB) and anionic dye methyl orange (MO) over a wide range of concentrations.

Supporting nZVI with alumina caused a decrease in MB removal speed and a slight increase in MO removal speed. The extent of dye removal using Al-nZVI was lower in comparison with nZVI. Supporting nZVI with zeolite resulted in large increase in both dyes removal speed, higher extent of dyes removal, and better dye removal longevity.

Almost in all dye removal processes, the removal of the cationic dye (MB) was faster than that of the anionic dye (MO). The dye removal process in all the prepared materials has increased with increasing temperature, suggesting an endothermic behavior. Moreover, the dye removal percentage increased with increasing initial dye concentration, and decreased at higher solution pH's.

The nZVI-based materials were employed in column-type removal of the dyes. The breakthrough curves suggested successful removal, however, further work is recommended to develop more appropriate filters to enhance the performance of the columns.

# References

1. Wikipedia. http://en.wikipedia.org/wiki/Water (accessed January 23, 2012).

2. Christie, R. *Environmental Aspects of Textile Dyeing,* 1st ed.; CRC Press: Cambridge, 2007.

3. Gordon, P.; Gregory, P. *Organic Chemistry in Colour;* Springer: Berlin, 1983.

4. Hunger, K. *Industrial Dyes: Chemistry, Properties, Applications.;* Wiley-VCH: Weinheim, 2003.

5. Gupta, V. K.; Suhas. Application of low-cost adsorbents for dye removal – A review. *J. Environ. Manage.* **2009,** *90 ,* 2313–2342.

6. Demirbas, A. Agricultural based activated carbons for the removal of dyes from aqueous solutions: A review. *J. Hazard. Mater.* **2009,** *167,* 1-9.

7. Mohd Salleh, M. A.; Mahmoud, D. K.; Abdul Karim, W. A.; Idris, A. Cationic and anionic dye adsorption by agricultural solid wastes: A comprehensive review. *Desalination* **2011,** *280,* 1-13.

8. Zollinger, H. *Color Chemistry: syntheses, properties, and applications of organic dyes and pigments,* 3rd ed.; Lost Helvetica Chimica Acta: Zurich, 2003.

9. Mohan, N.; Balasubramanian, N.; Ahmed Basha, C. Electrochemical oxidation of textile wastewater and its reuse. *J. Hazard. Mater.* **2007,** *147,* 644-651.

10. Ganesh, R.; Boardman, G. D.; Michelson, D. Fate of azo dyes in sludges. *Water Res.* **1994,** *28,* 1367–1376.

11. Malik, R.; Ramteke, D. S.; Wate, S. R. Adsorption of malachite green on groundnut shell waste based powdered activated carbon. *Waste Manage.* **2007,** *27,* 1129–1138.

12. Garg, V. K.; Amita, M.; Kumar, R.; Gupta, R. Basic dye (methylene blue) removal from simulated wastewater by adsorption using Indian Rosewood

sawdust: a timber industry waste. *Dyes Pigm.* **2004,** *63,* 243-250.

13. McKay, G.; Otterburn, M. S.; Sweeney, A. G. The removal of colour from effluent using various adsorbents. III. Silica: rate process. *Water Res.* **1980,** *14,* 15-20.

14. Pan, H.; Feng, J.; He, G.; Cerniglia, C. E.; Chen, H. Evaluation of impact of exposure of Sudan azo dyes and their metabolites on human intestinal bacteria. *Anaerobe* **2012,** *18,* 445-453.

15. Selvam, K.; Swaminathan, K.; Chae, K. S. Microbial decolorization of azo dyes and dye industry effluent by Fomes lividus. *World J. Microbiol. Biotechnol.* **2003,** *19,* 591–593.

16. Mu, Y.; Rabaey, K.; Rozendal, R. A.; Yuan, Z.; Keller, J. Decolorization of Azo Dyes in Bioelectrochemical Systems. *Environ. Sci. Technol.* **2009,** *43,* 5137–5143.

17. Ramakrishna, K. R.; Viraraghavan, T. Dye removal using low cost adsorbents. *Water Sci. Technol.* **1997,** *36,* 189-196.

18. Sulak, M. T.; Demirbas, E.; Kobya, M. Removal of Astrazon Yellow 7GL from aqueous solutions by adsorption onto wheat bran. *Biores. Technol.* **2007,** *98,* 2590–2598.

19. Chuah, T. G.; Jumasiah, A.; Katayon, A. S.; Choong, S. Y. Rice husk as a potentially low-cost biosorbent for heavy metal and dye removal: an overview. *Desalination* **2005,** *175,* 305-316.

20. Ali, I. New Generation Adsorbents for Water Treatment. *Chem. Rev.* **2012,** *112,* 5073–5091.

21. Dabrowski, A. Adsorption — from theory to practice. *Adv. Colloid Interface. Sci.* **93,** *2001,* 135-224.

22. Stewart, R. *Environmental Science in the 21st Century - An Online Textbook;* Texas A&M University, 2008.

23. Mackay, D. M.; Cherry, J. A. Groundwater contamination: pump-and-treat remediation. *Environ. Sci. Technol.* **1989,** *23 ,* 630–636.

24. Higgins, M. R.; Olson, T. M. Life-Cycle Case Study Comparison of Permeable Reactive Barrier versus Pump-and-Treat Remediation. *Environ. Sci. Technol.* **2009,** *43 ,* 9432–9438.

25. Zhang, W. Nanoscale iron particles for environmental remediation: An overview. *J. Nanopart.Res.* **2003,** *5,* 323–332.

26. Glazier, R.; Venkatakrishnan, R.; Gheorghiu, F. W. L. N. R.; Zhang, W. Nanotechnology Takes the Root. *Civil Engineering* **2003,** *73,* 64-69.

27. Blowes, D. W.; Ptacek, C. J.; Benner, S. J.; McRae, C. W.; Bennett, T. A.; Puls, R. W. Treatment of inorganic contaminants using permeable reactive barriers. *J. Contam. Hydrol.* **2000,** *45,* 123-137.

28. *United States Environmental Protection Agency;* 2002: Washington, DC, Field Applications of In Situ Remediation Technologies: Permeable Reactive Barriers.

29. Henderson, A. D.; Demond, A. H. Long-Term Performance of Zero-Valent Iron Permeable Reactive Barriers: A Critical Review. *Environ. Eng. Sci.* **2007,** *24,* 401-423.

30. Cantrell, K. J.; Kaplan, D. I.; Wietsma, T. W. Zero-valent iron for the in situ remediation of selected metals in groundwater. *J. Hazard. Mater* **1995,** *42,* 201-212.

31. Benner, S. G.; Herbert, R. B. J.; Blowes, D. W.; Ptacek, C. J.; Gould, D. Geochemistry and microbiology of a permeable reactive barrier for acid mine drainage. *Environ. Sci. Technol.* **1999,** *33,* 2793–2799.

32. Baker, M. J.; Blowes, D. W.; Ptacek, C. J. Phosphorous Adsorption and Precipitation in a Permeable Reactive Wall: Applications for Wastewater Disposal Systems. *Land Contam. Reclam.* **1997,** *5,* 189–193.

33. Phillips, D. H.; Van Nooten, T.; Bastiaens, L.; Russell, M. I.; Dickson, K.; Plant, S.; Ahad, J. E.; Newton, T.; Elliot, T.; Kalin, R. M. Ten Year Performance Evaluation of a Field-Scale Zero-Valent Iron Permeable Reactive Barrier Installed to Remediate Trichloroethene Contaminated Groundwater. *Envrion. Sci. Technol.* **2010,** *44,* 3861-3869.

34. Qu, X.; Brame, J.; Li, Q.; Alvarez, P. J. Nanotechnology for a Safe and Sustainable Water Supply: Enabling Integrated Water Treatment and Reuse.

*Acc. Chem. Res.* **2013,** *46,* 834–843.

35. Wang, C.-B.; Zhang, W.-X. Synthesizing Nanoscale Iron Particles for Rapid and Complete Dechlorination of TCE and PCBs. *J. Environ. Sci. Technol.* **1997,** *31,* 2154–2156.

36. Wikipedia. http://en.wikipedia.org/wiki/Iron (accessed February 12, 2012).

37. Vanysek, P. Electrochemical Series. In *CRC Handbook of Chemistry and Physics,* 89th ed.; Lide, D. R., Ed.; Taylor and Francis Group: Boca Raton, 2009; pp 8-20.

38. Gillham, R. W.; O'Hannesin, S. F. Enhanced degradation of halogenated aliphatics by zero valent iron. *Ground Water* **1994,** *32,* 958-967.

39. Lien, H. L.; Wilkin, R. T. High-level arsenite removal from groundwater by zero-valent iron. *Chemosphere* **2005,** *59,* 377-386.

40. Chuang, F. W.; Larson, R. A.; Wessman, M. S. Zero-valent iron-promoted dechlorination of polychlorinated-biphenyls. *Environ. Sci. Technol.* **1995,** *29,* 2460–2463.

41. Sayles, G. D.; You, G. R.; Wang, M. X.; Kupferle, M. J. DDT, DDD, and DDE Dechlorination by Zero-Valent Iron. *Environ. Sci. Technol.* **1997,** *31,* 3448–3454.

42. Agrawal, A.; Tratnyek, P. G. Reduction of Nitro Aromatic Compounds by Zero-Valent Iron Metal. *Environ. Sci. Technol.* **1996,** *30,* 153–160.

43. Cheng, I. F.; Muftikian, R.; Fernando, Q.; Korte, N. Reduction of nitrate to ammonia by zero-valent iron. *Chemosphere* **1997,** *35,* 2689–2695.

44. O'Carroll, D.; Sleep, B.; Krol, M.; Boparai, H.; Kocur, C. Nanoscale zero valent iron and bimetallic particles for contaminated site remediation. *Adv. Water Resour.* **2013,** *51,* 104–122.

45. Ponder, S. M.; Darab, J. G.; Mallouk, T. E. Remediation of Cr(VI) and Pb(II) Aqueous Solutions Using Supported, Nanoscale Zero-valent Iron. *Environ. Sci. Technol.* **2000,** *34,* 2564-2569.

46. Service, R. F. Superstrong Nanotubes Show They Are Smart, Too. *Science*

**1998,** *281,* 940-942.

47. Huber, D. L. Synthesis, Properties, and Applications of Iron Nanoparticles. *Small* **2005,** *1,* 482 –501.

48. Li, L.; Fan, M.; Brown, R. C.; Leeuwen, J. V. W. J.; Wang, W.; Song, Y.; Zhang, P. Synthesis, Properties, and Environmental Applications of Nanoscale Iron-Based Materials: A Review. *Crit. Rev. Environ. Sci. Technol.* **2006,** *36,* 405-431.

49. Ghauch, A.; Tuqan, A.; Abou Assi, H. Antibiotic removal from water: Elimination of amoxicillin and ampicillin by microscale and nanoscale iron particles. *Eniron. Pollut.* **2009,** *157 ,* 1626–1635.

50. Fan, J.; Guo, Y.; Wang, J.; Fan, M. Rapid decolorization of azo dye methyl orange in aqueous solution by nanoscale zerovalent iron particles. *J. Hazard. Mater.* **2009,** *166 ,* 904–910.

51. Elliott, D. W.; Lien, H. L.; Zhang, W. X. Degradation of Lindane by Zero-Valent Iron Nanoparticles. *J. Environ. Eng.* **2009,** *135 ,* 317–325.

52. Ambashta, R. D.; Repo, E.; Sillanpaa, M. Degradation of Tributyl Phosphate Using Nanopowders of Iron and Iron–Nickel under the Influence of a Static Magnetic Field. *Ind. Eng. Chem. Res.* **2011,** *50 ,* 11771–11777.

53. Naja, G.; Halasz, A.; Thiboutot, S.; Ampleman, G.; Hawari, J. Degradation of Hexahydro-1,3,5-trinitro-1,3,5-triazine (RDX) Using Zerovalent Iron Nanoparticles. *Environ. Sci. Technol.* **2008,** *42,* 4364–4370.

54. Zhang, X.; Lin, Y.; Chen, Z. 2,4,6-Trinitrotoluene reduction kinetics in aqueous solution using nanoscale zero-valent iron. *J. Hazard. Mater.* **2009,** *165,* 923–927.

55. Cheng, R.; Wang, J.; Zhang, W. Comparison of reductive dechlorination of p-chlorophenol using Fe0 and nanosized Fe0. *J. Hazard. Mater.* **2007,** *144,* 334–339.

56. A., L.; Tai, C.; Zhao, Z.; Wang, Y.; Zhang, Q.; Jiang, H.; Hu, J. Debromination of Decabrominated Diphenyl Ether by Resin-Bound Iron Nanoparticles. *Environ. Sci. Technol.* **2007,** *41 ,* 6841–6846.

57. Varanasi, P.; Fullana, A.; Sidhu, S. Remediation of PCB contaminated soils using iron nano-particles. *Chemosphere* **2007,** *66 ,* 1031–1038.

58. Choe, S.; Chang, Y. Y.; Hwang, K. Y.; Khim, J. Kinetics of reductive denitrification by nanoscale zero-valent iron. *Chemosphere* **2000,** *41,* 1307-1311.

59. Xiong, Z.; Zhao, D.; Pan, G. Rapid and complete destruction of perchlorate in water and ion-exchange brine using stabilized zero-valent iron nanoparticles. *Water Res.* **2007,** *41,* 3497–3505.

60. Celebi, O.; Uzum, C.; Shahwan, T.; Erten, H. N. A radiotracer study of the adsorption behavior of aqueous Ba2+ ions on nanoparticles of zero-valent iron. *J. Hazard. Mater.* **2007,** *148 ,* 761–767.

61. Klimkova, S.; Cernik, M.; Lacinova, L.; Filip, J.; Jancik, D.; Zboril, R. Zero-valent iron nanoparticles in treatment of acid mine water from in situ uranium leaching. *Chemosphere* **2011,** *82,* 1178–1184.

62. Uzüm, C.; Shahwan, T.; Eroglu, A. E.; Lieberwirth, I.; Scott, T.; Hallam, K. Application of zero-valent iron nanoparticles for the removal of aqueous Co2+ ions under various experimental conditions. *Chem. Eng. J.* **2008,** *144,* 213-220.

63. Karabelli, D.; Uzum, C.; Shahwan, T.; Eroglu, A. E.; Scott, T.; Hallam, K.; Lieberwirth, I. Batch Removal of Aqueous Cu2+ Ions Using Nanoparticles of Zero-Valent Iron: A Study of the Capacity and Mechanism of Uptake. *Ind. Eng. Chem. Res.* **2008,** *47,* 4758-4764.

64. Efecan, N.; Shahwan, T.;. Eroglu, A. E.; Lieberwirth, I. Characterization of the uptake of aqueous Ni2+ ions on nanoparticles of zero valent iron. *Desalination* **2009,** *249,* 1048-1054.

65. Li, X. Q.; Zhang, W. X. Sequestration of Metal Cations with Zerovalent Iron NanoparticlesA Study with High Resolution X-ray Photoelectron Spectroscopy (HR-XPS). *J. Phys. Chem. C* **2007,** *111,* 6939-6946.

66. Kanel, S. R.; Manning, B.; Charlet, L.; Choi, H. Removal of Arsenic(III) from Groundwater by Nanoscale Zero-Valent Iron. *Environ. Sci. Technol.* **2005,** *39,* 1291–1298.

67. Olegario, J. T.; Yee, N.; Miller, M.; Sczepaniak, J.; Manning, B. Reduction of Se(VI) to Se(-II) by zerovalent iron nanoparticle suspensions. *J. Nanopart. Res.* **2010,** *12,* 2057–2068.

68. Dickinson, M.; Scott, T. B. The application of zero-valent iron nanoparticles for the remediation of a uranium-contaminated waste effluent. *J. Hazard. Mater.* **2010,** *178,* 171–179.

69. Crane, R. A.; Scott, T. B. Nanoscale zero-valent iron: Future prospects for an emerging water treatment technology. *J. Hazard. Mater.* **2012,** *211-212,* 112-125.

70. Miehr, R.; Tratnyek, P. G.; Bandstra, J. Z.; Scherer, M. M.; Alowitz, M. J.; Bylaska, E. J. Diversity of Contaminant Reduction Reactions by Zerovalent Iron:  Role of the Reductate. *Enivron. Sci. Technol.* **2004,** *38,* 139–147.

71. Sun, Y. P.; Li, X. Q.; Cao, J.; Zhang, W. X.; Wang, H. P. Characterization of zero-valent iron nanoparticles. *Adv. Colloid Interface Sci.* **2006,** *120 ,* 47–56.

72. Nurmi, J. T.; Tratnyek, P. G.; Sarathy, V.; Baer, D. R.; Amonette, J. E.; Pecher, K.; Wang, C.; Linehan, J.; Matson, D. W.; Penn, R. L.; Driessen, M. D. Characterization and Properties of Metallic Iron Nanoparticles: Spectroscopy, Electrochemistry, and Kinetics. *Environ. Sci. Technol.* **2005,** *39,* 1221–1230.

73. Li, X. Q.; Elliott, D. W.; Zhang, W. X. Zero-Valent Iron Nanoparticles for Abatement of Environmental Pollutants: Materials and Engineering Aspects. *Crit. Rev. Solid State Mater. Sci.* **2006,** *31,* 111–122.

74. Gavaskar, A.; Tatar, L.; Condit, W. *Cost and performance report nanoscale zero-valent iron technologies for source remediation;* Contract Report; NAVFAC: California, 2005.

75. Phenrat, T.; Saleh, N.; Sirk, K.; Tilton, R. D.; Lowry, G. V. Aggregation and sedimentation of aqueous nanoscale zerovalent iron dispersions. *Environ. Sci. Technol.* **2007,** *41,* 284-290.

76. Ninham, B. W. On progress in forces since the DLVO theory. **1999,** *83,* 1-17.

77. Hong, Y. S.; Honda, R. J.; Myung, N. V.; Walker, S. L. Transport of Iron-Based Nanoparticles: Role of Magnetic Properties. *Environ. Sci. Eng.* **2009,**

*43,* 8834–8839.

78. Sirk, K. M.; Saleh, N. B.; Phenrat, T.; Kim, H. J.; Dufour, B.; Ok, J.; Golas, P. L.; Matyjaszewski, K.; Lowry, G. V.; Tilton, R. D. Effect of Adsorbed Polyelectrolytes on Nanoscale Zero Valent Iron Particle Attachment to Soil Surface Models. *Environ. Sci. Technol.* **2009,** *43,* 3803–3808.

79. Phenrat, T.; Saleh, N.; Sirk, K.; Kim, H. J.; D., T. R.; Lowry, G. V. Stabilization of aqueous nanoscale zerovalent iron dispersions by anionic polyelectrolytes: adsorbed anionic polyelectrolyte layer properties and their effect on aggregation and sedimentation. *J. Nanopart. Res.* **2008,** *10,* 795–814.

80. Tiraferri, A.; Chen, K. L.; Sethi, R.; Elimelech, M. Reduced aggregation and sedimentation of zero-valent iron nanoparticles in the presence of guar gum. *J. Colloid Interface Sci.* **2008,** *324 ,* 71–79.

81. Hydutsky, B. W.; Mack, E. J.; Beckerman, B. B.; Skluzacek, J. M.; Mallouk, T. E. Optimization of Nano- and Microiron Transport through Sand Columns Using Polyelectrolyte Mixtures. *Environ. Sci. Technol.* **2007,** *41,* 6418–6424.

82. Schrick, B.; Hydutsky, B. W.; Blough, J. L.; Mallouk, T. E. Delivery Vehicles for Zerovalent Metal Nanoparticles in Soil and Groundwater. *Chem. Mater.* **2004,** *16,* 2187–2193.

83. Kanel, S. R.; Nepal, D.; Manning, B.; Choi, H. Transport of surface-modified iron nanoparticle in porous media and application to arsenic(III) remediation. *J. Nanopart. Res.* **2007,** *9,* 725–735.

84. Sun, Y.; Li, X.; Zhang, W.; Wang, H. A method for the preparation of stable dispersion of zero-valent iron nanoparticles. *Physicochem. Eng. A* **2007,** *308,* 60-66.

85. Saleh, N.; Phenrat, T.; Sirk, K.; Dufour, B.; Ok, J.; Sarbu, T.; Matyjaszewski, K.; Tilton, R.; Lowry, G. Adsorbed Triblock Copolymers Deliver Reactive Iron Nanoparticles to the Oil/Water Interface. *Nano Lett.* **2005,** *5,* 2489–2494.

86. Comba, S.; Sethi, R. Stabilization of highly concentrated suspensions of iron nanoparticles using shear-thinning gels of xanthan gum. *Water Res.* **2009,** *43,* 3717–3726.

87. Phenrat, T.; Liu, Y.; Tilton, R. D.; Lowry, G. V. Adsorbed Polyelectrolyte Coatings Decrease Fe0 Nanoparticle Reactivity with TCE in Water: Conceptual Model and Mechanisms. *Environ. Sci. Technol.* **2009,** *43,* 1507–1514.

88. He, F.; Zhao, D. Preparation and Characterization of a New Class of Starch-Stabilized Bimetallic Nanoparticles for Degradation of Chlorinated Hydrocarbons in Water. *Environ. Sci. Technol.* **2005,** *39,* 3314–3320.

89. Shahwan, T.; Abu Sirriah, S.; Nairat, M.; Boyacı, E.; Eroglu, A. E.; Scott, T. B.; Hallam, K. R. Green synthesis of iron nanoparticles and their application as a Fenton-like catalyst for the degradation of aqueous cationic and anionic dyes. *Chem. Eng. J.* **2011,** *172 ,* 258– 266.

90. Njagi, E. C.; Huang, H.; Stafford, L.; Genuino, H.; Galindo, H. M.; Collins, J. B.; Hoag, G. E.; Suib, S. L. Biosynthesis of iron and silver nanoparticles at room temperature using aqueous Sorghum Bran extracts. *Langmuir* **2011,** *27 ,* 264–271.

91. Üzüm, C.; Shahwan, T.; Eroğlu, A. E.; Hallam, K. R.; Scott, T. B.; Lieberwirth, I. Synthesis and characterization of kaolinite-supported zero-valent iron nanoparticles and their application for the removal of aqueous Cu2+ and Co2+ ions. *Appl. Clay. Sci.* **2009,** *43 ,* 172–181.

92. Shahwan, T.; Üzüm, C.; Eroğlu, A. E.; Lieberwirth, I. Synthesis and characterization of bentonite/iron nanoparticles and their application as adsorbent of cobalt ions. *Appl. Clay Sci.* **2010,** *47 ,* 257–262.

93. Frost, R. L.; Xi, Y.; He, H. Synthesis, characterization of palygorskite supported zero-valent iron and its application for methylene blue adsorption. *J. Colloid Interface Sci.* **2010,** *341 ,* 153–161.

94. Karabelli, D.; Ünal, S.; Shahwan, T.; Eroglu, A. E. Preparation and characterization of alumina-supported iron nanoparticles and its application for the removal of aqueous Cu2+ ions. *Chem. Eng. J.* **2011,** *168 ,* 979–984.

95. Ponder, S. M.; Darab, J. G.; Bucher, J.; Caulder, D.; Craig, I.; Davis, L.; Edelstein, N.; Lukens, W.; Nitsche, H.; Rao, L.; Shuh, D. K.; Mallouk, T. E. Surface Chemistry and Electrochemistry of Supported Zerovalent Iron Nanoparticles in the Remediation of Aqueous Metal Contaminants. *Chem. Mater.* **2001,** *13,* 479-486.

96. Zhan, J.; Zheng, T.; Piringer, G.; Day, C.; McPherson, G.; Lu, Y.; Papadopoulos, K.; John, V. Transport Characteristics of Nanoscale Functional Zerovalent Iron/Silica Composites for in Situ Remediation of Trichloroethylene. *Environ. Sci. Technol.* **2008,** *42,* 8871–8876.

97. Shu, H. Y.; Chang, M. C.; Chen, C. C.; Chen, P. E. Using resin supported nano zero-valent iron particles for decoloration of Acid Blue 113 azo dye solution. *J. Hazard. Mater.* **2010,** *184 ,* 499–505.

98. Wang, W.; Zhou, M.; Mao, Q.; Yue, J.; Wang, X. Novel NaY zeolite-supported nanoscale zero-valent iron as an efficient heterogeneous Fenton catalyst. *Catal. Commun.* **2010,** *11 ,* 937–941.

99. Kim, S.; Kamala-Kannan, S.; Lee, K.; Park, Y.; Shea, P.; Lee, W.; Kim, H.; Oh, B. Removal of Pb(II) from aqueous solution by a zeolite–nanoscale zero-valent iron composite. *Chem. Eng. J.* **2013,** *217,* 54-60.

100. Xiao, S.; Shen, M.; Guo, R.; Huang, Q.; Wan, S.; Shi, X. Fabrication of multiwalled carbon nanotube-reinforced electrospun polymer nanofibers containing zero-valent iron nanoparticles for environmental applications. *J. Mater. Chem.* **2010,** *20,* 5700–5708.

101. Mackenzie, K.; Bleyl, S.; Georgi, A.; Kopinke, F. D. Carbo-Iron – An Fe/AC composite – As alternative to nano-iron for groundwater treatment. *Water Res.* **2012,** *46,* 3817-3826.

102. Zhang, H.; Jin, Z.; Han, L.; Qin, C. Synthesis of nanoscale zero-valent iron supported on exfoliated graphite for removal of nitrate. *Trans. Nonferrous Met. SOC. China* **2006,** *16,* s345-s349.

103. Horzum, N.; Demir, M. M.; Nairat, M.; Shahwan, T. Chitosan fiber-supported zero-valent iron nanoparticles as a novel sorbent for sequestration of inorganic arsenic. *RSC Adv.* **2013,** Published Online.

104. Zhan, J.; Sunkara, B.; Le, L.; John, V. T.; He, J.; McPherson, G. L.; Piringer, G.; Lu, Y. Multifunctional Colloidal Particles for in Situ Remediation of Chlorinated Hydrocarbons. *Environ. Sci. Technol.* **2009,** *43,* 8616–8621.

105. Cao, J.; Wei, L.; Huang, Q.; Wang, L.; Han, S. Reducing degradation of azo dye by zero-valent iron in aqueous solution. *Chemosphere* **1999,** *38,* 565-571.

106. Shu, H.; Chang, M.; Yu, H.; Chen, W. Reduction of an azo dye Acid Black 24 solution using synthesized nanoscale zerovalent iron particles. *J. Colloid Interface Sci.* **2007,** *314 ,* 89–97.

107. Shu, H.; Chang, M.; Chang, C. Integration of nanosized zero-valent iron particles addition with UV/H2O2 process for purification of azo dye Acid Black 24 solution. *J. Hazard. Mater.* **2009,** *167 ,* 1178–1184.

108. Lin, Y.; Weng, C.; Chen, F. Effective removal of AB24 dye by nano/micro-size zero-valent iron. *Sep. Purif. Technol.* **2008,** *64 ,* 26–30.

109. Satapanajaru, T.; Chompuchan, C.; Suntornchot, P.; Pengthamkeerati, P. Enhancing decolorization of Reactive Black 5 and Reactive Red 198 during nano zerovalent iron treatment. *Desalination* **2011,** *266 ,* 218–230.

110. Moon, B.; Park, Y.; Park, K. Fenton oxidation of Orange II by pre-reduction using nanoscale zero-valent iron. *Desalination* **2011,** *268 ,* 249–252.

111. Zhao, Z.; Liu, J.; Tai, C.; Zhuo, Q.; Hu, J.; Jiang, G. Rapid decolorization of water soluble azo-dyes by nanosized zero-valent iron immobilized on the exchange resin. *Sci. China Ser. B* **2008,** *51,* 186-192.

112. Xi, Y.; Megharaj, M.; Naidu, R. Dispersion of zerovalent iron nanoparticles onto bentonites and use of these catalysts for orange II decolourisation. *Appl. Clay Sci.* **2011,** *53 ,* 716–722.

113. Hoag, G. E.; Collins, J. B.; Holcomb, J. L.; Hoag, J. R.; Nadagouda, M. N.; Varma, R. S. Degradation of bromothymol blue by 'greener' nano-scale zero-valent iron synthesized using tea polyphenols. *J. Mater. Chem.* **2009,** *19,* 8671–8677.

114. Rakhshaee, R. Rule of Fe0 nano-particles and biopolymer structures in kinds of the connected pairs to remove Acid Yellow 17 from aqueous solution: Simultaneous removal of dye in two paths and by four mechanisms. *J. Hazard. Mater.* **2011,** *197 ,* 144– 152.

115. Zhang, J.; Liu, Q.; Ding, Y.; Bei, Y. 3-aminopropyltriethoxysilane functionalized nanoscale zero-valent iron for the removal of dyes from aqueous solution. *Pol. J. Chem. Technol.* **2011,** *13,* 35-39.

116. Trujillo-Reyes, J.; Sánchez-Mendieta, V.; Colín-Cruz, A.; Morales-Luckie, R. A. Removal of Indigo Blue in Aqueous Solution Using Fe/Cu

Nanoparticles and C/Fe–Cu Nanoalloy Composites. *Water Air Soil Pollut.* **2010,** *207,* 307–317.

117. Bokare, A. D.; Chikate, R. C.; Rode, C. V.; Paknikar, K. M. Iron-nickel bimetallic nanoparticles for reductive degradation of azo dye Orange G in aqueous solution. *Appl. Catal. B Eniron.* **2008,** *79 ,* 270–278.

118. Afkhami, A.; Moosavi, R. Adsorptive removal of Congo red, a carcinogenic textile dye, from aqueous solutions by maghemite nanoparticles. *J. Hazard. Mater.* **2010,** *174 ,* 398–403.

119. Feng, J.; Hu, X.; Yue, P. L. Degradation of Azo-dye Orange II by a Photoassisted Fenton Reaction Using a Novel Composite of Iron Oxide and Silicate Nanoparticles as a Catalyst. *Ind. Eng. Chem. Res.* **2003,** *42,* 2058-2066.

120. Mak, S. Y.; Chen, D. H. Fast adsorption of methylene blue on polyacrylic acid-bound iron oxide magnetic nanoparticles. *Dyes Pigm.* **2004,** *61 ,* 93–98.

121. Li, F.; Wu, X.; Ma, S.; Xu, Z.; Liu, W.; Liu, F. Adsorption and Desorption Mechanisms of Methylene Blue Removal with Iron-Oxide Coated Porous Ceramic Filter. *J. Water Res. Prot.* **2009,** *1,* 1-57.

122. Nasrazadani, S.; Namduri, H. Study of phasetransformation in ironoxides using Laser Induced Breakdown Spectroscopy. *Spectrochim. Acta B* **2006,** *61,* 565–571.

123. Lee, D. K.; Kang, Y. S. Preparation and characterization of magnetic nanoparticles by γ-irradiation. *Mater. Sci. Eng. C* **2004,** *24,* 107–111.

124. Liu, Y.; Majetich, S. A.; Tilton, R. D.; Sholl, D. S.; Lowry, G. V. TCE Dechlorination Rates, Pathways, and Efficiency of Nanoscale Iron Particles with Different Properties. *Environ. Sci. Technol.* **2005,** *39,* 1338-1345.

125. Aronniemi, M.; Sainio, J.; Lahtinen, J. XPS study on the correlation between chemical state and oxygen-sensing properties of an iron oxide thin film. *Appl. Surf. Sci.* **2007,** *253,* 9476–9482.

126. Lu, W.; Yang, D.; Sun, Y.; Guo, Y.; Xie, S.; Li, H. Preparation and structural characterization of nanostructured iron oxide thin films. *Appl. Surf. Sci.* **1999,** *147 ,* 39–43.

127. Abdel-Samad, H.; Watson, P. R. An XPS study of the adsorption of lead on goethite (a-FeOOH). *Appl. Surf. Sci.* **1998,** *136*.

128. Wannaparhun, S.; Seal, S.; Desai, V. Surface chemistry of Nextel-720, alumina and Nextel-720/alumina ceramic matrix composite (CMC) using XPS–A tool for nano-spectroscopy. *Appl. Surf. Sci.* **2002,** *185 ,* 183–196.

129. Allen, G. C.; Curtis, M. T.; Hooper, A. J.; Tucker, P. M. X-Ray photoelectron spectroscopy of iron–oxygen systems. *J. Chem. Soc. Dalton Trans.* **1974,** *14,* 1525-1530.

130. Tan, B. J.; Klabunde, K. J.; Sherwood, M. A. X-ray photoelectron spectroscopy studies of solvated metal atom dispersed catalysts. Monometallic iron and bimetallic iron-cobalt particles on alumina. *Chem. Mater.* **1990,** *2,* 186-191.

131. Tan, B. J.; Klabunde, K. J.; Sherwood, M. A. XPS studies of solvated metal atom dispersed (SMAD) catalysts. Evidence for layered cobalt-manganese particles on alumina and silica. *J. Am. Chem. Soc.* **1991,** *113,* 855–861.

132. Paparazzo, E. XPS analysis of oxides. *Surf. Interface Anal.* **1988,** *12 ,* 115–118.

133. Duman, A. *Zeolite Product Information Sheet;* Balikesir, Turkey. (Retrived March 24, 2010)

134. Barr, T. L. The nature of the relative bonding chemistry in zeolites: An XPS study. *Zeolites* **1990,** *10,* 760-765.

135. Ruiz-Serrano, D.; Flores-Acosta, M.; Conde-Barajas, E.; Ramírez-Rosales, D.; Yáñez-Limón, J.; Ramírez-Bon, R. Study by XPS of different conditioning processes to improve the cation exchange in clinoptilolite. *J. Mol. Struct.* **2010,** *980 ,* 149–155.